The role of kinesin-8 and PRC1 proteins in kinetochorepositioning in the metaphase plate

Jagrić, Mihaela

Doctoral thesis / Disertacija

2021

Degree Grantor / Ustanova koja je dodijelila akademski / stručni stupanj: **University of Zagreb, Faculty of Science / Sveučilište u Zagrebu, Prirodoslovno-matematički fakultet**

Permanent link / Trajna poveznica: https://urn.nsk.hr/urn:nbn:hr:217:286908

Rights / Prava: In copyright/Zaštićeno autorskim pravom.

Download date / Datum preuzimanja: **2024-04-25**

University of Zagreb

FACULTY OF SCIENCE
DEPARTMENT OF BIOLOGY

Mihaela Jagrić

THE ROLE OF KINESIN-8 AND PRC1 PROTEINS IN KINETOCHORE POSITIONING IN THE METAPHASE PLATE

DOCTORAL THESIS

Zagreb, 2020.

University of Zagreb

PRIRODOSLOVNO-MATEMATIČKI FAKULTET
BIOLOŠKI ODSJEK

Mihaela Jagrić

ULOGA PROTEINA KINEZINA-8 I PRC1 U SMJEŠTANJU KINETOHORA U METAFAZNOJ RAVNINI

DOKTORSKI RAD

Zagreb, 2020.

Supervisor biography

Professor Iva Tolić was born in Zagreb, Croatia. She graduated Molecular biology at Faculty of Science, University of Zagreb, Croatia in 1996. During her graduate studies, she worked as a Research assistant in the group of Prof. Nenad Trinajstić, Ruđer Bošković Institute. Her PhD work was done at Harvard School of Public Health, Boston, USA with Prof. Ning Wang. She obtained her academic degree of Doctor of biology at University of Zagreb in 2002. She worked as a postdoctoral fellow with Prof. Kirstine Berg-Sørensen at Niels Bohr Institute, Copenhagen, Denmark and later with Prof. Francesco Pavone, LENS - European Laboratory for Non-Linear Spectroscopy, Florence, Italy. From 2005 until 2014 she was a Leader of her Research Group at Max Planck Institute of Molecular Cell Biology and Genetics in Dresden, Germany. She works in the area of natural sciences, biology and physics with emphasis on mitosis, microtubules, motor proteins and mitotic spindle mechanics in general. Professor Iva Tolić has received many valuable and prestigious research grants, including two projects funded by European Research Council (ERC), ERC Consolidator (*A new class of microtubules in the spindle exerting forces on kinetochores*) and recently also ERC Synergy Grant (*Molecular origins of aneuploidies in healthy and diseased human tissues*) in collaboration with Geert Kops (Hubrecht institute-KNAW, Netherlands), Angelika Amon (MIT, USA) and Nenad Pavin (University of Zagreb, Croatia). She has published more than 80 papers in peer-reviewed journals including *Science*, *Cell*, and *Nature Cell Biology*, cited more than 5000 times, and served as reviewer for these and various other journals. She has been elected to EMBO membership and received numerous awards including the Ignaz Lieben Award of the Austrian Academy of Sciences, European Biophysical Societies Association (EBSA) Young Investigators' Medal and Prize, and Order of Danica Hrvatska for science. To this date she has mentored 10 PhD and 10 Master theses. As an invited speaker, she has participated in more than 100 conferences and seminars worldwide. She organized several scientific meetings including the *EMBO Conference on Meiosis* in Hvar and conference *Mitotic spindle: From living and synthetic systems to theory* in Split. Currently, professor Iva Tolić is a Senior Research Group Leader with tenure at Ruđer Bošković Institute in Zagreb.

Acknowledgements

Firstly, I would like to express my gratitude to my supervisor Iva Tolić for giving me an opportunity to work in her lab. Her enthusiasm, dedication and love for science were really inspiring these four years.

My immense gratitude goes to my parents Mijo and Terezija for all their love and support, for raisning me to be who I am and teaching me that it is far more important who you are than what you are… also to my sisters Adela, Martina and Gabriela for always being my best friends and loving me unconditionally. You are the best family I could ever wish for and I am so lucky to have you!

I thank to my friends for all the gatherings, birthday parties, movie nights, coversations, laughs and support over the years.

Special thanks go to my lab partners and friends, Patrik and Jelena from whom I learned so much…to Patrik, for all the coffees we drank, all conversations, for all the knowledge you shared with me. You are a true inspiration…to Jelena for always being calm and rational (especially when things did not go well) and for teaching me how to write my first for loop in MATLAB. Guys, you are the best!

I thank to "Rays of sunshine" of our office: Valentina, Isabella and Iva, for their positive energy, enthusiasm and all the conversations in our walks from work.

Big thanks go to all other former and present members of Tolić and Pavin group. My dear collegues and friends, you made these years to be one amazing and fun experience.

THE ROLE OF KINESIN-8 AND PRC1 PROTEINS IN KINETOCHORE POSITIONING IN THE METAPHASE PLATE

Mihaela Jagrić,

Ruđer Bošković Institute

In metaphase of mitosis, chromosomes align at the equatorial plane of the spindle, which is crucial for correct completion of later phases. Chromosome alignment is regulated by forces exerted by dynamics of kinetochore fibers (k-fibers) and polar ejection forces. This study explored a role of motor protein kinesin-8, which is known as one of main regulators of k-fiber dynamics, in chromosome alignment. Here, I showed that kinesin-8 regulates velocity and amplitude of kinetochore movements, while experiments of laser ablation of k-fibers after depletion of kinesin-8 indicate it has a role in limiting the growth of microtubules.

Furthermore, chromosome alignment could be influenced by bridging fibers, new class of microtubules in the spindle that connect sister k-fibers and balance the tension on sister kinetochores. This possibility is investigated by developing and applying optogenetic approach to manipulate localization of PRC1 protein, which specifically crosslinks microtubules within the bridging fibers. Acute removal of PRC1 led to partial disassembly of bridging fibers and elongation of their antiparallel overlaps, which was accompanied by misaligned and lagging chromosomes. Kif4A/kinesin-4 and Kif18A/kinesin-8 were also found within bridging fibers and largely lost upon PRC1 removal, suggesting that these proteins regulate the overlap length of bridging microtubules. Finally, a model is proposed where PRC1-mediated crosslinking of bridging microtubules and recruitment of kinesins to the bridging fiber promote chromosome alignment by overlap length-dependent forces transmitted to the associated k-fibers.

ULOGA PROTEINA KINEZINA-8 I PRC1 U SMJEŠTANJU KINETOHORA U METAFAZNOJ RAVNINI

Mihaela Jagrić,

Ruđer Bošković Institute

U metafazi mitoze kromosomi se poravnavaju u ekvatorijalnoj ravnini diobenog vretena što je od ključne važnosti za pravilan završetak kasnijih faza. Poravnavanje kromosoma regulirano je silama dinamike kinetohornih vlakana (k-vlakana) te silama odbijanja na polovima. U ovome radu istražena je uloga kinezina-8 u poravnavanju kromosoma, koji je jedan od glavnih regulatora dinamike k-vlakana. Pokazala sam kako kinezin-8 regulira brzinu i amplitudu kretanja kinetohora, dok eksperimenti laserskog rezanja k-vlakana nakon deplecije kinezina-8 upućuju na njegovu ulogu u ograničavanju rasta mikrotubula.

Nadalje, ulogu u poravnavanju kromosoma mogla bi imati premošćujuća vlakna, nova klasa mikrotubula u vretenu koja povezuje sestrinska k-vlakna i balansira silu tenzije na sestrinskim kinetohorama. Ova mogućnost istražena je razvitkom i primjenom optogenetičkog pristupa za manipulaciju lokalizacije proteina PRC1 koji specifično povezuje mikrotubule u premošćujućim vlaknima. Akutno uklanjanje proteina PRC1 dovelo je do djelomičnog raspada premošćujućih vlakana i produljenja njihovih antiparalelnih preklopa, uz pojavu neporavnatih i zaostajućih kromosoma. Kif4A/kinezin-4 i Kif18A/kinezin-8 uočeni su u premošćujućim vlaknima, no većinom izgubljeni nakon uklanjanja PRC1, što upućuje na to da ovi proteini reguliraju duljine preklopa premošćujućih mikrotubula. Zaključno, predložen je model prema kojemu PRC1 povezujući mikrotubule u premošćujućim vlaknima i regrutiranjem kinezina u premošćujuća vlakna pospješuje poravnanje kromosoma silama ovisnim o duljini preklopa koje se posredno prenose na k-vlakna.

Table of Contents

1. INTRODUCTION

The cell cycle of eukaryotic cells consists of interphase (I) and mitotic (M) phase. Key events in the cell cycle occur during S phase of interphase, (for synthesis) when duplication of DNA occurs, and in M phase, when duplicated genetic material is equally distributed between daughter cells. In majority of cells, there are also two G phases (for gap) when protein synthesis and cell growth occurs, thus preparing cells for later phases. Mitosis starts with prophase marked by chromosome condensation and separation of centrosomes. At the end of prophase nuclear envelope disassembles marking the beginning of prometaphase when chromosomes are being incorporated in the spindle by attaching to microtubules and begin their movement towards equatorial plate in the process termed congression. In metaphase chromosomes are aligned at the spindle centre and exhibit phenomenon of oscillatory movements towards and away from the spindle equator. If all the chromosomes are properly attached to the spindle microtubules, cell progresses to anaphase marked by separation of sister chromatids and their synchronous movement towards poles. During telophase, nuclear envelope reassembles and chromosomes decondense. Finally, M phase ends with cytokinesis when cytoplasm divides in two (Alberts et al., 2017).

The central structure required for mitosis to occur is the mitotic spindle built from microtubules and numerous microtubule associated proteins (MAPs) (Pavin and Tolic, 2016; Prosser and Pelletier, 2017). Microtubules are hollow cylinders built from 13 protofilaments that assemble by head-to-tail stacking of αβ-tubulin heterodimers. Important features of microtubules are their structural polarity, with α-tubulin being exposed on the minus (-) end, and β-tubulin on the plus (+) end, and dynamic instability, or the ability of microtubules to stochastically switch between the states of growth and shrinkage (Alberts et al., 2017). Within the spindle, microtubules persist as individual ones or, more often, are organized into bundles. Based on the orientation of microtubules from which they are built, bundles can be comprised from parallel or antiparallel microtubules. The most stable population of spindle microtubules are kinetochore fibers (k-fibers) that attach with their plus ends to kinetochores, protein complexes on chromosomes (Brinkley and Cartwright, 1975; Musacchio and Desai, 2017). Non-kinetochore microtubules are all those that do not end at kinetochores. These include astral microtubules that extend towards the cell cortex, those that extend toward spindle equator, but have free ends, often called polar, and interpolar or overlap microtubules that form antiparallel overlaps in the central part of the spindle (Tolic, 2018).

The ultimate goal of mitosis is to equally and faithfully divide the genetic material in anaphase so that each daughter cell receives identical number of chromosomes. This is ensured in the preceding phases of mitosis by establishment of proper kinetochore-microtubule attachments, which are being rigorously monitored by the spindle assembly checkpoint (Musacchio and Salmon, 2007), and the alignment of chromosomes at the position equidistant from both spindle poles. These mechanisms are thought to be a prerequisite for synchronous movement of chromosomes in anaphase, and therefore chromosome inheritance fidelity (Cimini, 2008; Maiato et al., 2017; Walczak et al., 2010). Recently, chromosome alignment itself, apart from kinetochore-microtubule attachments, was shown to promote growth and survival in mice by ensuring proper incorporation and organisation of chromosomes into a single nucleus at mitotic exit, and continued cell proliferation (Fonseca et al., 2019). Therefore, it is important to explore and understand the precise mechanisms involved in congression and maintenance of chromosome alignment at the spindle equator, as this is an important feature required for punctuality of genetic material distribution between daughter cells.

The maintenance of chromosome alignment at the spindle equator is generally thought to rely on two main mechanisms: those based on length-dependent pulling and polar ejection forces (PEFs) (**Fig. 1**). Length-dependent pulling forces exerted by plus-ends of k-fibers are thought to be regulated by kinesin-8 motor proteins, which were shown to regulate k-fiber dynamics in a length-dependent manner in yeast (Tischer et al., 2009; Varga et al., 2006; Varga et al., 2009), and are needed for proper kinetochore alignment in various organisms from yeast to humans (Garcia et al., 2002; Stumpff et al., 2008; Wargacki et al., 2010). In addition to the forces produced by k-fibers, PEFs are proposed to push chromosome arms away from the pole, thus preventing chromosomes to move in the vicinity of the poles, far from the equator. These forces are mediated by action of arm-bound chromokinesins that walk towards the plus end of microtubules (**Fig. 1**) (Bajer et al., 1982; Brouhard and Hunt, 2005).

Although kinesin-8 was proposed to regulate k-fiber dynamics and promote pulling of kinetochores in a length-dependent manner in yeast (Mary et al., 2015; Tischer et al., 2009; Varga et al., 2006), the mode of action of human Kif18A/kinesin-8 is still unknown. Also, as k-fibers were shown not to be isolated from other populations of microtubules in the spindle, but interact with them (McDonald et al., 1992; O'Toole et al., 2020), the forces acting on kinetochores not necessarily come only from the plus-ends of k-fibers, regulated mainly by kinesin-8, but also from these microtubules that can exert forces on k-fibers and in this way

on kinetochores also. In particular, sister k-fibers were shown to be tightly linked by the bridging fiber, a bundle of antiparallel microtubules that balances the tension on sister kinetochores, whose microtubules are crosslinked by non-motor protein PRC1 (Kajtez et al., 2016; Milas and Tolić, 2016; Polak et al., 2017; Tolic, 2018; Vukusic et al., 2017). Therefore, bridging fibers may also have a role in maintenance of chromosome alignment at the equator, but this concept is still unknown and unexplored (**Fig. 1**).
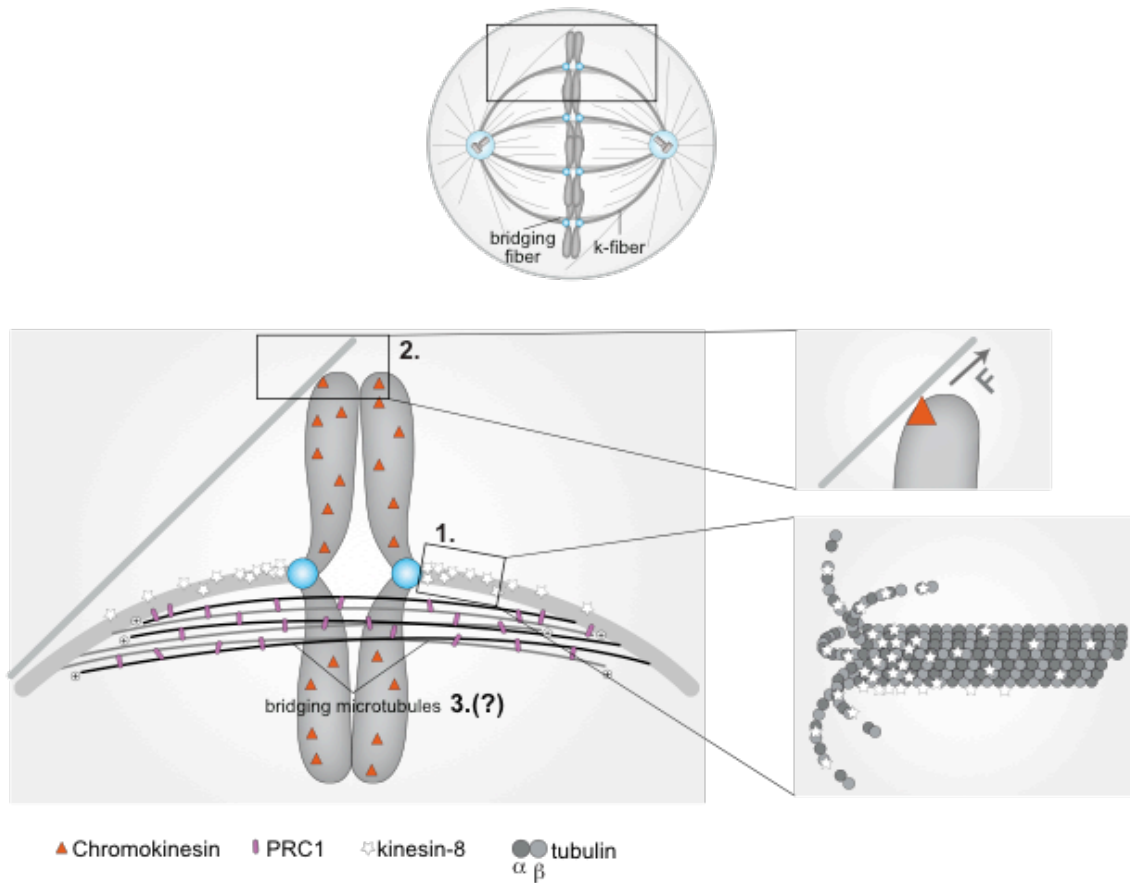
Figure 1. Mechanisms involved in chromosome alignment. Chromosome alignment is usually thought to be regulated by two main mechanisms. Length-dependent regulation of k-fiber dynamics, exerted by kinesin-8 motors (1) and PEFs mediated by chromokinesins (2). In addition, recently discovered bridging fibers, that interact with k-fibers could also have a role in this process (3), but this is still unexplored.

To explore some of these unanswered questions, the motivation of this research was to examine roles of Kif18A as major player in chromosome alignment in further detail, more precisely, how it contributes to force generation at kinetochores. Also, the goal was to test completely new premise about possible involvement of bridging fibers in chromosome

alignment and if such role is confirmed, explore underlying mechanisms involved in this process.

To explore the mechanisms of how Kif18A regulates dynamics of k-fibers, live-cell imaging of human retinal pigment epithelial (RPE-1) cells with labelled kinetochores and poles will be used. Influence of Kif18A on kinetochore movements in this cell line will be explored by varying its levels using siRNA or excessive expression of untagged kinesin-8 from plasmid. Kinetochore movements will be tracked and various parameters quantified (e.g. kinetochore distances from the metaphase plate, velocity of kinetochore movements and switch rates) and compared between control and cells with changed amounts of Kif18A in this cell line, but also with results of similar experiments in other cell line (Mayr et al., 2007; Stumpff et al., 2008). The role of Kif18A in force generation at kinetochores will be explored by laser ablation of outer kinetochore fibers, that will be performed similarly as in our previous work (Buda et al., 2017; Kajtez et al., 2016; Vukusic et al., 2017). Performing these experiments in control cells will show whether pulling or pushing forces on kinetochores are responsible for their movements, while laser ablations in regimes of different amount of kinesin-8 will give an insight in how Kif18A contributes to and affects these forces.

The role of bridging fibers in kinetochore alignment will be explored by development of an optogenetic approach based on the improved Light Inducible Dimer System (iLID) (Guntas et al., 2015) for acute and reversible removal of PRC1 from the spindle to the cell membrane in metaphase, which will be achieved by exposing cells to the blue light. This approach has many advantages over conventionally used siRNA, since it enables manipulation of proteins on a short time-scale, in real-time and precise phase of mitosis, while also being easily applicable and reversible. In these optogenetic experiments, endogenous PRC1 will be depleted by siRNA and siRNA-resistant optogenetic constructs will be added by transfecting the cells with plasimds coding for opto-PRC1 and light-responsive component iLID. Upon PRC1 removal, various parameters regarding kinetochore alignment and spindle mechanics will be monitored and measured.

The main conceptual advance of this work is the finding of novel mechanisms that contribute to chromosome alignment and were not included in the existent models, where the forces required for kinetochore alignment are not exerted exclusively at k-fiber plus tips as a consequance of their dynamics, but also indirectly through their interaction with bridging fibers.

2. OVERVIEW OF RESEARCH

2.1 A brief history of cell theory

Cells are basic structural, functional and biological units of all known organisms. All cells share some fundamental properties that remained conserved throughout evolution: they posses DNA as a genetic material, are surrounded by plasma membranes which separate them from, but also ensure communication with the surrounding environment, and use similar metabolic mechanisms for energy production.

The term "cell" was firstly coined by English natural philosopher, physicist and scientist Robert Hooke in 1665 after his observations of the structure of cork which reminded him of *cella*, a small room inhabited by monks. First live cells, including members of protozoa and bacteria, were observed and described somewhat later by Antonie van Leeuwenhoek (**Fig. 2**).
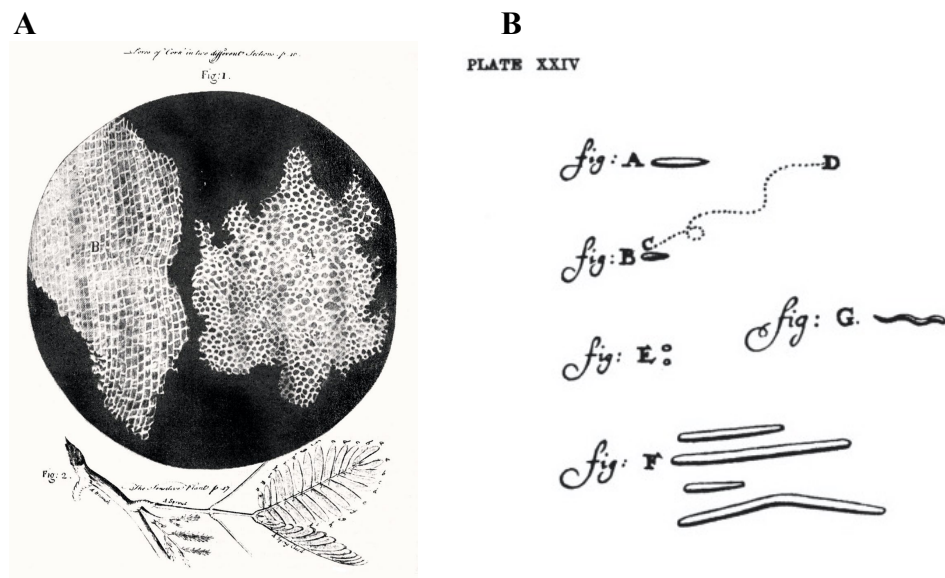
Figure 2. First evidence of cellular organization of life. **A.** Drawings of Hooke's observations of cork, which inspired the origin of the term "cell". **B.** Drawings of mouth bacteria by Leeuwenhoek, first live organisms observed under the microscope (Lane, 2015).

The contemporary definition of cells as basic building blocks of life was introduced in the 19th century by Matthias Schleiden and Theodor Schwann. They formulated a "cell theory" based on the assumption that all living forms are built from cells and in this way laid the foundations of modern biology (Mazzarello, 1999).

2.2 Overview of the cell cycle

Perhaps the most fundamental property of cells, either in a form of unicellular organism or as a constituent of a complex multicellular system, is their ability to self-reproduce and pass their genetic material on the next generation of cells. This process of cell division occurs through orderly sequence of events called the cell cycle, essential mechanism by which all living things reproduce. Although some details of the cell cycle can differ between certain organisms, the basic function remains universal: to duplicate DNA and then equally distribute the copies into two newly formed daughter cells.

The cell cycle of a typical eucaryotic cell is represented by a human cell in culture which divides approximately every 24 h and consists of two major basic parts: M-phase (M for *mitosis*) and interphase. The M-phase is the most dramatic stage of the cell cycle, which includes two major processes: nuclear division or *mitosis,* during which duplicated chromosomes segregate and distribute into two daughter nuclei, and cell division or *cytokinesis.* Interphase is the period between two cell divisions and consists of G_1 (G for *gap*), S and G_2 phases. DNA replication takes place in S phase (S for *synthesis*). The interval between M-phase and S phase is the first gap or G_1 phase, while G_2 represents time between S and M-phase (**Fig. 3**). Gap phases serve as a preparation period when cells grow and synthesize proteins required for DNA replication and mitosis, but also during which cells monitor their environment to ensure that conditions are appropriate and preparations complete for proceeding in ongoing phases. The G_1 phase is especially important in this sense. Its duration greatly depends on external conditions and extracellular signals from other cells. If the conditions are unfavorable, cells can delay their progress through G_1 and even enter the resting state, so-called G_0 (G zero) phase in which they can stay for longer periods before continuing with the cell cycle. On the other hand, if the conditions are favorable and all required signals are present, cells in early G_1 or G_0 progress through the commitment point called *restriction point* (or START in yeast) after which they are committed to progress to S phase. For a typical proliferating human cell with 24 h cycle, the G1 phase lasts up to 11 h, S phase about 8 h, G2 4 h and M-phase for about 1 h. In contrast, some cells of adult animals do not divide (nerve cells) or rest in G_0 state and divide only occasionally, in case of injury or cell death when cells need to be replaced (e.g. fibroblasts and liver cells) (Alberts et al., 2017; Cooper, 2019).
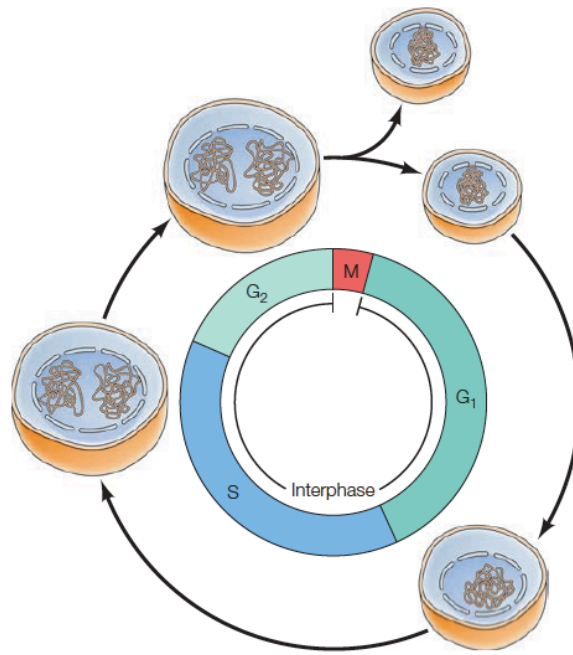
Figure 3. Phases of the cell cycle. The cell cycle of most eukaryotic cells consists of four distinct phases: M, G_1, S and G_2. M-phase includes segregation of duplicated DNA (mitosis) and division of entire cell (cytokinesis). DNA replication occurs in the S-phase. Gap phases (G_1 and G_2) are phases of cell growth and preparation for ongoing phases (Cooper, 2019).

2.2.1 Cell cycle regulation

Cell cycle is controlled by surveillance mechanisms that verify the order, integrity and accuracy of major events of the cell cycle. These control mechanisms called *checkpoints* prevent entry to the next phase of the cell cycle until the events of the previous one are not successfully completed (**Fig. 4**). The first checkpoint is the abovementioned restriction point (or START) in late G_1, which monitors cell's external environment as well as DNA integrity, and after which cell is committed to cell cycle-entry and DNA replication. The second checkpoint at the G_2/M transition prevents entry into mitosis if DNA is not completely replicated or contains unrepaired damage. The final checkpoint is at metaphase-to-anaphase transition, also called the spindle assembly checkpoint (or SAC), which ensures that chromosomes are accurately distributed to the daughter cells by preventing sister chromatide separation unless all chromosomes are properly attached to the mitotic spindle and aligned at the spindle equator (Alberts et al., 2017).
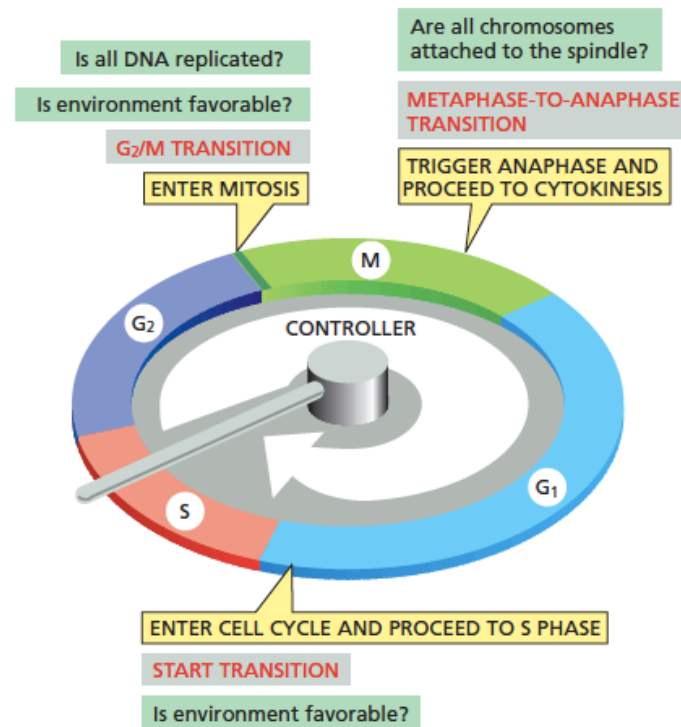
Figure 4. Control of the cell cycle by checkpoints. The cell cycle control system initiates DNA replication, mitosis and cytokinesis, major events of the cell cycle. The controller, represented as a central arm, triggers the events of the cell cycle when it reaches specific transition points (indicated in the yellow boxes). Cell's environment (in the terms of presence of growth factors and nutrients) and feedback about the completion of previous cell-cycle event can lead to arrest of the cell cycle by the controller at these transition points (Alberts et al., 2017).

The cell-cycle control system relies on the activity of members of a family of protein kinases called cyclin-dependent kinases (Cdks) that target intracellular proteins involved in initiation or regulation of major events of the cell cycle. As their activity cyclically changes during the cell cycle, so does the phosphorylation and activity of their target proteins. The cyclical changes in Cdk activity are regulated by proteins called cyclins, which undergo round of synthesis and degradation during each cell cycle, resulting in cyclic assembly and activation of cyclin-Cdk complexes in specific phases of the cell cycle. There are four classes of cyclins, each activating Cdks in the specific stage of the cell cycle: G_1/S-cyclins activate Cdks in the late G_1 thus enabling progression through restriction point and entering to S phase; S-cyclins that initiate chromosome duplication, and M-cyclins that enable entry into mitosis. Cyclins operate not only as simple activators of Cdk activity, but also function as guides that navigate Cdks to their specific target proteins. While the progression through restriction point and

G$_2$/M transition is regulated by activation of cyclin-Cdk complexes and consequential phosphorylation of their target proteins, the metaphase-to-anaphase transition is triggered not by protein activation, but degradation. The major regulator at this transition point is anaphase-promoting complex or cyclosome (APC/C) which belongs to the familiy of ubiquitin ligases. This APC/C is responsible for ubiquitination and destruction of securin, protein that acts as a protector of linkages that hold sister chromatides together, which subsequently activates protease that separates chromatides and allows start of anaphase.

2.3 Mitosis – an overview

Mitosis is the most dramatic process of the cell cycle which fascinates scientist ever since Walther Flemming in 1880s observed and described the events of mitosis in newt cells as we know them today (see Paweletz (2001)). Some details of mitosis differ between various organisms, but basic processes that ensure correct segregation of genetic material between daughter cells remained conserved in all eucaryotes. These fundamental events include chromosome condensation, assembly of the mitotic spindle, and incorporation of chromosomes in the spindle. Afterwards, sister chromatids separate and move to the opposite sides of the spindle followed by formation of daughter nuclei. Mitosis is a highly complex process commony divided into five sequential stages characterized by a specific behavior and spatial organisation of chromosomes: prophase, prometaphase, metaphase, anaphase and telophase (**Fig. 5**) (Alberts et al., 2017).
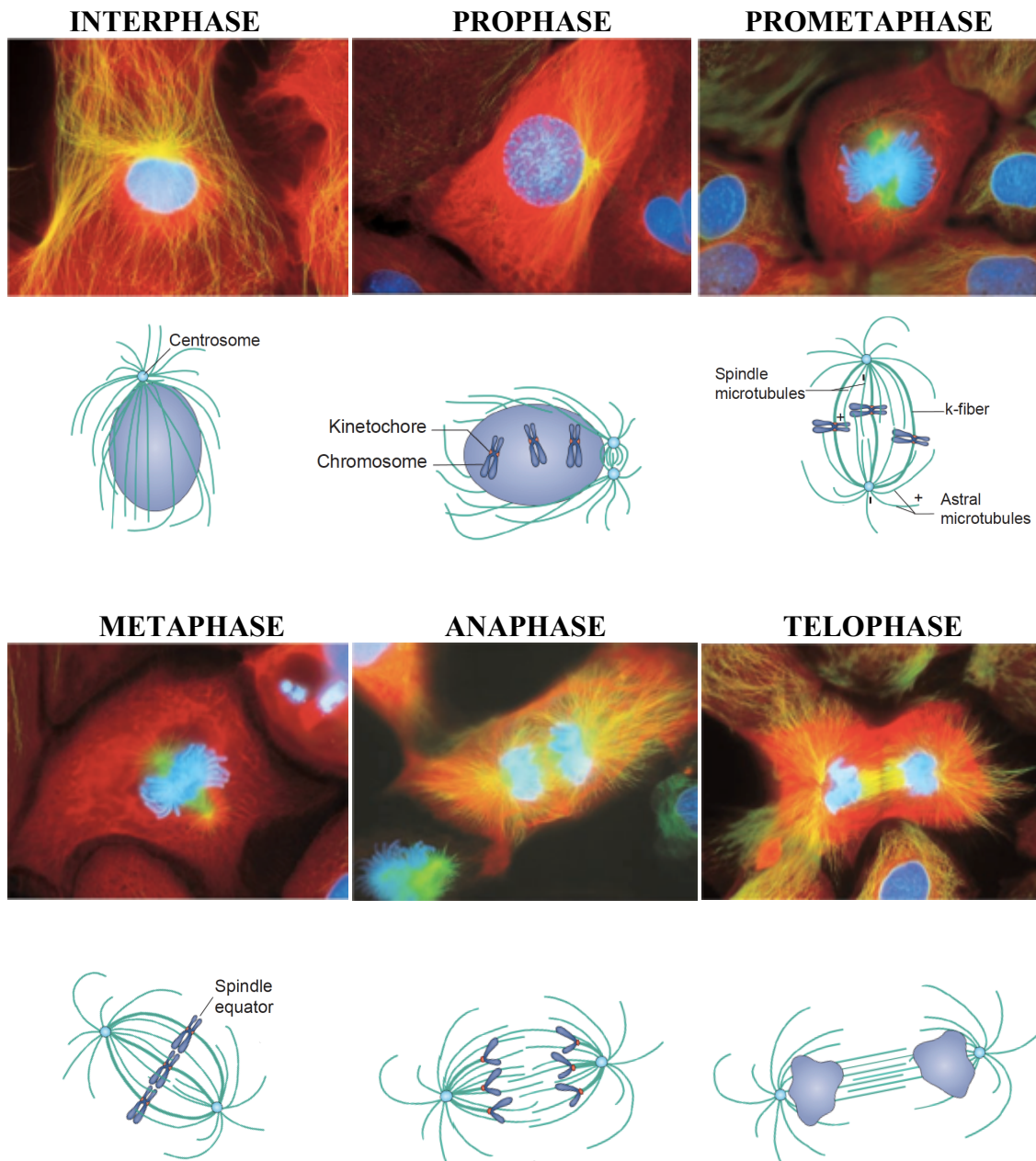
Figure 5. Phases of mitosis in mammalian cells. Conventionally, mitosis is subdivided into several consecutive phases defined based on the behaviour of chromosomes. In prophase chromosomes condense and centrosomes separate while nucleating microtubules that start formation of the mitotic spindle. Prometaphase begins with the nuclear envelope breakdown (NEBD) that allows capture of chromosomes and their movement toward equator (congression). In metaphase bi-oriented chromosomes are aligned in the centre of the spindle and exhibit poleward and away from the pole movements around spindle equator. Chromosomes separate and move toward poles in anaphase. During telophase, nuclear envelope reassembles and chromosomes decondense. Upper rows: fluorescence images of newt lung cells from (Cooper, 2019), where DNA is shown in blue, tubulin in

green and keratin in red. Bottom rows: corresponding drawings adapted and modified from (Walczak et al., 2010).

2.3.1 Prophase

During prophase previously duplicated chromosomes become highly condensed (nearly 1000-fold), now consisting of two sister chromatids bound together at the centromere by a protein complex cohesin. Furthermore, cell goes through extensive reorganisation of interphase microtubule network in order to form bipolar mitotic spindle. Centrosomes, duplicated in S phase, undergo processes of maturation and separation (**Fig. 6**) (Meraldi and Nigg, 2002). Centrosomes are organelles built from two perpendiculary oriented, barrel-shaped centrioles surrounded by a proteinaceous matrix called centrosomal material or pericentriolar material (PCM). In animal cells they act as a microtubule-organising centers (MTOCs) responsible for nucleation and organisation of microtubules. Maturation of centrosomes occurs through polo-like kinase 1 (Plk1) and Aurora A kinase mediated phosphorylation of pericentriolar material which triggers recruitment of additional PCM components, including γ-tubulin ring complexes (γ-TuRCs), key components required for microtubule nucleation, resulting in the increased nucleation and dynamics of microtubules compared to interphase (Hannak et al., 2001; Kuriyama and Borisy, 1981; Lee and Rhee, 2011; Saxton et al., 1984). Centrosome separation is a motor-driven process, mainly residing on the ability of Eg5/kinesin-5 motor protein to slide apart antiparallel microtubules, as its inactivation by small molecule inhibitor monastrol prevents centrosome separation and results in the formation of monoastral spindles (Kapoor et al., 2000; Tanenbaum and Medema, 2010).

Taken together, in prophase chromosomes consist of two sister chromatides, ready to be attached to microtubules of the spindle, while outside of the nucleus centrosomes begin to separate and extensively nucleate radial network of microtubules, thus starting the assembly of the mitotic spindle.
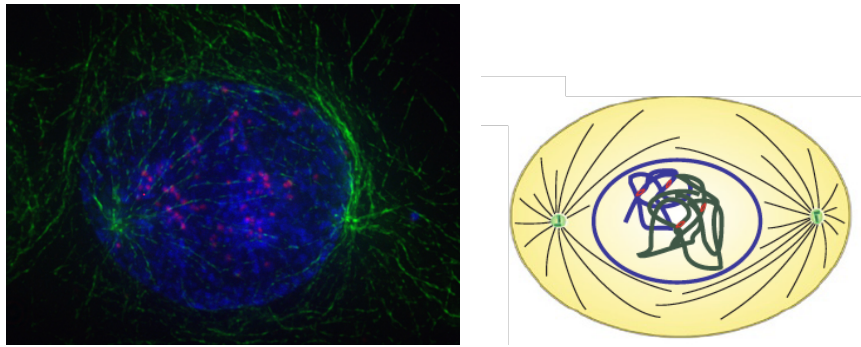
Figure 6. Prophase stage of mitosis. Human cell (left) immunostained for tubulin (green), kinetochores (red) and stained DNA (blue). Image downloaded from [commons.wikimedia.org]. Shematic illustration of prophase (right) from Silkworth and Cimini (2012).

2.3.2 Prometaphase

Prometaphase starts abruptly with disassembly of nuclear membrane or nuclear envelope breakdown (NEBD), making chromosomes accessible to the forming spindle (**Fig. 7**). The main events of prometaphase are incorporation of the chromosomes in the spindle by establishing correct amphitelic or 'bi-oriented' attachments, meaning that each chromosome is attached to the microtubules emanating from both poles, and their movement towards the spindle equator, a process known as congression (Walczak et al., 2010). The key attachment site of chromosomes to the microtubules of the spindle is at the kinetochores, macromolecular complexes assembled at the centromere of the chromosome (Cheeseman and Desai, 2008; Musacchio and Desai, 2017; Rieder and Salmon, 1998).
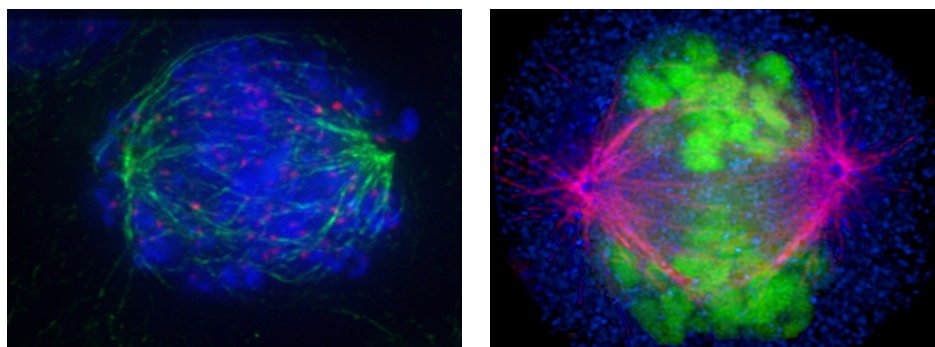
Figure 7. Prometaphase stage of mitosis. Early prometaphase in HeLa cell with tubulin shown in green, kinetochores in red and DNA in blue (left). Image downloaded from [commons.wikimedia.org]. Late prometaphase in HeLa cell with tubulin shown in magenta and DNA in green (right). Image downloaded from [wellcomecollection.org].

An intriguing question is how these initial kinetochore-microtubule attachments are established given the fact that human cells have 46 chromosomes randomly positioned throughout the cell at the moment of NEBD. According to 'search and capture' model the dynamically unstable microtubules nucleated from centrosomes probe the cellular space as they grow and shrink, changing their trajectory in each growth cycle thus 'searching' for kinetochores (**Fig. 8 A**) (Kirschner and Mitchison, 1986). Accordingly, angular motion of microtubules or pivoting was observed in yeast cells where it contributes to more efficient capture of kinetochores, but also formation of interpolar microtubules (Kalinina et al., 2013; Winters et al., 2019). Kinetochore capture ultimately leads to stabilisation of microtubules and incorporation of chromosome in the spindle (Mitchison and Kirschner, 1985; Nicklas and Kubai, 1985). However, mathematical modelling, based on the assumption that 'search and capture' process is completely unbiased and stochastic, revealed it would take considerably more for spindle to assemble and capture the chromosomes in comparison with 10-15 minutes observed in live cells. This time difference indicates the existence of additional mechanisms facilitating this process (Wollman et al., 2005). These include chromosome- and microtubule-mediated nucleation of microtubules, reviewed in Prosser and Pelletier (2017) (**Fig. 8 B**). The first one resides on the existence of RanGTP gradient in the vicinity of chromosomes, which facilitates phosphorylation of γ-TuRC adaptor protein NEDD1 by Aurora A kinase thus promoting microtubule nucleation in the vicinity of chromosomes that are subsequently incorporated into the rest of the spindle (Gruss and Vernos, 2004; Kalab et al., 2006; Khodjakov et al., 2003; Maiato et al., 2004a). The microtubule-mediated nucleation is achieved through augmin complex mediated recruitment of γ-TuRC on the walls of pre-existing microtubules (Goshima et al., 2008). Both these pathways enable the formation of the spindle even in the absence of centrosomes (Khodjakov et al., 2000) (**Fig. 8 B**). The formation of the robust spindle in systems with centrosomes is probably a combination of centrosomal and chromatin- and microtubule-mediated pathways of microtubule nucleation (Prosser and Pelletier, 2017) (**Fig. 8 C**).
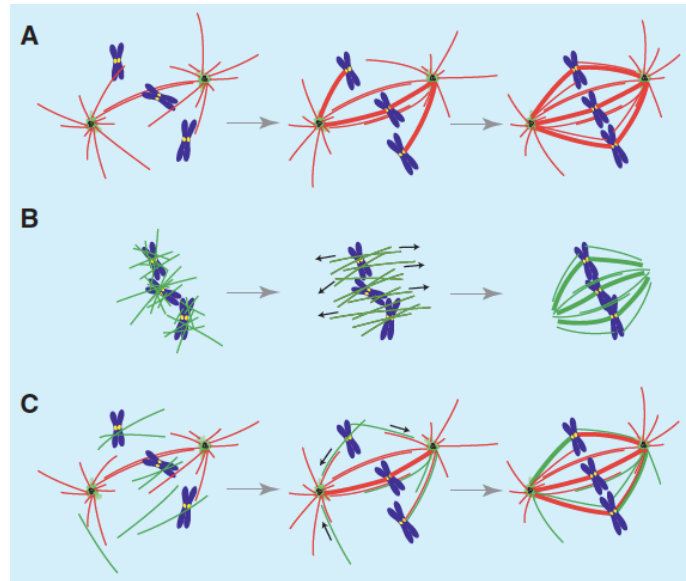
Figure 8. Models of spindle assembly. A. In the 'search and capture' model, microtubules grow from centrosomes in random directions until they encounter kinetochore and become stabilized. **B.** Self-organisation model in acentrosomal spindles, where microtubules are nucleated on kinetochores and along existing microtubules and organized into bipolar spindle. These mechanisms also exist in cells with centrosomes. **C.** Combined model of spindle assembly, where formation of the spindle is a result of both centrosomal and alternative pathways of micorotubule nucleation. Microtubules nucleated at centrosomes are indicated in red, those that are not are in green. Image from Gadde and Heald (2004).

The other important process of prometaphase is chromosome congression, prerequisite for proper chromosome segregation. It is known today that not all chromosomes use the same mechanisms for approaching the spindle equator (Walczak et al., 2010). Some chromosomes that had favourable position between the poles will achieve amphitelic, bi-oriented end-on attachments before congressing to equator (Barisic et al., 2014; Magidson et al., 2011). However, congression can occur even before amphitelic attachments are established by gliding of laterally attached kinetochores along pre-existing microtubules governed by motor proteins. This is mostly the case for chromosomes that are located near the poles or outside the spindle. This population firstly attaches to one pole, which is called monotelic attachment or monoorientation and moves polewards by dynein motor protein activity while subsequent movement towards equator is driven by CENP-E/kinesin-7 motor activity (Barisic et al., 2014; Kapoor et al., 2006). Mechanisms and proteins involved in the congression process are extensively reviewed in Auckland and McAinsh (2015) and Maiato et al. (2017).

2.3.3 Metaphase

In metaphase chromosomes established amphitelic bi-oriented attachments to microtubules and are aligned at the spindle equator (Walczak et al., 2010) (**Fig. 9**). During prometaphase, when initial kinetochore-microtubule attachments occur, it is common for incorrect configurations to arise. These include monotelic attachments (that are frequent in prometaphase as can be seen in the previous paragraph), when only one kinetochore is attached to one spindle pole; syntelic attachments, when both kinetochores are connected to the same pole; and merotelic when one kinetohore is attached to microtubules from both poles (Gregan et al., 2011). It is important in metaphase, prior to segregation, to detect and resolve incorrect attachments and establish correct ones, in order to prevent chromosome mis-segregation and aneuploidy. Luckily, cells possess surveillance safety mechanism called spindle assembly checkpoint (SAC), one of abovementioned checkpoints in the cell cycle that will halt metaphase-to-anaphase transition until all chromosomes are properly attached to microtubules. The molecular mechanism of SAC is based on the formation of mitotic checkpoint complex (MCC) as a response on the presence of unattached kinetochores, consisting of checkpoint proteins MAD2, BUBR1/Mad3 and BUB3, as well as CDC20 which is now unable to activate the ubiquitin ligase anaphase promoting complex/cyclosome (APC/C) (Sudakin et al., 2001). In addition to attachment, the proper level of inter-kinetochore tension is also an important signal that is monitored by SAC (Musacchio and Salmon, 2007). Corrections of improper attachments require MCAK/kinesin-13 whose localisation at centromeres and depolymerisation activity are regulated by Aurora B kinase (Andrews et al., 2004; Lan et al., 2004). Recent intriguing findings suggest MCAK's ability to discriminate between correct and incorrect attachments depends also on tubulin post-translational modifications or 'the tubulin code' (Ferreira et al., 2020; Janke and Magiera, 2020).
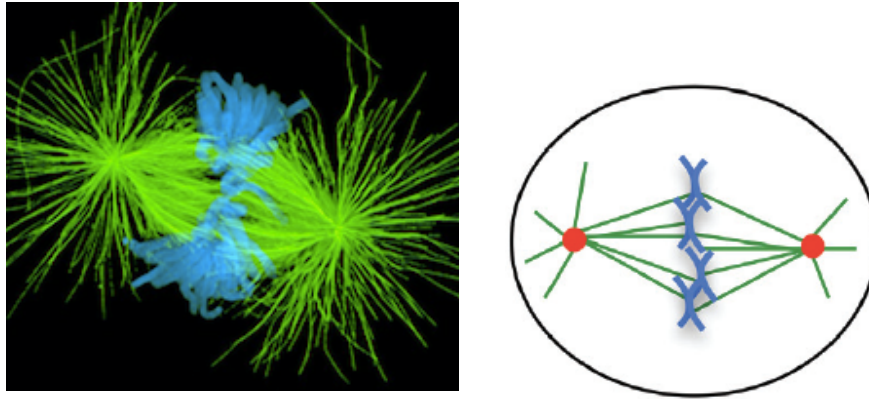
Figure 9. Metaphase of mitosis. Metaphase spindle in a newt lung cell with tubulin shown in green and DNA in blue (left). Image from O'Connell and Khodjakov (2007). Schematic illustration of a metaphase spindle (right) from Goodson and Jonasson (2018).

A characteristic feature of metaphase is chromosome directional instability, 'dance of chromosomes' or oscillations visible as chromosome movements towards and away from the spindle equator, believed to serve as an additional probing mechanism for accuracy of kinetochore-microtubule attachments (Walczak et al., 2010). Similar movements are observed in various organisms, from amphibians to yeast and mammals (Nabeshima et al., 1998; Skibbens et al., 1993; Wise et al., 1991). Chromosomes start oscillating already in prometaphase after establishment of bi-orientation with movements of both aligned and unaligned chromosomes being similar to metaphase oscillations, with exception that those unaligned are more biased in direction toward equator between reversals of movement (Rieder and Salmon, 1994; Skibbens et al., 1993). The main mechanisms and proteins involved in chromosome alignment and control of chromosome directional instability are reviewed and discussed in more detail later in this introductory part.

2.3.4 Anaphase

Mitosis culminates with anaphase, when the duplicated genetic material is equally divided between daughter cells. Anaphase begins when all chromosomes are bi-oriented with sister kinetochores attached to microtubules emanating from opposite spindle poles and SAC being satisfied (Joglekar, 2016). Chromosome segregation involves two characteristic types of movements: anaphase A, synchronous poleward movement of disjoined sister chromatids and anaphase B, elongation of the entire spindle, where the relative contribution of each phase to

chromosome segregation and their timing vary among different organisms (**Fig. 10**) (Roostalu et al., 2010). In human cells both mechanisms occur almost simultaneously and equally contribute to chromosome segregation (Vukusic et al., 2017). Anaphase A occurs through motor-independent shortening or depolymerisation of k-fibers, preferentially on their plus ends (pointing toward kinetochores), where it seems like kinetochores are 'chewing' on the k-fibers to approach the poles, reminiscent of a popular game Pac-Man (Cassimeris et al., 1987; Maiato and Lince-Faria, 2010). During this process kinetochores have to be able to track the ends of depolymerizing microtubules, this way coupling the movements of chromosomes to microtubule shortening. Although the shortening on the minus end (at the pole) also happens, its contribution to anaphase A movements is only minor in human cells (Vukusic et al., 2017; Vukusic et al., 2019b). Anaphase B is a mechanistically distinct process, where separation of spindle poles is driven by the pushing forces deriving from sliding of antiparallel interpolar microtubules governed by plus-end directed motor proteins (Vukusic et al., 2017; Vukusic et al., 2019a; Yu et al., 2019). In some other systems, for example in long-nosed potoroo epithelial kidney cells (PtK$_2$) and nematode *Caenorhabditis elegans,* these interpolar microtubules in the spindle midzone act more as a brake thus acting to resist spindle elongation, while predominant mechanism comes from the external cortical pulling forces probably mediated by dynein pulling on astral microtubules (Aist et al., 1993; Grill et al., 2001; Yu et al., 2019). As can be inferred, anaphase is a process relying on several mechanisms that can all be active in the same cell.
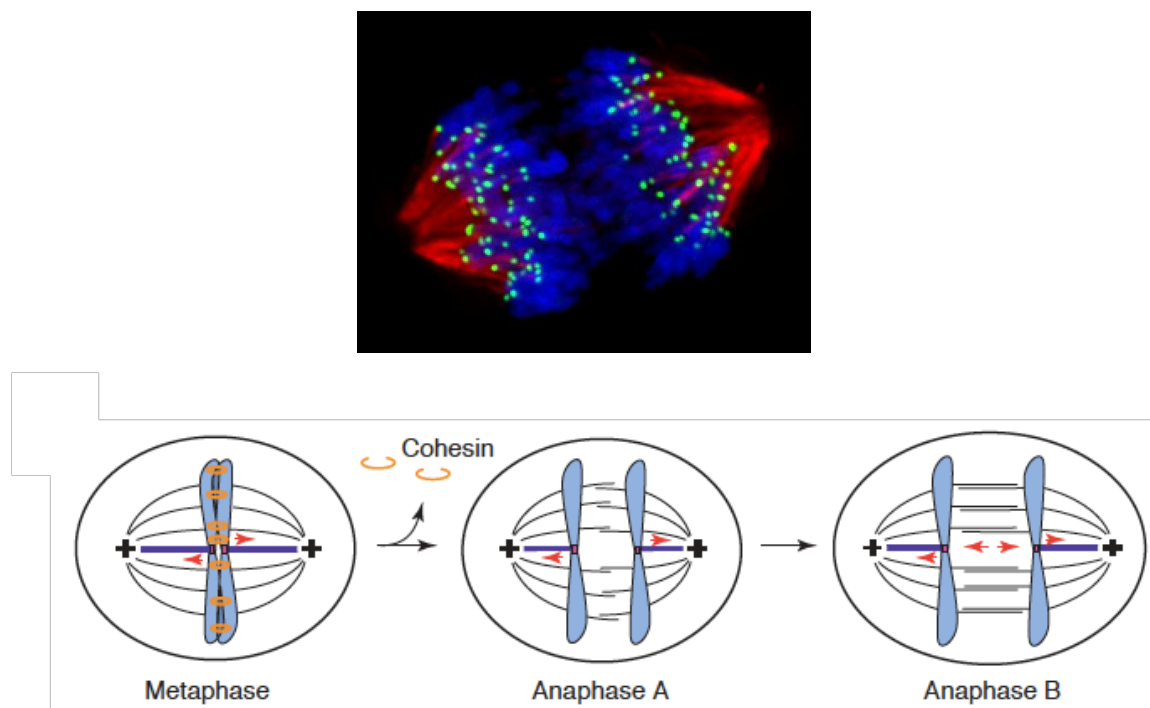
Figure 10. Anaphase of mitosis. Anaphase spindle in a human cell with tubulin shown in red, kinetochores in green and DNA in blue (top). Image downloaded from [warwick.ac.uk]. Illustration of two basic mechanisms involved in chromosome movements during anaphase: depolymerization of k-fibers (anaphase A) and separation of spindle poles driven by sliding of antiparallel microtubules (anaphase B) (bottom). Image from de Gramont and Cohen-Fix (2005).

2.3.5 Telophase

By the end of anaphase segregated daughter chromosomes are located at the opposite sides of the cell. The events of telophase, the final stage of mitosis can be interpreted as a reversal of those occurring in prophase, since in telophase the mitotic spindle disassembles and two sets of chromosomes become packaged in daughter nuclei by re-formation of nuclear envelopes around them (**Fig. 11**). Once nuclear envelope is reassembled, nuclear pore complexes incorporate into the envelope and transport nuclear proteins back in, while chromosomes decondense and reorganise into their interphase state, thus allowing for the gene transcription to continue (Alberts et al., 2017). Chromosome separation and the events of telophase need to be precisely spatially and temporally coordinated to ensure that each new daughter cell receives equal and proper number of chromosomes (Afonso et al., 2014).
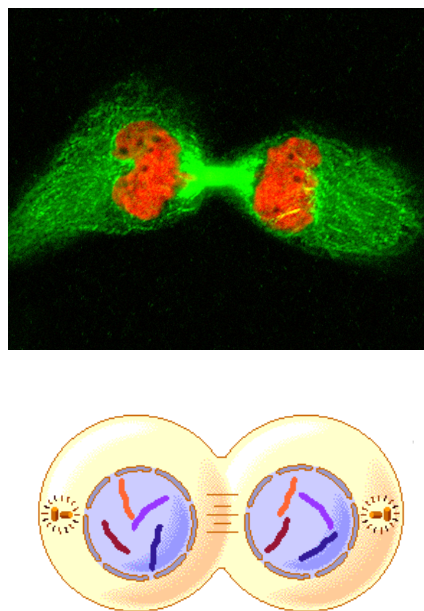
Figure 11. Telophase of mitosis. Human cell in telophase of mitosis with tubulin shown in green and DNA in red. Image downloaded from **[**wellcomecollection.org]. Schematic illustration of a cell in telophase, downloaded from [www.quia.com].

Completion of mitosis is followed by the division of cytoplasm or cytokinesis when the contraction of actin and myosin II containing contractile ring finally divides cell in two. At the same time, this event marks the end of the cell cycle and each of two daughter cells now starts its own (Alberts et al., 2017).

2.4 Structure of the metaphase mitotic spindle

The mitotic spindle is a key structure required for mitosis to occur that starts to assemble at the beginning of mitosis, as was mentioned earlier (Prosser and Pelletier, 2017). It is a dynamic and complex self-constructed micromachine built from microtubules and numerous microtubule associated proteins (MAPs) (Pavin and Tolic, 2016).

2.4.1 Microtubules – structure, properties and classes in the spindle

The main structural component of the mitotic spindle are microtubules, noncovalent polymers of α- and β-tubulin heterodimers as a basic building unit. Each microtubule is a hollow tube built from 13 protofilaments formed by head-to-tail stacking of αβ-tubulin heterodimers and lateral interactions between protofilaments (Nogales et al., 1999) (**Fig. 12 A,B**). Note that the number of protofilaments in microtubules assembled *in vitro* from mammalian brain tubulin can vary between 10 and 15, majority containing 14 protofilaments, while those assembled *in vitro* from centrosomes and axonemes as well as those assembled *in vivo* posses preferentially 13 protofilaments (Evans et al., 1985). This way of forming, where all subunits within the protofilament point in the same direction and parallel alignment of protofilaments, gives microtubules a property of structural polarity, with α-tubulin exposed at the slower growing end, named minus (−) and β-tubulin at the other, faster growing, named plus (+) end (**Fig. 12 B**). Beside polarity, another important property of microtubules is their dynamics, which is influenced by the binding and hydrolysis of guanosine triphosphate (GTP) nucleotide. Both tubulins in heterodimer bind GTP, but only in the β-tubulin subunit it can hydrolyse. If the rate of addition of new subunits is high, in the way that new subunits are added before the GTP in the previous ones hydrolysed, the end of microtubule will have GTP-containing subunits forming a *GTP cap* that stabilizes the end and allows for continuous growth. On the other hand, if the rate of additon of new subunits is low, GTP can hydrolyse before addition

of new subunits, which causes conformational change in the tubulin subunits that forces protofilaments to aquire unstable curved shape subsequently leading to microtubule shortening (Desai and Mitchison, 1997). Microtubules are able to stochastically alternate between these states, a property called dynamic instability. The rapid interconversion from growth to shrinkage is known as *catastrophe*, while the opposite event is known as the *rescue*. All these changes occur preferentially at the plus ends of microtubules (**Fig. 12 C**) (Mitchison and Kirschner, 1984).
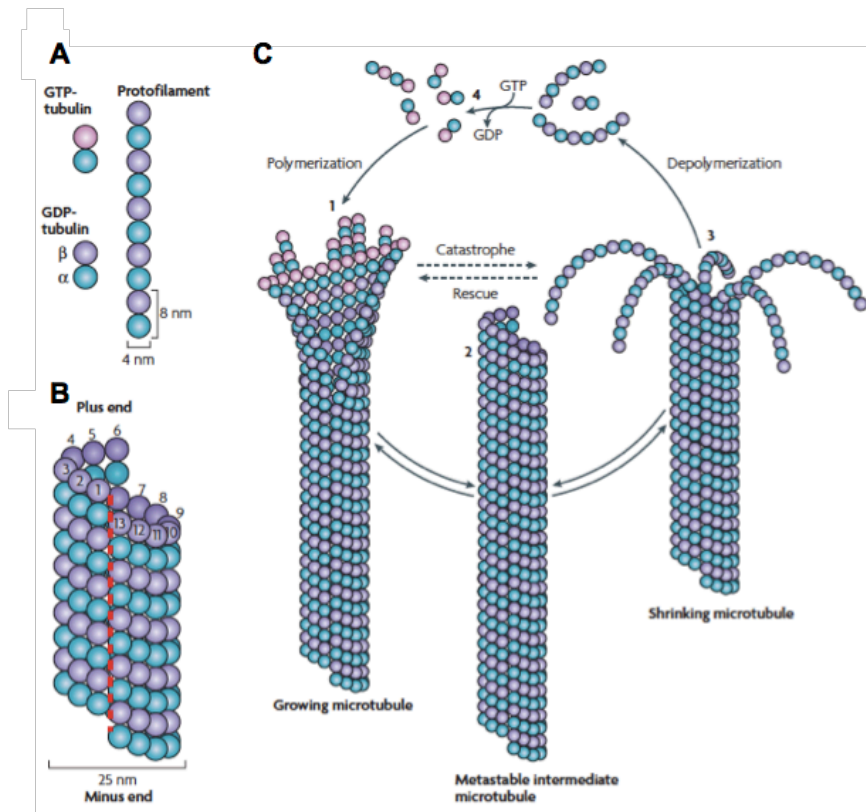
Figure 12. Structural and dynamic properties of microtubules. A. The basic structural units of microtubules are αβ-tubulin heterodimers that arrange head-to tail forming a protofilament. **B.** Protofilaments connect laterally folding into a tube this way making a microtubule. Microtubules have the property of structural polarity that originates from the way of stacking of αβ-tubulin heterodimers so that α-tubulin is exposed at the minus end, and β-tubulin at the plus end. **C.** Microtubules are dynamic structures that can switch between states of growth and shrinkage. This property of dynamic instability is defined by the binding of GTP, where its hydrolysis changes the conformation of tubulin subunits leading to formation of curved protofilaments and their depolymerisation. Image from Akhmanova and Steinmetz (2008).

In the spindle, microtubules nucleate at the centrosomes that function as microtubule organising centers (MTOCs) in majority of animal cells. This process requires the third type

of tubulin called γ-tubulin as a template for nucleation. Microtubules of the spindle are formed in the way that their minus ends remain focused at the pole, while plus ends extend outwards. The mitotic spindle itself is built from hundreds of microtubules that can be sub-divided in populations based on the differences in their structure, dynamics and function (**Fig. 13**) (Alberts et al., 2017). Kinetochore microtubules form parallel bundles or k-fibers that end at kinetochores. In human HeLa cells k-fibers consist of 17 microtubules, on average, as revealed by electron microscopy (McEwen et al., 2001; Wendell et al., 1993). K-fibers are the most stable population in the spindle as they are resistant to perturbations like cold-treatment, whereas all others disassemble (Rieder, 1981). Non-kinetochore microtubules are all those that do not end at kinetochores. These include astral microtubules that extend from the pole towards the cell cortex and help position the spindle within the cell; so called polar microtubules that grow toward equator, but have free ends; and those that form antiparallel overlaps in the middle, called overlap or interpolar microtubules (Tolic, 2018).

U2OS, CenpA-GFP, tubulin-AF-594
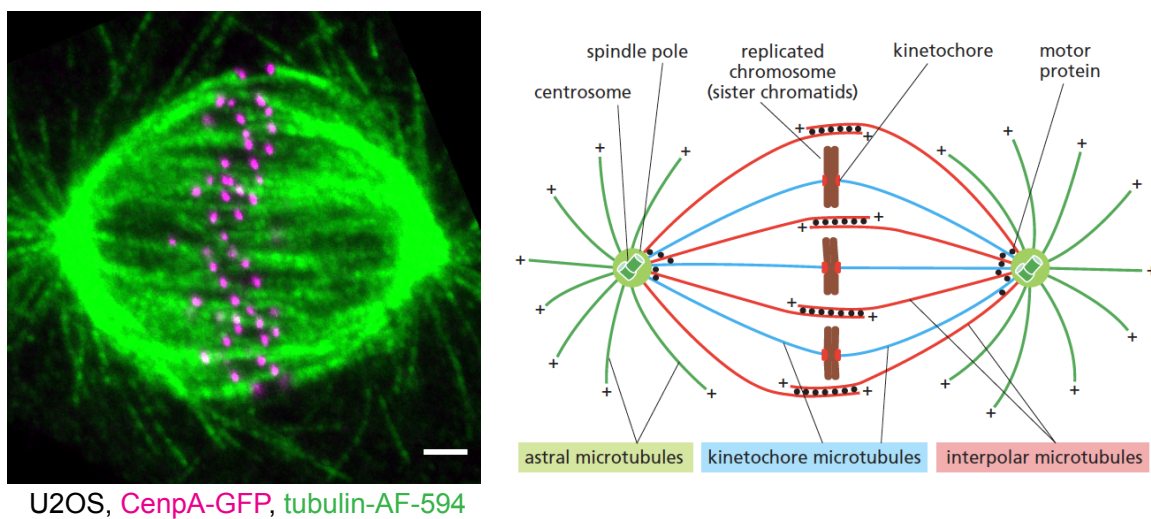
Figure 13. Structure of the metaphase mitotic spindle in animal cells. Metaphase spindle (left) in U2OS cell expressing CenpA-GFP (magenta) and immunostained for tubulin (AF-594, green). Scale bar; 2 μm. Textbook scheme of the mitotic spindle (right) from Alberts et al. (2017). Mitotic spindle is built from several microtubule populations: kinetochore microtubules that form parallel bundles or k-fibers that end at kinetochore, interpolar microtubules that extend from opposite poles and form a region of antiparallel overlap in the midzone, and astral that radiate from the pole towards cell cortex.

2.4.1.1 Bridging fibers – an update to the textbook images of the spindle

The basic 'textbook' structure of the mitotic spindle so far was mainly depicted as in Fig. 13, where k-fibers and interpolar microtubules are completely separate and independent populations of microtubules. However, electron microscopy studies gave a more detailed insight into the structure of the spindle regarding microtubule spatial organisation and interactions between different microtubule populations. Non-kinetochore microtubules were observed extending along k-fibers, passing kinetochore and ending between sister kinetochores in electron micrographs of human WI-38 cells (McIntosh and Landis, 1971), HeLa (Nixon et al., 2017) and RPE-1 cells (O'Toole et al., 2020), as well as PtK cells (O'Toole et al., 2020) and non-mammalian systems, plant endosperm (Jensen, 1982), *Drosophila* S2 cells (Strunov et al., 2018) and *Xenopus* egg extract (Ohi et al., 2003) (**Fig. 14**). Also, minus ends of non-kinetochore microtubules were found to be distributed along k-fibers (Mastronarde et al., 1993). At that point, it was not completely clear whether these populations are merely in the close proximity of each other or they are indeed phisically linked. The latter would have profound implications on the force-balance within the spindle and forces acting on chromosomes, since the forces arising from interpolar microtubules could be transmitted to k-fibers in this way.
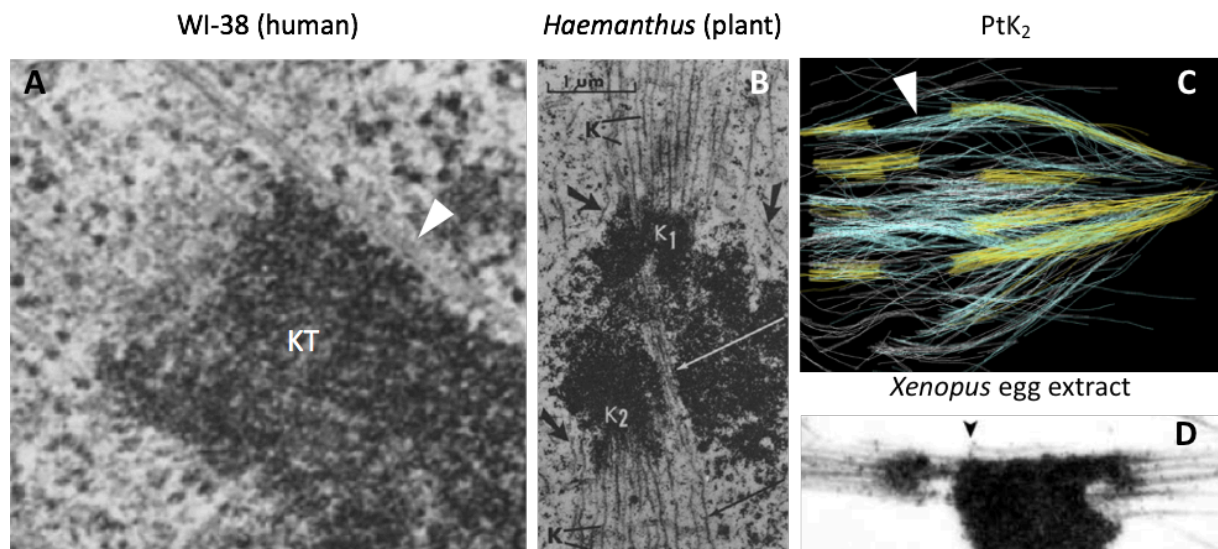
Figure 14. Examples of metaphase spindles from different organisms obtained with electron microscopy, where interpolar microtubules are observed in the close proximity of k-fibers and kinetohores. A. Interpolar microtubules in proximity of kinetochore in human WI-38 cell (indicated

with white arrowhead). Image from McIntosh and Landis (1971). **B.** Area around pair of sister kinetochores (K1 and K2) in endosperm of *Haemanthus* plant. Microtubules of k-fibers (K) are visible ending at kinetochores, but also a population that intermix with them and enters area between kinetochores (long arrows). Image from Jensen (1982). **C.** Tomographic reconstruction of spindle in PtK$_2$ cell. Interpolar microtubules (blue) are clearly visible in the vicinity of k-fibers (yellow) and in the region between their plus-ends. Image from O'Toole et al. (2020). **D.** K-fibers lateraly associated with population of microtubules that do not end at kinetochores (black arrowhead) in *Xenopus* egg extract spindle. Image from Ohi et al. (2003).

The relationship between k-fibers and interpolar microtubules was explored only recently. Similar observations were made by fluorescence microscopy where bundles of interpolar microtubules were seen connecting k-fibers of sister kinetochores in metaphase spindles acting as a bridge between them and therefore they were named the *bridging fibers* (**Fig. 15 A**) (Kajtez et al., 2016). Laser ablation experiments in HeLa, PtK$_1$ and U2OS cells demonstrated tight physical coupling of k-fibers and bridging fibers, as they moved outward together as a single mechanical unit after k-fiber cutting (Buda et al., 2017; Kajtez et al., 2016; Milas and Tolić, 2016) (**Fig. 15 B**). Physical modelling revealed bridging fibers are key structural elements that balance forces on kinetochores and at the poles, enabling the spindle to obtain its round shape and maintaining the tension between sister kinetochores, which has physiological relevance for the cell as tension is monitored by the SAC (**Fig. 15 C**) (Kajtez et al., 2016; Musacchio and Salmon, 2007). These predictions were supported by observations that cells with thicker bridging fibers have more round shape compared to those with thinner ones (Kajtez et al., 2016). Furthermore, laser cutting experiments of k-fibers at different distances from kinetochore resulted in greater reduction of tension for cuts closer to kinetochore (less than 1 μm away) as interactions between bridging fiber and k-fiber were lost (Milas and Tolić, 2016). Additionally, laser ablation experiments of outer k-fibers in early anaphase demonstrated kinetochores are able to separate without connection to one pole, but not if the bridging fiber between them was ablated also, thus revealing the role of bridging fibers in driving spindle elongation in anaphase through microtubule sliding which is driven by plus-end directed motors localized within the bridge (Vukusic et al., 2017; Vukusic et al., 2019a).
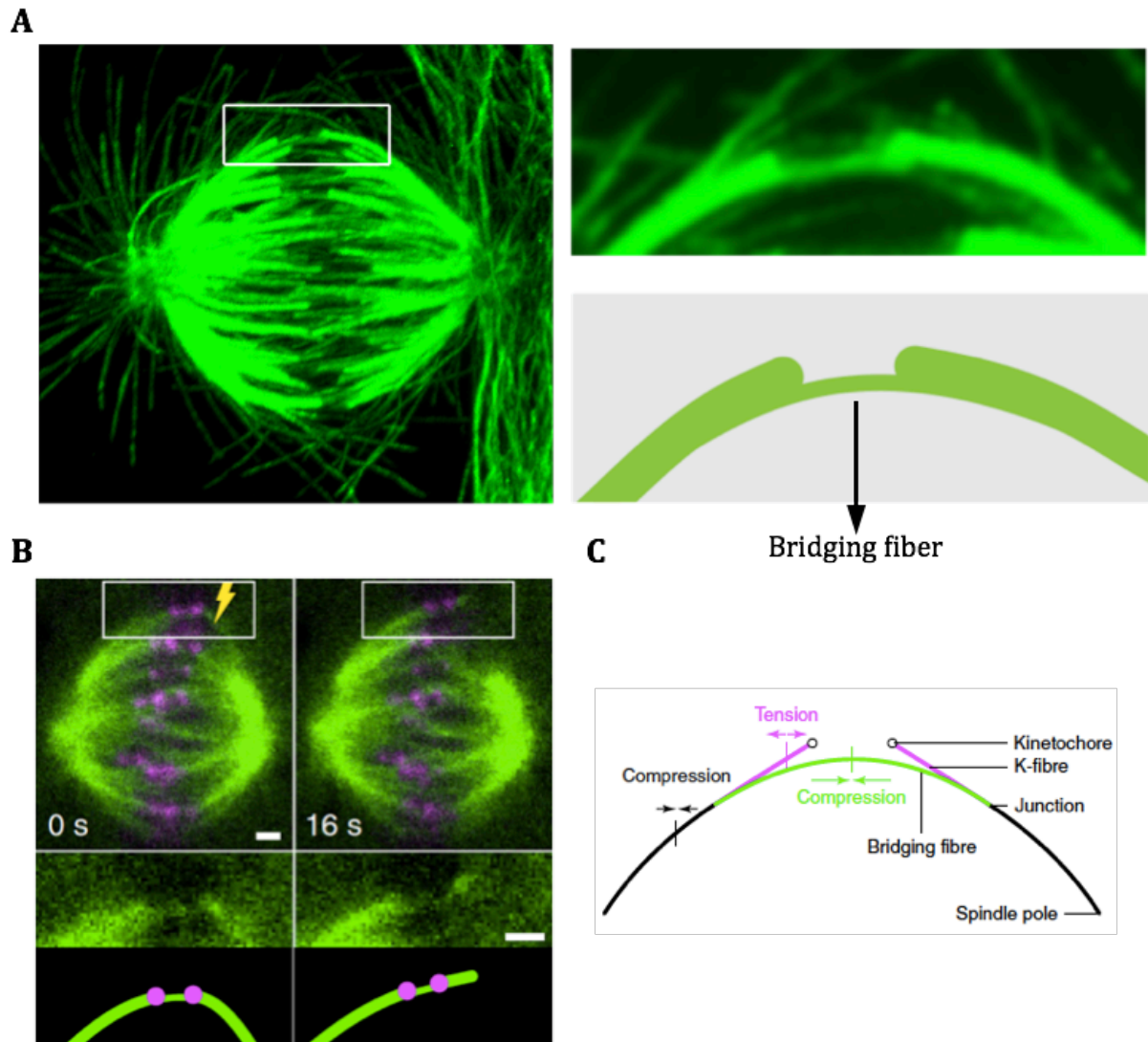
Figure 15. Bridging fibers connect sister k-fibers and balance the forces within the spindle. A. Expansion microscopy image of tubulin (green) in metaphase spindle in RPE-1 cell. Enlargement of the boxed region where bridging fiber is visible (black arrow) and the scheme are given on the right. (Image taken by Ivana Ponjavić). **B.** Time lapse of spindle in HeLa cell expressing tubulin-GFP (green) and mRFP-CENP-B (magenta) (top) and enlargements of the boxed region (middle: GFP, bottom: schemes). After severing of k-fiber (yellow lightning), bridge moved outward together with k-fiber proving they are tightly physically linked in one structural element. Image from Kajtez et al. (2016). **C.** Scheme of a model where bridging fibers balance the tension on kinetochores and compression at the poles enabling simultaneous existence of both compression and tension in the k-fiber. Image from Kajtez et al. (2016). Scale bars: 1 μm.

2.4.2 Microtubule associated proteins (MAPs)

MAPs are proteins that interact with microtubules and can function as their stabilizers, destabilizers, capping proteins and bundling/crosslinkers (Alberts et al., 2017). Within the spindle, the most important MAPs can be classified into motor proteins, kinesins and dynein, main force generators in the spindle that move along microtubules toward plus or minus ends of microtubules by converting chemical energy stored in ATP; passive proteins that for example crosslink microtubules, and various proteins that act as regulators of function of other proteins, like protein kinases (Cross and McAinsh, 2014; Maiato et al., 2004b). Also, MAPs are known to be involved in regulation of microtubule dynamics, with some of them promoting microtubule polymerization and stability, while others induce depolymerization (Maiato et al., 2004b).

2.4.2.1 Protein regulator of cytokinesis 1 (PRC1)

PRC1 is a conserved non-motor MAP from Ase1/PRC1/MAP65 family that selectively crosslinks and bundles MTs in an antiparallel orientation *in vitro* (Bieling et al., 2010b; Janson et al., 2007; Mollinari et al., 2002; Subramanian et al., 2010). These diffusible MT cross-linkers can regulate motor-driven MT sliding through mechanisms such as mechanical friction (Braun et al., 2011; Forth et al., 2014; Janson et al., 2007; Subramanian et al., 2010). It has been shown that Ase1 confined within overlaps can produce entropic expansion forces, analogous to gas molecules confined in a cylinder by a piston. These forces were shown to be strong enough to induce sliding of microtubules with respect to each other, which could have implications in regulation of motor-driven sliding of midzone microtubules (Lansky et al., 2015). Such entropic overlap expansion was not observed for human ortholog PRC1 (Gaska et al., 2020; Wijeratne and Subramanian, 2018), that seems to rather operate in a 'leaky' piston mode as it exhibits higher off diffusion rates on microtubule ends compared to Ase1. Human PRC1 is proposed to act more as a dashpot that provides viscous resistance to motion in a way proportional to velocity (Gaska et al., 2020).

Structure of PRC1 protein consists of four domains: a dimerization domain, rod domain, spectrin domain and an unstructured C-terminal domain (Kellogg et al., 2016; Subramanian et al., 2010) (**Fig. 16 A**). PRC1 forms homodimers that adopt long rod-shaped conformation that bind microtubules in a particular way so that average distance between crossed antiparallel filaments is ~35 nm and the angle 70° relative to microtubule surface

(Kellogg et al., 2016; Subramanian et al., 2013; Subramanian et al., 2010) (**Fig. 16 B**). The rod domain in flexible when PRC1 is attached to a single microtubule, but adopts rigid conformation when crosslinking two antiparallel microtubules (Kellogg et al., 2016; Subramanian et al., 2013; Subramanian et al., 2010). Charge-dependent MT binding is mediated by structured spectrin and Lys/Arg rich C-terminal unstructured domain at the end of each homodimer (Subramanian et al., 2010), while N-terminal domain has a dual function in mediating key protein-protein interactions, like those with kinesin-6 and kinesin-4 (Kurasawa et al., 2004), and enabling PRC1 homodimerization (Subramanian et al., 2013).
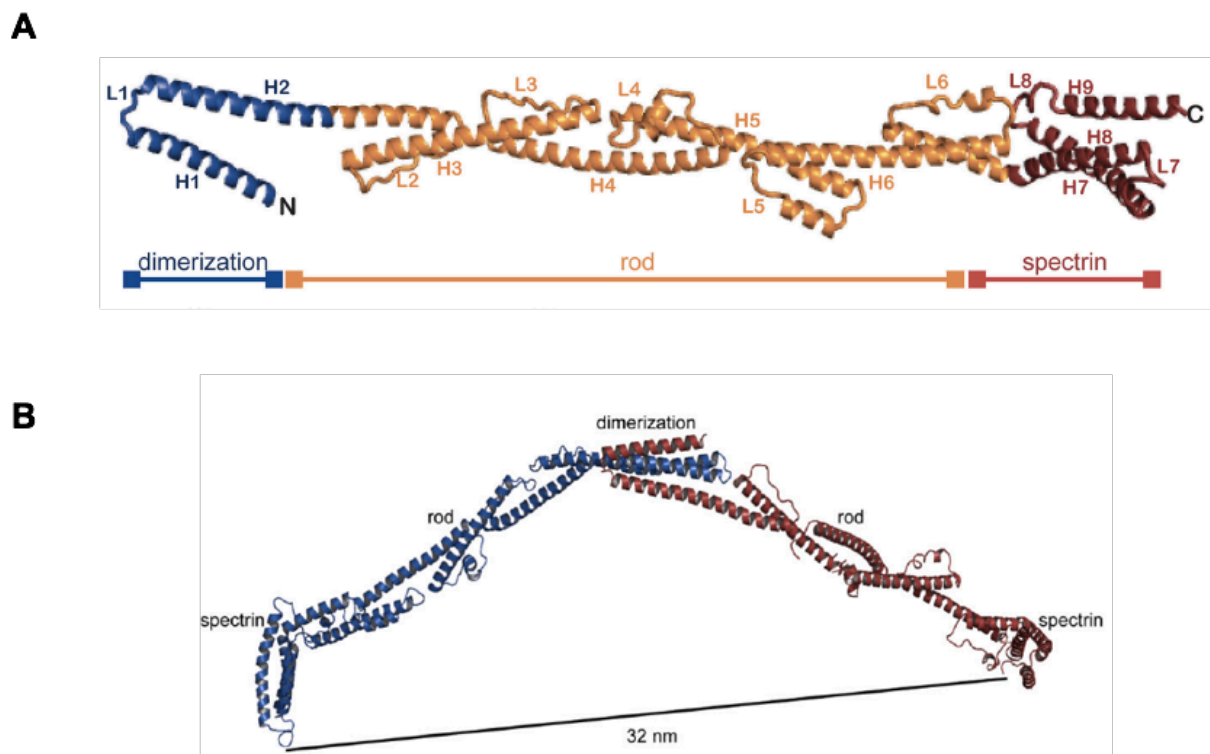
Figure 16. Structure of the PRC1 protein. A. Ribbon diagram of PRC1 structural domains. PRC1 consists of a dimerization, central rod domain, spectrin domain and unstructured Lys/Arg rich domain. Image from (Subramanian et al., 2013). **B.** Ribbon diagram of a PRC1 homodimer consisting of two monomers indicated in red and blue. Image from Subramanian et al. (2013).

In the metaphase spindle, PRC1 is enriched in the overlap bundles (Mollinari et al., 2002) specifically marking anti-parallel regions of the bridging fibers (Kajtez et al., 2016; Polak et al., 2017) (**Fig. 17**). As remodelling of these MT bundles occurs in anaphase, PRC1 becomes associated with the central spindle where its bundling activity is essential for stable MT

organization and successful progression of cytokinesis (Jiang et al., 1998; Kurasawa et al., 2004; Liu et al., 2009; Mollinari et al., 2002; Mollinari et al., 2005; Zhu and Jiang, 2005).
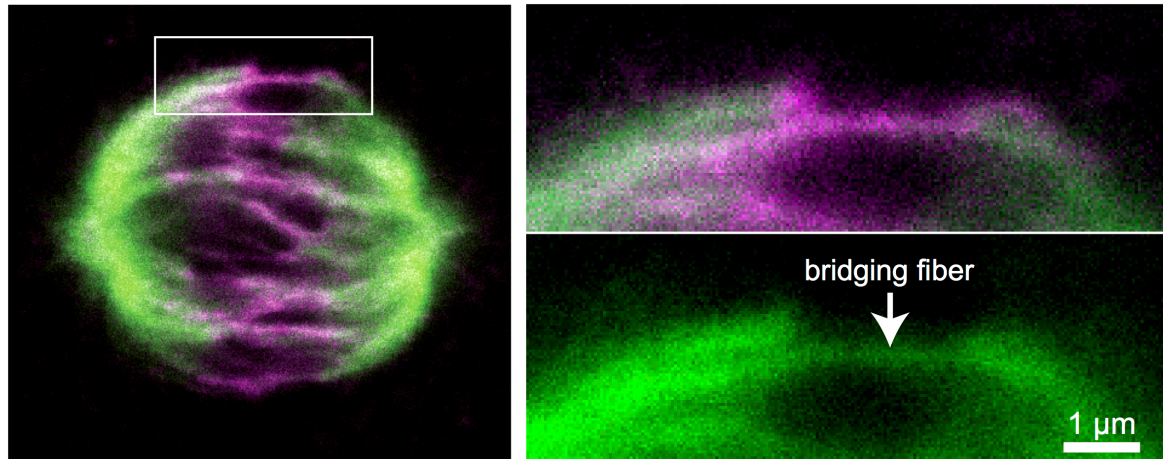
Figure 17. PRC1 localizes in the bridging fibers in metaphase. Image of HeLa cell stably expressing tubulin-GFP (green) immunostained for endogneous PRC1 (Alexa Fluor-555, magenta). Enlargements of the boxed region (right); top, merge; bottom, GFP. Image adapted from Polak et al. (2017).

During mitosis, the MT-binding and -bundling affinities of PRC1 are precisely regulated by phosphorylation and dephosphorylation events. In early mitosis, PRC1 is phosphorylated by CDK1/cyclin B at Thr-470 and Thr-481, thereby decreasing its affinity for MTs or preventing its dimerization (Jiang et al., 1998; Mollinari et al., 2002; Subramanian et al., 2010; Zhu et al., 2006). During metaphase-to-anaphase transition, CDK1/cyclin B becomes inactive due to cyclin B degradation, allowing PP2-B55 phosphatase to remove inhibitory phosporylation on PRC1 (Cundell et al., 2013). Additionaly, PRC1 is phosphorylated by Plk1 at Thr-578 and Thr-602, which promotes Plk1 recruitment by PRC1 to the central spindle (Neef et al., 2007). More recent study suggested that Plk1 negatively regulates PRC1 in metaphase to prevent premature central spindle formation (Hu et al., 2012).

Dephosphorylated PRC1 is required to localise many MAPs associated with the central spindle. Immunoprecipitation and *in vitro* binding experiments showed that PRC1 directly binds to Kif4A/kinesin-4, MKLP1 and MKLP2 from kinesin-6 family, and CENP-E/kinesin-7 in late mitosis (Gruneberg et al., 2006; Kurasawa et al., 2004). These interactions are required for recruitment of Kif4A to the central spindle to ensure proper midzone formation and cytokinesis (Kurasawa et al., 2004; Zhu and Jiang, 2005). PRC1 and Kif4A

were shown to form end-tags at the end of single microtubules, with intensity and size of these end-tags being proportional to microtubule length (Subramanian et al., 2013). *Xenopus laevis* PRC1 was shown to recruit kinesin-4 Xklp-1 to overlaps that inhibited microtubule plus-end growth (Bieling et al., 2010b). Similar *in vitro* experiments and modeling with human PRC1 and Kif4A/kinesin4 demonstrated they are sufficient for assembly of a minimal anaphase-like midzone bundles with Kif4A regulating their length in an overlap length-dependent manner (Hannabuss et al., 2019). PRC1 was also shown to physically interact with cytoplasmic linker associated protein 1 (CLASP1), which is required for stable antiparallel microtubule organization and faithful chromosome segregation (Liu et al., 2009).

2.5 Mechanisms involved in chromosome alignment at the metaphase plate

2.5.1 Polar ejection force (PEF)

Poleward chromosome movements driven by microtubule depolymerization are opposed by PEFs that push chromosome arms anti-poleward, towards spindle equator (McIntosh et al., 2002; Rieder et al., 1986; Rieder and Salmon, 1994). PEFs are exerted by interactions between spindle microtubules and the chromosome arms, with anti-poleward forces generated by polymerizing microtubules that push against chromosome arms or by chromokinesin motors, proteins that associate with both microtubules and chromosomes (**Fig. 18 A**) (Bajer et al., 1982; Brouhard and Hunt, 2005; Rieder et al., 1986). With the increasing microtubule density towards the spindle poles, PEFs increase, which makes these forces essential for positioning chromosomes at the spindle equator (**Fig. 18 B**) (Cane et al., 2013; Ke et al., 2009).
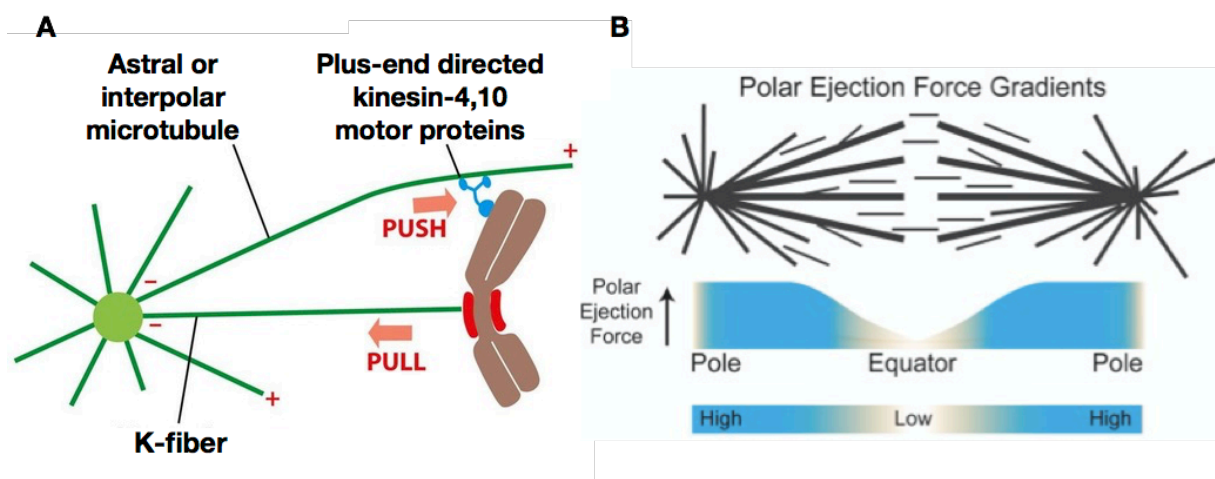
Figure 18. Role of PEFs in chromosome alignment. A. PEFs are exerted by plus-end directed chromokinesin motors bound to chromosome arms. Their movement toward plus-ends of astral or interpolar microtubules interacting with chromosome arms creates force that opposes to pulling force generated by k-fiber plus-end depolymerization [https://quizlet.com/74210217/chapter-x-microtubules-flash-cards/]. **B.** A model of PEF gradients within the spindle: in the proximity of poles, the microtubule density increases and so does PEFs, thus preventing chromosomes to move close to the poles, far from the equator. Image from Cane et al. (2013).

Generation of PEFs is mediated by chromokinesins namely kinesin-4 and kinesin-10 family proteins (**Fig. 18 A**). It was shown that co-operation between these plus-end directed motors contributes to PEFs to a larger extent than pushing generated by polymerizing microtubules (Barisic et al., 2014). With an active role in generation of PEFs, chromokinesins exert forces on chromosome arms involved in chromosome congression, orientation, and oscillation (Antonio et al., 2000; Brouhard and Hunt, 2005; Funabiki and Murray, 2000; Wandke et al., 2012). As individual depletions of KID/kinesin-10 and Kif4A/kinesin-4 have minor effect on chromosome alignment, yet co-depletion gives rise to conspicuous defects, KID and Kif4A have independent and coordinated functions in PEF generation (Wandke et al., 2012). KID is thought to be important for chromosome arm orientation whereas Kif4A regulates microtubule plus-end dynamics (Levesque and Compton, 2001; Wandke et al., 2012). However, role of KID in generation of PEFs becomes evident only upon perturbation of microtubule dynamics, e.g. when co-depleted with Kif4A or Kif18A (Stumpff et al., 2012).

2.5.2 Poleward flux

Poleward flux, defined as a continuous translocation of microtubules towards spindle poles, is an evolutionarily conserved phenomenon in metazoan cells (Forer, 1965; Mitchison, 1989). Molecular mechanisms responsible for this process are not yet fully elucidated. One model proposes flux is driven by Kif2a/kinesin-13 mediated depolymerization at spindle poles with simultaneous CLASP-mediated polymerization at kinetochore microtubule plus-ends (Ganem et al., 2005; Maiato et al., 2005). Different model explains origin of poleward flux as a downstream response to kinesin-5 driven sliding of antiparallel interpolar microtubules, which could be subsequently transmitted to kinetochore microtubules due to their coupling mediated by different crosslinking molecules (Brust-Mascher et al., 2009; Miyamoto et al., 2004). However, inhibition of kinesin-5 in mammalian cells led to only minor reduction of

flux rates, suggesting kinesin-5 is not a predominant generator of flux-driving force in mammalian spindles (Cameron et al., 2006). Recently, it was proposed that poleward flux is driven consecutively from prometaphase to metaphase by CENP-E/kinesin-7 at kinetochores and Kif4A/kinesin-4 on chromosome arms, respectively, and the distribution of flux across the spindle is achieved by coupling of non-kinetochore and kinetochore microtubules (Steblyanko et al., 2020).

Rates and functions of flux differ widely in different cell types. There is almost clear distinction between mitotic systems, where flux rates are relatively slow and contribute to anaphase chromosome poleward movement only to a minor extent, and meiotic, where flux rates are equal or exceed the rates of poleward chromosome movements (Desai et al., 1998; LaFountain et al., 2004). Microtubule flux has been implicated in regulation of spindle length (Maiato et al., 2005; Rogers et al., 2004), correction of erroneous kinetochore-microtubule attachments (Ganem et al., 2005), regulation of kinetochore activity (Maddox et al., 2003), and equalization of forces at kinetochores prior to segregation (Matos et al., 2009). Furthermore, in insect spermatocytes and *Drosophila*, flux represents mechanism important for chromosome alignment (LaFountain et al., 2004; Rogers et al., 2004). In contrast, in human cells alignment as well as periodicity and extent of oscillations were unimpaired upon flux inhibition, suggesting that in human cells other mechanisms ensure chromosome alignment (Ganem et al., 2005). Interestingly, inhibition of both poleward flux and PEFs through simultaneous suppression of MCAK, Kif2a and KID in human U2OS cells did not prevent chromosome alignment and anaphase, indicating that chromosomes in human cells rely on other mechanisms for finding the centre of the spindle (Ganem and Compton, 2006).

2.5.3 Kinetochore fibers plus-end dynamics

The key player involved in regulation of k-fiber dynamics thus responsible for driving chromosome oscillations is kinesin-8. *In vitro* studies initially characterized kinesins-8 as plus-end-directed motors that can depolymerize microtubules at their plus ends in a length-dependent manner, indicative of their involvement in regulation of microtubule dynamics and length *in vivo* (Mayr et al., 2007; Varga et al., 2006; Varga et al., 2009). In several organisms, kinesin-8 was shown to promote catastrophe and microtubule shortening (Gupta et al., 2006; Mayr et al., 2007; Tischer et al., 2009; West et al., 2002). Furthermore, genetic and RNAi studies indicated that kinesin-8, including human Kif18A, is required for proper mitotic

chromosome alignment (Gandhi et al., 2004; Garcia et al., 2002; Klemm et al., 2018; Mayr et al., 2007; Stumpff et al., 2008; Stumpff et al., 2012; West et al., 2002).

Depletion of Kif18A results in increased spindle length and loss of inter-kinetochore tension (Mayr et al., 2007; Stumpff et al., 2008). Quantitative tracking of kinetochore positioning indicated that Kif18A limits kinetochore movements around spindle equator by affecting both frequency of kinetochore directional switches and velocity of kinetochore movements, although with some conflicting results (Mayr et al., 2007; Stumpff et al., 2008). It is proposed that Kif18A regulates chromosome positioning by combining its plus-end length-dependent accumulation and concentration-dependent modulation of k-fiber dynamics (Stumpff et al., 2008).

Besides kinesin-8, various MAPs accumulate at the plus-ends of microtubules throughout mitosis. These plus-end-tracking proteins can contribute to regulation of microtubule dynamics by affecting microtubule polymerization and depolymerization, stabilization of microtubule plus-ends, or promoting microtubule rescue and catastrophe, i.e. switch from shrinkage to growth and vice versa (Akhmanova and Steinmetz, 2008; Schuyler and Pellman, 2001).

Among plus-end-tracking proteins, several are implicated in affecting kinetochores once chromosomes are aligned. Mitotic centromere-associated kinesin (MCAK/Kif2c) is a potent diffusible depolymeraze, which localizes on centromeres and kinetochores, thus being a strong candidate for force generation involved in chromosome movements and positioning (Hunter et al., 2003; Wordeman and Mitchison, 1995). Depletion of MCAK leads to chromosome alignment defects, decrease of chromosome oscillation speed and directional coordination between sister kinetochores, without affecting period of oscillations (Jaqaman et al., 2010; Kline-Smith et al., 2004; Wordeman et al., 2007). Based on these results and observation that MCAK preferentially accumulates on leading sister kinetochore, it was suggested that MCAK sets the velocity of chromosome oscillations together with Kif18A. In this model, MCAK depolymerizes microtubules preferentially in the k-fiber of leading kinetochore, whereas Kif18A promotes depolymerization on the trailing kinetochore, thereby providing resistance to sister pair movement (Jaqaman et al., 2010; Kline-Smith et al., 2004).

Upon microtubule attachment, CLASP proteins, CLASP1 and CLASP2, remain localized at kinetochore-microtubule interface (Maiato et al., 2003; Mimori-Kiyosue et al., 2006; Pereira et al., 2006). With their redundant roles in promoting microtubule rescue and suppressing microtubule catastrophe, without affecting overall microtubule polymerization rate, CLASPs act as microtubule stabilizers (Al-Bassam et al., 2010). By stabilizing

kinetochore microtubules, CLASPs increase tension on kinetochores, and decrease both oscillations and microtubule growth (Mimori-Kiyosue et al., 2006). Thus, CLASPs keep kinetochores in tight alignment at the spindle equator.

2.6. Approaches to study functions of mitotic spindle proteins

The common approach in studying the function of a protein of interest is observation of phenotype after its inactivation or removal. In the last two decades, many valuable tools were developed to fulfill this task.

The majority of studies of protein functions in *in vivo* systems still rely on the usage of RNA interference (RNAi), where introduction of double stranded RNAs (dsRNAs) induces gene silencing by targeting corresponding mRNA for degradation. This natural phenomenon is involved in cellular antiviral response, suppression of expression of potentially harmful segments of the genome, such as transposons, which can destabilize the genome acting as insertional mutagens, and control of gene expression (Agrawal et al., 2003; Ito, 2013). Pioneering observations of RNAi or post-transcriptional gene silencing (PTGS) were reported in plants and fungi after introduction of transgenic DNA, treatment with exogenous RNA or viral infection (Dougherty et al., 1994; Napoli et al., 1990; Romano and Macino, 1992; Ruiz et al., 1998; van der Krol et al., 1990), but the underlying mechanism was finally explained in 1998 when Andrew Fire and Craig Mello published a seminal paper identifying long double-stranded RNAs (dsRNAs) as a agents for post-transcriptional sequence-specific gene silencing in *Caenorhabditis elegans* (Fire et al., 1998). In brief, the principle of gene silencing by RNAi in non-mammalian systems is based on introduction of long dsRNAs that are subsequantlly cleaved by cytoplasmic Dicer enzyme into 21-23 bp small interferenig RNAs (siRNAs), that then assemble into RNA-induced silencing complexes (RISCs). The antisense siRNA strand guides RISC toward complementary mRNA molecules, which are cleaved by RISC, leading to a silencing of a specific gene. Since most mammalian systems produce strong aniviral response upon introduction of dsRNAs longer than 30 bp, silencing can be achieved by introducing siRNAs 21-23 bp long without generation of antiviral response (**Fig. 19**) (Caplen et al., 2001; Elbashir et al., 2001).
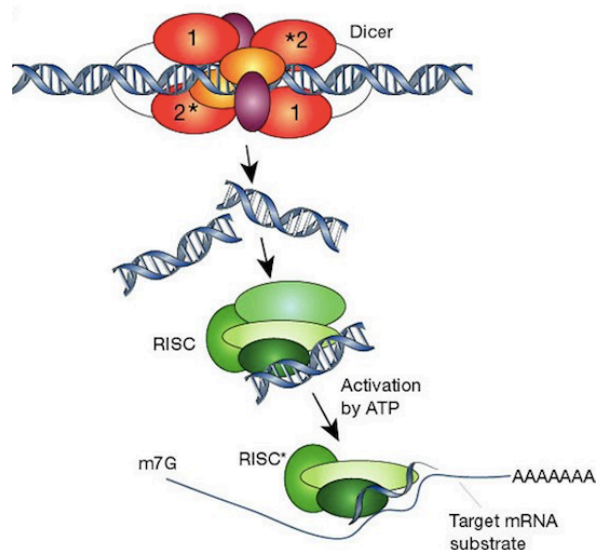
Figure 19. Basic principle of gene silencing by RNAi. The first step in RNAi is production of small interfering RNAs (siRNAs) ~ 22 nt long from dsRNAs by Dicer enzyme. Produced siRNA incorporates into a multicomponent nuclease RISC, which is fully activated after unwinding of siRNA so that antisense strand remains associated with RISC and serves as a guide to its complementary mRNA. Upon recognition, this mRNA is cleaved, which suppresses protein synthesis. Image from Hannon (2002).

For the first time, this approach enabled quick and easy silencing of a particular gene, while availability of quality kits and reagents for performing RNAi made it widely accepted in the research community. However, the effects of this approach are noticeable on a time-scale of days making it difficult to determine whether the phenotypes are a direct consequence of protein depletion or a consequence of earlier defects. Also, this delay between application of siRNA and actual protein depletion can acivate compensatory mechanims, which can modify and/or mask the true phenotype. Furthermore, studying the function of proteins relevant in different phases of mitosis by RNAi can be problematic, e.g. if the protein is relevant for formation of the spindle it is therefore impossible to study its functions in later stages of mitosis. Despite these limitations, RNAi revolutionized molecular biology and contributed to important discoveries regarding functions of individual genes and identification of genes involved in controlling complex phenotypes in many model organisms, as well as in mammalian systems.

An improvement compared to RNAi is the knock-out (KO) approach based on the disruption of target genes on the DNA level. It can be constitutive or conditional, triggered upon addition of a chemical compound. One of the systems available for achieving KO is the

inducible CRISPR/Cas9 system, previously used in genome-wide knock-out screens to identify genes involved in viability of cancer and pluripotent stem cells, as well as genes contributing to resistance to certain compunds and drugs (Shalem et al., 2014; Wang et al., 2014). Recently, generation of hundreds of CRISPR/Cas9 inducible KO cell lines for genes involved in various cell-cycle related processes was reported (McKinley and Cheeseman, 2017). Each of these cell lines stably expresses single guide RNA (sgRNA) that targets exon of the gene of interest, and doxycycline-inducible Cas9 nuclease. Upon induction, double-strand breaks are generated in the target gene, which repair by error-prone non-homologous end joining, thus disrupting function of the gene (**Fig. 20**) (McKinley and Cheeseman, 2017). Although this approach achieves better protein depletion compared to RNAi, the induction is irreversible and requires several days for protein levels to decrease. Over this time secondary compensatory effects can occur, affecting the phenotype. Also, there are reports of some cells escaping the cutting or repairing the cuts without the disruption of a gene (McKinley et al., 2015).
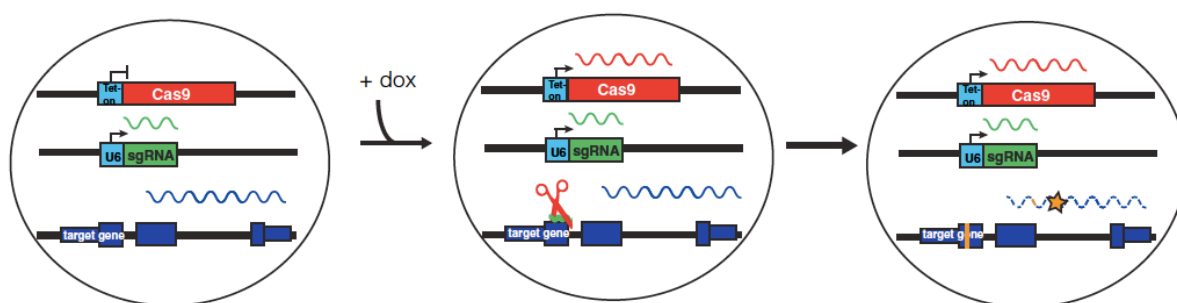
Figure 20. Principle of inducible CRISPR/Cas9 KO. Addition of doxycycline induces expression of Cas9 nuclease that makes double strand brakes in the target gene, navigated by sgRNA. Brakes repair by non-homologous end joining, thus disrupting gene structure and expression. Image from McKinley and Cheeseman (2017).

Ever since new approaches were developed and improved in order to achieve more precise manipulation of protein level, activity or localization to elucidate its function more accurately. An ideal approach should enable reversible manipulation of a specific protein on a time-scale of minutes, in a particular phase of the cell cycle, e.g. mitosis, but also be applicable on different proteins.

One of the common and easy ways of protein inactivation is by small molecule inhibitors, e.g. monastrol is an inhibitor of kinesin-5/Eg-5 (Mayer et al., 1999). This approach enables protein inactivation at a precise moment on a minute time-scale, and allows for

reversibility, which is achieved by simple washout of inhibitor. However, application of inhibitor is impossible without affecting all cells in the dish. Also, production of an inhibitor that would be specific for a certain protein is a long, laborious and expensive process. Very often one inhibitor can have undesireable off-target effects on other kinesins, depending on its working concentration. Therefore, application of inhibitors in studying protein functions is limited by the availability of inhibitors specific for a protein of interest.

Another group of approaches is also based on administration of small molecules, which affect protein stability or localization. One of them is the auxin-inducible degron (AID) system where post-translational degradation of proteins of interest is achieved by addition of a plant hormone auxin. The idea came from the discovery of a naturally present pathway in plants, where hormone auxin induces degradation of AUX/IAA family of transcription repressors by promoting interaction between F-box protein TIR1 component of Skp1, Cullin, and F-Box (SCF) E3 ubiquitin ligase and proteins containing an auxin-inducible degron (AID). The SCF family of ubiquitin ligases exists also in non-plant systems, TIR1 component of SCF and AID however, need to be added. By tagging the protein of interest with AID and adding TIR1, which incorporates in the SCF ligase, protein of interest is degraded upon addition of auxin (**Fig. 21**) (Nishimura et al., 2009). Auxin-induced degradation was successfully applied in various systems, from yeast cells (Kanke et al., 2011; Nishimura et al., 2009), *Drosophila* (Bence et al., 2017), *Caenorhabditis elegans* (Zhang et al., 2015) to human cells (Holland et al., 2012; Li et al., 2019). In human cells, degradation of tested proteins occured on a minute-time-scale, with near complete degradation achieved after 30 to 120 min, making this approach somewhat limiting for studying mitosis, unless cells are artificially arrested in a particular phase of mitosis (Holland et al., 2012). Also, a minor limitation is addition of auxin affecting all cells in the dish at the same time. Important advantage is reversibility of the approach, which is somewhat slow since it requires *de novo* protein synthesis.
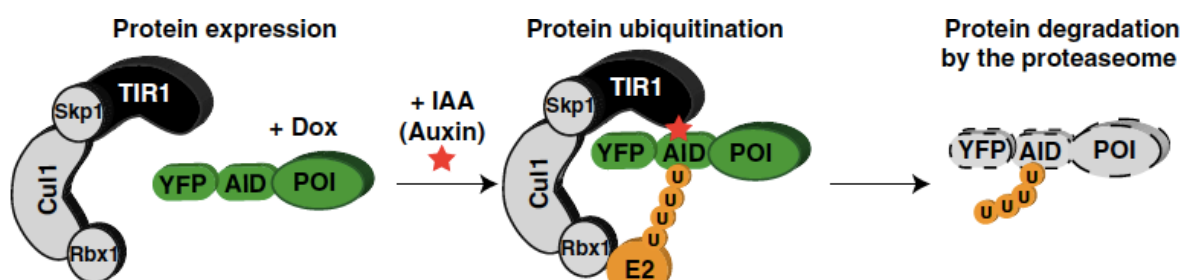
Figure 21. Schematic illustration of auxin induced degradation system. Addition of auxin enables interaction between TIR1 component of SCF ubiquitin ligase and AID degron fused to the protein of interest. SCF-TIR1 acts as an E3 ligase recruiting E2 ligase resulting in polyubiquitylation of AID, which directs target for degradation by the proteasome. Image from Holland et al. (2012).

Knocksideways is a relatively new approach that circumvents most of abovementioned limitations. It is based on chemically induced protein heterodimerization causing rerouting of target proteins to mitochondria on a time-scale of minutes (**Fig. 22**) (Robinson et al., 2010). The signal that activates the system is the drug rapamycin, which normally binds FKBP12, prolyl isomerase, and then this rapamycin-FKBP12 complex binds to a mammalian target of rapamycin (mTOR) kinase. Therefore, if rapamycin binding domains from FKBP12 and mTOR are fused to other proteins, addition of rapamycin can induce their heterodimerization (Robinson and Hirst, 2013). Knocksideways is used as a research tool in studies of endoplasmatic reticulum (ER) and Golgi during mitosis (Pecot and Malhotra, 2004), roles of phosphoinositides in endocytosis and intracellular trafficking (Zoncu et al., 2009; Zoncu et al., 2007) and also in yeast cells, for translocation of nuclear proteins in the cytoplasm (Geda et al., 2008; Haruki et al., 2008). In particular, this method is suitable for studying the role of specific mitotic proteins since it can be applied for various proteins at specific stages of mitosis, as demonstrated for Transforming Acidic Coiled Coil 3 (TACC3) protein and MCAK and Kif18A motors (Cheeseman et al., 2013; Wordeman et al., 2016). However, addition of rapamycin affects all the cells in the dish at the same time, and exposure of cells to rapamycin longer than 1 h is not advised, since it could start affecting mTOR signalling (Robinson and Hirst, 2013). Also, translocation of proteins is irreversible once rapamycin is added, which represents the main limitation of this approach.
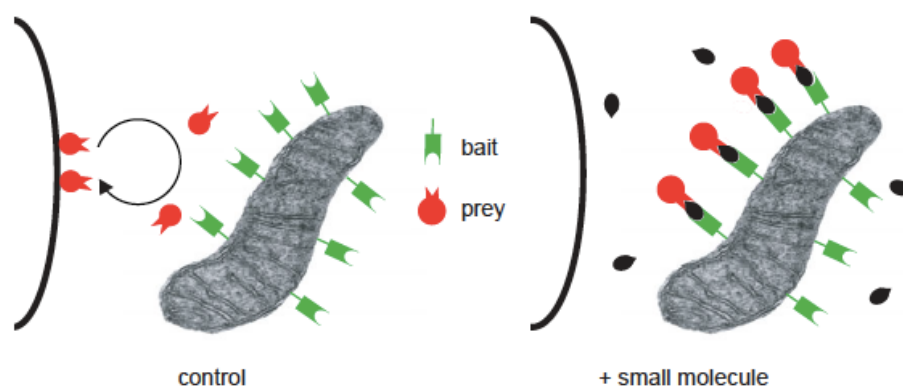
Figure 22. The principle of the knocksideways approach. Domains that bind to a small molecule (in this case rapamycin) are fused both to bait and pray construts. The bait localizes to the mitochondria outer membrane, while pray is a protein of interest wich has some level of turnover between cytosol and its original location in the cell. Addition of rapamycin causes formation of heterodimer between bait and pray, thus trapping the pray on the mitochondrial membrane. Image from Robinson and Hirst (2013).

Trim-Away is a new approach that enables acute depletion of endogenous proteins on the post-translational level, without need for previous protein tagging or modification. It relies on the natural activity of E3 ubiquitin ligase called TRIM21 that is involved in immune response by recognizing antibody-bound pathogens and targeting them for degradation. In the Trim-Away experiment, an antibody is introduced against endogenous target protein, an endogenous or exogenously added TRIM21 is then recruited that recognizes antibody-bound target protein thus triggering the proteasome-mediated degradation of the entire complex (**Fig. 23**) (Clift et al., 2017; Clift et al., 2018). This approach is acute and rapid, enabling protein degradation on the time-scale of minutes and can be applied on any endogenous protein in a wide range of cell types, as demonstrated in (Clift et al., 2017). Also, it is suitable for various model organisms, as it was successfully applied for studying roles of different proteins during zebrafish embriogenesis (Chen et al., 2019).
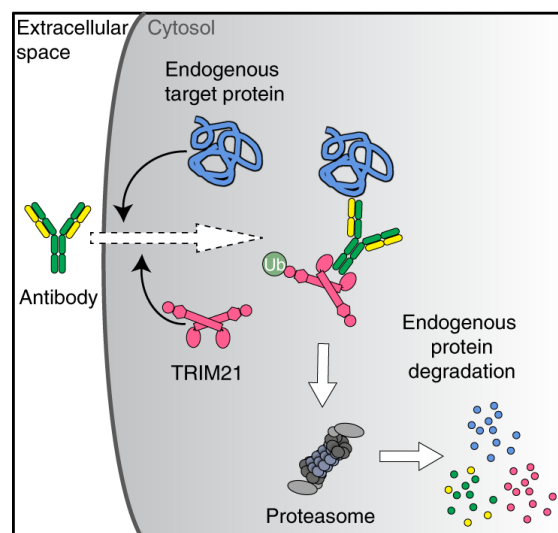
Figure 23. Trim-Away approach for endogenous protein degradation. The Trim-Away approach consists of three critical steps: addition of an antibody specific for a target protein of interest; recognition of antibody-target complex by TRIM21 ubiquitin ligase that targets entire antibody-target-TRIM21 complex for a proteasome degradation. Image from Clift et al. (2018).

A novel elegant technology in the field is optogenetics, which implements different genetic modifications of targeted proteins in order to achieve light-induced control of protein function, reviewed in Dugue et al. (2012). Optogenetic approach was first applied in neuroscience for light-induced control of neuronal activity (Boyden et al., 2005; Nagel et al., 2003). Utilization of light makes this method easily applicable on most setups for fluorescent microscopy and enables fast, reversible, and precise control of protein activity in different cells and tissues. It can be achieved either by causing inhibitory conformational change of targeted proteins (Renicke et al., 2013; Strickland et al., 2008) or by changing protein localization and consequentially its activity (Deisseroth, 2011; Tucker et al., 2014). Inhibition of proteins by conformational change is more challenging since it is necessary to fuse the photosensitive domain to the optimal position specific for each targeted protein. In the second approach, based on a change of protein localization, application of light of a specific wavelength triggers a conformational change of the photosensitive domain fused with a chosen cell structure (usually mitochondria or cell membrane), which causes translocation of the targeted protein from its initial localization in the cell to mitochondria or cell membrane. Currently available systems for light-induced dimerization are based on light-oxygen-voltage (LOV) domain (Guntas et al., 2015; Strickland et al., 2012), plant phytochromes (Levskaya et al., 2009) or cryptochromes (Kennedy et al., 2010), or fluorescent proteins sensitive to light (Zhou et al., 2012).

3. MATERIALS AND METHODS

3.1 Cell lines

Experiments of altering Kif18A levels and laser ablations were performed on human hTERT-RPE-1 (retinal pigmented epithelium, female) premanently transfected and stabilized using CENP-A-GFP and centrin-GFP, which was a gift from Alexey Khodjakov (Wadsworth Center, New York State Department of Health, Albany, NY). Experiments regarding optogenetic removal of PRC1 were performed using: unlabeled human osteosarcoma U2OS cell line and U2OS cell line stably expressing CENP-A-GFP, used in our previous work (Vukusic et al., 2017); which was a gift from Marin Barišić and Helder Maiato (Institute for Molecular Cell Biology, University of Porto, Portugal); U2OS cell line stably expressing 2xGFP-EB3 and mCherry-CENP-A, a gift from Julie Welburn (University of Edinburgh, United Kingdom) (Kajtez et al., 2016); HeLa-Kyoto BAC lines stably expressing MKLP1-GFP, Kif4A-GFP, Kif18A-GFP, CENP-E-GFP and PRC1-GFP were a courtesy of Ina Poser and Tony Hyman (MPI-CBG, Dresden, Germany); unlabeled HeLa-TDS cells from the High-Throughput Technology Development Studio (MPI-CBG, Dresden); HeLa-TDS cells, permanently transfected with pEGFP-α-tubulin, used in our previous work (Kajtez et al., 2016); HeLa cells stably expressing YFP-tubulin, a courtesy of Lars Jansen (University of Oxford, United Kingdom); HeLa cells permanently transfected with EGFP-CLASP1, which was a gift from Helder Maiato (Institute for Molecular Cell Biology, University of Porto, Portugal). Cells were grown in flasks in Dulbecco's Modified Eagle's Medium (DMEM; Lonza, Basel, Switzerland) with 1 g/L D-glucose, L-glutamine, and pyruvate, supplemented with 10% of heat-inactivated Fetal Bovine Serum (FBS; Sigma Aldrich, St. Louis, MO, USA), 100 IU/mL penicillin and 100 mg/mL streptomycin solution (Lonza). For cell lines with stable expression of fluorescently labeled proteins, 50 μg/mL geneticin (Life Technologies, Waltham, MA, USA) was added. Cells were kept at 37°C and 5% CO_2 in a Galaxy 170 R humidified incubator (Eppendorf, Hamburg, Germany). All used cell lines were confirmed to be mycoplasma free by using MycoAlert Mycoplasma Detection Kit (Lonza).

3.2 Plasmids

Kif18A untagged plasmid was purchased (OriGene Technologies, SC324239). To make PRC1-tgRFPt-SspB WT (opto-PRC1) plasmid, PRC1 fragment was amplified from His6-PRC1 plasmid (Addgene number: 69111) (Nixon et al., 2015) using the primers GCTAGAATTGACCGGATGAGGAGAAGTGAGGTGCTG (FWD) and CATGGTGGCGACCGGTAAATTCGAAGCTTGAGCTCGAGATCTGAGGGACTGGAT GTTGGTTGAATTGAGG (REV) and inserted into plasmid tgRFPt-SspB WT (Addgene number: 60415) using *AgeI* restriction site. This step was performed using commercially available *In-Fusion HD Cloning Kit* (Clontech, Mountain View, CA, USA). The produced plasmid expresses PRC1 tagged with tgRFPt and SspB at the C-terminus. Plasmid iLID-CAAX was purchased (Addgene number: 85680) (O'Neill et al., 2016). Plasmids pEGFP-C1Kif4a-sires and EGFP-Kif18A were a gift from Jason Stumpff (University of Vermont, Burlington, VT, USA) (Stumpff et al., 2008; Stumpff et al., 2012). Plasmid GFP-CENP-E was a gift from Marin Barišić (Danish Cancer Society Research Center, Copenhagen, Denmark).

3.3 Sample preparation

For experiments regarding Kif18A, 24 h before imaging RPE-1 cells were transfected with 100 nM *Silencer Select Validated Kif18A siRNA* (s37882; Ambion, Austin, TX, USA) or 5 μg of Kif18A untagged plasmid using Lipofectamine™ p3000 Reagent and Lipofectamine RNAiMAX, respectively (Life Technologies) according to manufacturer instuctions. For depletion of endogenous PRC1 before opto experiments, cells were transfected 72 h (U2OS cells) or 24 h (HeLa cells) prior to imaging with 25 μL of 20 μM *Accell PRC1 siRNA* (A-019491-15-0020, Dharmacon, Lafayette, CO, USA) targeting 3' UTR of PRC1 mRNA. A day prior to imaging, siRNA treated cells were transfected with corresponding plasmids in following amounts: 0.3 μg of iLID-CAAX, 5.5 μg PRC1-tgRFPt-SspB-WT (resistant to the used RNAi), 0.5 μg pEGFP-C1Kif4a-sires, 1 μg EGFP-Kif18A and 1 μg GFP-CENP-E. In HeLa BAC lines, 24 h prior to imaging, mock experiment cells were transfected with 100 nM *Accell Non-targeting Pool* (D-001910-10-05; Dharmacon), PRC1 siRNA treated with 100 nM *Accell PRC1 siRNA* (Dharmacon), Kif4A siRNA treated with 100 nM *Kif4A siRNA* (sc-60888; Santa Cruz Biotechnologies, Dallas, TX, USA), whereas Kif18A siRNA treated with

100 nM *Silencer Select Validated Kif18A siRNA* (s37882; Ambion, Austin, TX, USA). All transfections were performed using Nucleofector Kit R with the Nucleofector 2b Device (Lonza) using X-001 program for U2OS and O-005 (high viability) program for HeLa cells. Following transfection, the cells were seeded on 35-mm glass coverslip uncoated dishes with 0.17-mm (1.5 coverglass) glass thickness (MatTek Corporation, Ashland, MA, USA) in 1.5 mL DMEM medium with appropriate supplements.

To visualize microtubules, cells were stained with silicon rhodamine (SiR)-tubulin (Spirochrome AG, Stein am Rhein, Switzerland) (Lukinavicius et al., 2014), a far-red tubulin dye, at a concentration of 50 nM 12-16 h prior to imaging. To prevent dye efflux, verapamil, a broad-spectrum efflux-pump inhibitor (Spirochrome Ltd.), was added in U2OS and RPE-1 cells at a concentration of 1 μM. To visualize chromosomes and determine the phase of the mitosis, 20 min prior to imaging SiR-DNA (Lukinavicius et al., 2015) (Spirochrome AG, Stein am Rhein, Switzerland) was added to a final concentration of 150 nM. For experiments on U2OS cells expressing 2xGFP-EB3 and mCherry-CENP-A, the cells were synchronized by adding 20 μM of the proteasome inhibitor MG-132 (Sigma-Aldrich) to arrest the cells in metaphase. Imaging was started 15 min after adding MG-132.

3.4 Immunocytochemistry

Cells were fixed with ice-cold methanol for 3 min, washed 3 times with phosphate buffer saline (PBS), followed by 15 min permeabilization with 0.5% Triton in PBS. Cells were washed 3 times with PBS and blocked in 1% Normal Goat Serum (NGS) except in experiment for intensity of opto-PRC1 where cells were blocked in BSA in PBS for 1 h at 4°C. Cells were washed 3 times with PBS and then incubated in primary antibody solution in blocking buffer over night at 4°C. Following primary antibodies were used: mouse anti-PRC1 monoclonal antibody (1:100; C-1; sc-376983, Santa Cruz Biotechnology), rabbit anti-α-tubulin polyclonal antibody (1:100; SAB4500087, Sigma-Aldrich Corporation, St. Louis, MO, USA), mouse monoclonal anti-Kif4A antibody (1:100; E-8; sc-365144, Santa Cruz Biotechnology), rabbit polyclonal anti-MKLP1 antibody (1:100; N-19; sc-867, Santa Cruz Biotechnology), mouse monoclonal anti-Eg5 antibody (1:100; A-1; sc-365681, Santa Cruz Biotechnology). After washing off primary antibodies with PBS, cells were incubated in a solution of secondary antibodies in 2% NGS or BSA in PBS for 1 h at room temperature protected from light. Following secondary antibodies were used: donkey anti-mouse IgG Alexa Fluor 488 (1:250; ab150109, Abcam, Cambridge, UK), donkey anti-rabbit IgG Alexa

Fluor 594 (1:250; ab150064, Abcam), donkey anti-rabbit IgG Alexa Fluor 405 (1:250; ab175649, Abcam), and goat anti-mouse IgG Alexa Fluor 647 (1:250; ab150119, Abcam). After washing off the secondary antibodies 3 times in PBS, cells were incubated with a solution of 4', 6-diamidino-2-phenylindole (DAPI) (1:1000) in PBS for 20 min and washed 3 times in PBS or SiR-DNA (150 nM) in PBS for 15 min before imaging. Note that we used immunocytochemistry for PRC1 rather than Western blot analysis because the efficiency of opto-PRC1 plasmid transfection is low, and as Western blot analysis provides information about the complete cell population, these results may not be relevant for the cells used in the optogenetic experiments. In contrast, by using immunocytochemistry we analyzed only the cells with a similar opto-PRC1 level and in the same phase as those in our optogenetic experiments.

3.5 Microscopy

Immunocytochemistry imaging and live imaging of RPE-1 cells stably expressing CENP-A-GFP and centrin-GFP, unlabeled U2OS, U2OS stably expressing CENPA-GFP, HeLa-TDS pEGFP-α-tubulin and HeLa BAC CENP-E-GFP cells was performed using Bruker Opterra Multipoint Scanning Confocal Microscope (Bruker Nano Surfaces, Middleton, WI, USA), described previously (Buda et al., 2017). In brief, the system was mounted on a Nikon Ti-E inverted microscope equipped with a Nikon CFI Plan Apo VC 100x/1.4 numerical aperture oil objective (Nikon, Tokyo, Japan). During imaging, live cells were maintained at 37°C using H301-K-frame heating chamber (Okolab, Pozzuoli, NA, Italy). In order to obtain the optimal balance between spatial resolution and signal-to-noise ratio, 60-μm pinhole aperture was used. Opterra Dichroic and Barrier Filter Set 405/488/561/640 was used to separate the excitation light from the emitted fluorescence. Following emission filters were used: BL HC 525/30, BL HC 600/37 and BL HC 673/11 (all from Semrock, Rochester, NY, USA). Images were captured with an Evolve 512 Delta Electron Multiplying Charge Coupled Device (EMCCD) Camera (Photometrics, Tucson, AZ, USA) using a 200 ms exposure time. Electron multiplying gain was set on 400. Camera readout mode was 20 MHz. No binning was performed. The xy-pixel size in the image was 83 nm. The system was controlled with the Prairie View Imaging Software (Bruker).

For imaging of kinetochore dynamics and laser ablation experiments, RPE-1 cells were imaged with 488 and 640 nm diode laser lines with 150 ms exposure time. Five z-stacks were obtained every 7 s with 0.5 μm spacing between adjacent z-planes. Laser ablation

experiments were performed using 1030 nm Mikan air-cooled diode-pumped femtosecond oscillator (Amplitude Systems, Pessac, France) with 900 mM power in the spiral mode with spiral revolutions set to 17 and 1500 ms exposure time. The entire setup for ablation is extensively described in (Buda et al., 2017). The size of the region for ablation was set to 800-1000 nm in order to cut individual k-fibers. Cuts were performed on the outermost fibers, because they could be more easily distinguished from the inner ones.

For kinetics experiments on U2OS cells (Fig. 23), 561 and 488 nm diode laser lines were used every 10 s with 200 ms exposure time. In all other optogenetic experiments, stacks were acquired using sequentially the following diode laser lines: 561 nm (to visualize opto-PRC1), 488 nm (to activate the optogenetic system and to visualize GFP), and 640 nm (to visualize SiR-tubulin or SiR-DNA, when applicable), with time interval between z-stacks of 60 s and with 200 ms exposure time per laser line. To prevent dissociation of PRC1 from the cell membrane between acquiring two consecutive z-stacks, only blue light was turned on for 200 ms every 10 seconds. Cells were imaged this way for 20 min in order to achieve almost complete removal of PRC1 from the spindle, after which the blue light was turned off and imaging was continued for another 10 min at 60 s intervals. The total imaging time of 30 min was chosen to be close to the typical metaphase duration of 29.7 ± 2.3 min, which was measured from the metaphase plate formation until anaphase onset in U2OS cells expressing CENP-A-GFP, mCherry-α-tubulin and PA-GFP-tubulin (N=187) imaged after nuclear envelope breakdown every minute by obtaining 15 z-slices with 0.5 μm spacing and 150 ms exposure time. After 30 min of imaging, one z-stack in each of the three channels was taken in order to visualize the spindle and kinetochores after PRC1 return. In all cells except HeLa cells expressing pEGFP-α-tubulin, three focal planes with spacing between adjacent planes of 1 μm were acquired. Live imaging of HeLa cells stably expressing pEGFP-α-tubulin was performed in the same manner as described above for optogenetic experiments. Additionally, before turning the blue light on every 10 s, one z-stack was acquired using 561, 488 and 640 nm diode laser lines with averaging 8, and seven focal planes with spacing between adjacent planes of 0.5 μm. Stack was taken in the same way after 20 min of exposure to the blue light and again 10 min after the blue light was switched off. Imaging of HeLa BAC CENP-E-GFP mock and PRC1 siRNA treated cells was performed by acquiring one z-stack of 3 focal planes with spacing between adjacent planes of 1 μm. For imaging of immunostained cells, 5 focal planes with spacing between adjacent planes of 0.5 μm were acquired.

Live imaging of U2OS cells stably expressing 2x-GFP-EB3 and mCherry-CENP-A was performed on a spinning disk confocal microscope system (Dragonfly, Andor Technology, Belfast, UK) using 63x/1.47 HC PL APO oil objective (Leica) and Zyla 4.2P scientific complementary metal oxide semiconductor (sCMOS) camera (Andor Technologies). During imaging cells were maintained at 37º and 5% CO_2 within H301-T heating chamber (Okolab, Pozzuoli, Italy). Images were acquired using Fusion software (v 2.2.0.38). For excitation, 488-nm and 561-nm laser lines were used for visualization of GFP, and mCherry and opto-PRC1, respectively. In order to achieve PRC1 removal from the spindle, 3 z-planes with a z-spacing of 1 μm were acquired sequentially with both laser lines, every 10 s with 200 ms exposure time for 10 min. This imaging protocol was followed by faster imaging, every 1.5 s with both laser lines on a central z-plane in order to visualize EB3 dynamics. Control, mock and PRC1 siRNA treated cells were imaged with the same imaging protocol.

Live imaging of unlabeled, BAC (except CENP-E-GFP), YFP-tubulin and EGFP-CLASP1 HeLa cell lines was performed on Leica TCS SP8 X laser scanning confocal microscope with a HC PL APO 63x/1.4 oil immersion objective (Leica, Wetzlar, Germany) heated with an objective integrated heater system (Okolab, Burlingame, CA, USA). During imaging, cells were maintained at 37°C in Okolab stage top heating chamber (Okolab, Burlingame, CA, USA). The system was controlled with the Leica Application Suite X software (LASX, 1.8.1.13759, Leica, Wetzlar, Germany). For GFP- and YFP-labeled proteins, a 488-nm and 514-nm Argon laser was used, respectively, and for SiR-DNA or SiR-tubulin, a 652-nm white light laser was used. For AF-647, a 637-nm white light laser was used. GFP, and SiR-DNA, SiR-tubulin or AF-647 emissions were detected with hybrid detector. For mock, PRC1 siRNA, Kif4A siRNA, and Kif18A siRNA experiments, images were acquired at 1–3 focal planes with 1 μm spacing and 0.05-μm pixel size. In optogenetic experiments 3 z-stacks with 1 μm spacing were acquired sequentially every 10 s in the same manner as in optogenetic experiments in U2OS cells. One z-stack with line averaging of 6 or 16 was acquired before system activation, 20 min after exposure to blue light and 10 min after the light was switched off. For FRAP experiments, image acquisition was performed for 100 time frames with 0.3 s intervals using unidirectional xyt scan mode without averaging.

3.6 Image and data analysis

3.6.1 Experiments on RPE-1 cells

The general behavior and movements of kinetochores in control, Kif18 siRNA treated and cells expressing untagged Kif18A were analyzed by tracking their x, y positions using Low Light Trackig Tool (LLTT) pluggin in Fiji software (Krull et al., 2014). Tracking of kinetochores was performed on maximum intensity of 2-3 z-planes. Sigma value (standard deviation of the Gaussian used to approximate the Point Spread Function (PSF) of the tracked objects) was set to *Automatic*. Quantifications were performed in MATLAB (MathWorks, Natick, MA, USA) using home-written script. In brief, coordinates of poles were used to calculate the coordinate of the spindle centre, which was set to correspond to the origin of the coordinate system. Coordinates of all kinetochores were translated and rotated so that long spindle axis is positioned perpendiculary and changes in y coordinates of kinetochores reflect their position with respect to the equatorial plate. Positions of kinetochores before and after laser ablation experiments were tracked using *Segmented Line Tool* in Fiji by obtaining intensity profiles in the GFP channel by drawing a 10 pixel wide line from pole across ablated kinetochore fiber. Before analysis, images were smoothed with 0.5-sigma-radius Gaussian blur.

3.6.2 Optogenetic experiments

Since the cells were transiently transfected with opto-PRC1, we observed variability in PRC1 expression levels and therefore we imaged and analyzed only those metaphase spindles with PRC1 localization consistent with endogenous and fluorescently labeled PRC1 (Kajtez et al., 2016; Polak et al., 2017). Cells were not synchronized in order to avoid additional chemical treatment of cells, and metaphase was determined by alignment of kinetochores in the equatorial plane.

For determination of kinetics of PRC1 removal and return (Fig. 36 C), intensity of opto-PRC1 was measured in each time frame on one focal plane. We used *Poligon selection tool* in Fiji (National Institutes of Health, Bethesda, MD, USA) to encompass the area of the spindle, $A_{spindle}$, and measure mean spindle intensity, $M_{spindle}$. Mean background intensity in the cytoplasm was measured using 30 x 30 pixels rectangle, M_{cyto}. Spindle intensity was background corrected by subtracting M_{cyto} from $M_{spindle}$ to obtain $M_{spindle\ corr}$. In order to

calculate the sum of PRC1 intensity on the spindle, $M_{spindle\ corr}$ was multiplied with $A_{spindle}$ for each timeframe. The background intensity outside of the cell was negligible, thus we did not take it into account. Note that for the measurements of kinetic parameters in Fig. 36 C, four outliers were excluded (see Fig. 36 A). The percentage of PRC1 removal was calculated from the mean value of intensity of all cells at time 20 min, i.e., the last time point of the continuous exposure to the blue light. The percentage of return was calculated from the mean value of intensity of all cells in the interval 25-30 min, i.e., during last 5 min of PRC1 return.

Intensity profiles of opto-PRC1 removal and return (Fig. 36 B,D) were obtained on sum intensity projections of all three z-planes by drawing a pole-to-pole line along the long axis of the spindle by using Line tool in Fiji. The width of the line corresponded to the width of each individual spindle. Intensities were normalized to position of the poles.

For quantification of PRC1 knock-down by siRNA and intensity level of opto-PRC1 (in Fig. 35 A,B) PRC1 intensity on fixed cells was measured on a sum-intensity projection of five focal planes by the procedure described above, in a way that mean spindle intensity was background corrected by subtracting mean intensity in the cytoplasm. For measuring opto-PRC1 intensity on the spindle cells where PRC1 was visible on astral microtubules were not analyzed, nor imaged in live experiments.

FRAP was measured in a 5x5 pixel region of interest (ROI) positioned on PRC1-labeled bundles for each timepoint. Raw intensities were background-corrected, normalized, and fitted using $A\ (1 - e - \tau\ t)$ equation. Half-time was aquired as $\ln 0.5/-\tau$.

Inter-kinetochore distance was measured using *Line tool* in Fiji on individual or maximum intensity z-projections of up to two z-planes as a distance between centers of sister kinetochore signals. Peripheral kinetochores were defined as three outermost pairs on each side of the spindle with respect to spindle long axis, while the remaining were considered as central. Measurement of inter-kinetochore distances in prometaphase was performed on U2OS cells expressing CENP-A-GFP, mCherry-α-tubulin and PA-GFP-tubulin, just after nuclear envelope breakdown in one imaging plane where both sister kinetochores could be clearly distinguished. For measuring kinetochore alignment and orientation, as well as orientation and length of PRC1 bundles, Multipoint tool in Fiji was used. A point was placed in the center of signal of each sister kinetochore or edges of PRC1 signal for each bundle. Before measuring, images were rotated in order to achieve perpendicular direction of the equatorial plane with respect to x-axis. The equatorial plane was defined with two points placed between outermost pairs of kinetochores on the opposite sides of the spindle. For all measurements regarding kinetochores, those located at the spindle poles were not taken into

account. All measurements in opto and control cells were performed in three time-points: before the blue light was switched on, after 20 min of continuous exposure to the blue light, and 10 min after the blue light was turned off. In untreated and PRC1 siRNA treated cells measurements were performed at the beginning of imaging. Kymographs of kinetochore oscillations were produced by Low Light Tracking Tool (LLTT) pluggin in Fiji. Tracking of kinetochores in x, y plane was performed on maximum intensity of 2-3 z-planes. Sigma value (standard deviation of the Gaussian used to approximate the Point Spread Function (PSF) of the tracked objects) was set to *Automatic.*

EB3 spots in U2OS cells stably expressing 2x-GFP-EB3 and mCherry-CENP-A were tracked by obtaining their xy coordinates using Multipoint tool in Fiji from the frame when a spot appeared until it disappeared or was no longer clearly distinguishable from its neighbors. Only spots belonging to bridging fibers were traced, which were defined as those passing between sister kinetochores or moving along PRC1 streaks. Half-overlap length was measured as the distance between the last location where a tracked EB3 spot was visible and the spindle equator. The number of spots in time was obtained by visually inspecting time frames where individual kinetochore pair or PRC1 bundle was visible, and dividing the total number of the observed EB3 spots in the bridging fibers by the total time of observation of individual kinetochore pairs or PRC1 bundles. Kymographs were generated using KymographBuilder plug-in in Fiji, and half-overlap length was measured from kymographs as the distance between a spot's trajectory end point and the mid-line between the poles corresponding to the equatorial plane. These measurements were performed in the first 2 min of a fast imaging sequence, which followed after the 10 min imaging protocol required for PRC1 removal.

The GFP-tubulin signal intensity of a cross-section of a bridging fiber was measured by drawing a 3-pixel-thick line between and perpendicular to the tubulin signal joining the tips of sister k-fibers. The intensity profile was taken along this line and the mean value of the background signal present in the cytoplasm was subtracted from it. The signal intensity of the bridging fiber was calculated as the area under the peak using SciDavis (Free Software Foundation Inc., Boston, MA, USA). The signal intensity in the region lateral from k-fiber tip was measured in a similar manner, 1 μm away from a k-fiber tip, perpendicular to and crossing the corresponding k-fiber. All of the measurements were performed on a single z-plane. The profile intensity of bridging fiber and at the position lateral from k-fiber tip in SiR-tubulin (Fig. 44 B,C) was performed in the same manner. Note that mostly outermost fibers

were used for these measurements because of being most easily distinguished from neighboring fibers.

Shapes of the spindle were quantified by tracking outermost k-fiber contours in the central z-slice of the spindle, or maximum intensity z-projection of two central z-slices. All spindles were rotated to have horizontal long axis. Pole-to-k-fiber-tip tracking was done using Multipoint tool by placing 5 roughly equidistant points along contour length, first point being at the pole and the last point being at the k-fiber tip. First point of each contour was translated to (0,0). This was done for maximum of 4 trackable outermost k-fibers in the spindle. Curvature of the contour was calculated by fitting a circle to the contour points of individual k-fibers and retrieving reciprocal value of its radius. To test the effect of tracking errors on curvature, we introduced 1-pixel noise to the x and y values of tracked points, which did not change the result. Angle between outermost k-fibers (θ) was calculated as the angle between lines passing through last two points along the contour of sister k-fibers.

Spindle length and width were measured using Line tool in Fiji. For length measurements, a line was drawn from pole to pole. The position of the pole was defined as the location of the strongest tubulin signal. Width was measured by drawing a line between outermost kinetochore pairs on the opposite sides of the spindle, perpendicular to the spindle long axis.

The intensity of GFP-Kif4A in metaphase and anaphase was measured in GFP-Kif4A channel on sum-intensity projections of all three z-planes using Poligon selection tool in Fiji by encompassing chromosomes in SiR-DNA channel. The intensity of opto-PRC1 in metaphase was measured by encompassing the spindle area. Background cytoplasm intensities in both GFP-Kif4A and opto-PRC1 channels were measured in 30 x 30 pixels rectangle and subtracted from measured mean intensities of GFP-Kif4A and opto-PRC1. Corrected intensities were divided by the number of focal planes. Measurements were performed in three time-points in metaphase: before the blue light was switched on, after 20 min of continuous exposure to the blue light, and 10 min after the blue light was turned off. In anaphase, measurements were performed 4 min after anaphase onset. Anaphase onset was defined as the timeframe when separation of majority of sister chromatids in SiR-DNA channel occurred.

The mean signal intensities of opto-PRC1 and MKLP1-GFP were measured on the central z-plane using Poligon selection tool in Fiji by encompassing the spindle area in SiR-tubulin channel. Background cytoplasm intensities in both channels were measured in 30 x 30

pixels rectangle and subtracted from measured mean intensities of opto-PRC1and MKLP1-GFP. Measurements were performed in the same time-points as for Kif4A in metaphase.

For quantification of PRC1 knock-down by siRNA in HeLa BAC MKLP1-GFP cell line, PRC1 intensity was quantified in the same manner as in U2OS cells. The intensity levels of MKLP1-GFP and Kif4A-GFP in fixed HeLa cells were measured by encompassing the whole cell area using Poligon selection tool in Fiji on sum intensity projections of 5 z-planes.

Localization test of GFP-Kif4A or Kif4A-GFP, MKLP1-GFP, Kif18A-GFP, EGFP-CLASP1, and CENP-E-GFP in the bridging fibers of either opto cells or cells treated with mock siRNA or PRC1 siRNA was performed by visually inspecting the GFP signal through the z-stack, in the region where PRC1-labeled fibers were found, i.e., in the region that spans between sister kinetochores and continues ~2 μm laterally from sister kinetochores. Quantification of the signal length of PRC1-GFP in mock, Kif4A, and Kif18A siRNA treated HeLa cells was performed by drawing a 5-pixel-thick pole-to-pole line along individual bundles and calculated as the width of the peak of the PRC1-GFP signal intensity.

Statistical analysis was performed in MATLAB (MathWorks, Natick, MA, USA) and RStudio (R Foundation for Statistical Computing, Vienna, Austria). Normality of the data was inspected by Q-Q plots and Shapiro-Wilk test of normality. Normally distributed data were tested with two-tailed t-test, while Mann-Whitney test was used for non-normally distributed data, as noted in figure captions. Proportions were statistically compared with test for equality of proportions, two-proportions z-test. For data with expected count smaller than 5, Yates's correction for continuity was used.

Graphs were generated in MATLAB (MathWorks) and RStudio (R Foundation for Statistical Computing). ImageJ (National Institutes of Health, Bethesda, MD, USA) was used to crop and rotate images, and to adjust brightness and contrast to the entire image, which was applied equally to all images in the same panel. To remove high frequency noise in displayed images a Gaussian blur filter with a 0.5-pixel sigma (radius) was applied where stated. Figures were assembled in Adobe Illustrator CS5 (Adobe Systems, Mountain View, CA, USA).

4. RESULTS AND DISCUSSION

4.1 Kif18A strongly affects kinetochore oscillations in RPE-1 cells

During metaphase kinetochores are aligned at the spindle equator, but exhibit constant poleward (P) and away-from the pole (AP) movements in a region around spindle equator (Skibbens et al., 1993). For such movements to occur, kinetochores need to be influenced by forces. Since kinetochores are attached to plus-ends of k-fiber microtubules, their movement depends on the dynamics of k-fibers. Shrinking microtubules were shown to be able to pull on kinetochores (Grishchuk et al., 2005), while growing ones can exert pushing forces on obstacles against which they are growing (Dogterom and Yurke, 1997). Many *in vitro* and *in vivo* studies identified kinesin-8 motor as a main regulator of microtubule dynamics, since it was shown to accumulate at microtubule plus-ends in a length-dependent manner, where it promotes microtubule catastrophe and shrinking (Erent et al., 2012; Grissom et al., 2009; Gupta et al., 2006; Mayr et al., 2007; Tischer et al., 2009; Varga et al., 2006; Varga et al., 2009). Also, it was shown to influence kinetochore movements in fission yeast (Garcia et al., 2002; Klemm et al., 2018; West et al., 2002) and human cells (Gardner et al., 2008; Mayr et al., 2007; Stumpff et al., 2008; Stumpff et al., 2012). However, how kinesin-8 motors contribute to force generation at kinetochores remained elusive.

To explore the effects of Kif18A on chromosome alignment and force generation at kinetochores in human cells, human retinal pigmented epithelium (RPE-1) cells stably expressing CenpA-GFP and centrin-GFP were either depleted for Kif18A by siRNA or transfected with Kif18A untagged construct to elevate the amount of Kif18A. To assess the role of Kif18A in kinetochore oscillations, cells were analyzed by fluorescence time-lapse microscopy. In control cells kinetochores oscillated by exhibiting coordinated poleward (P) and away from the pole (AP) movements mainly restricted to the narrow region around the spindle equator (**Fig. 24**). Oscillatory movements were drastically increased in cells depleted for Kif18A and supressed in cells with elevated Kif18A expression level, which is observable both from traces of movement of individual kinetochore pairs with respect to the equatorial plate and kymographs generated from CenpA fluorescence, consistent with previous reports of influence of changed levels of Kif18A on kinetochore behavior in human cells (Stumpff et al., 2008; Stumpff et al., 2012) (**Fig. 24 B,C**).
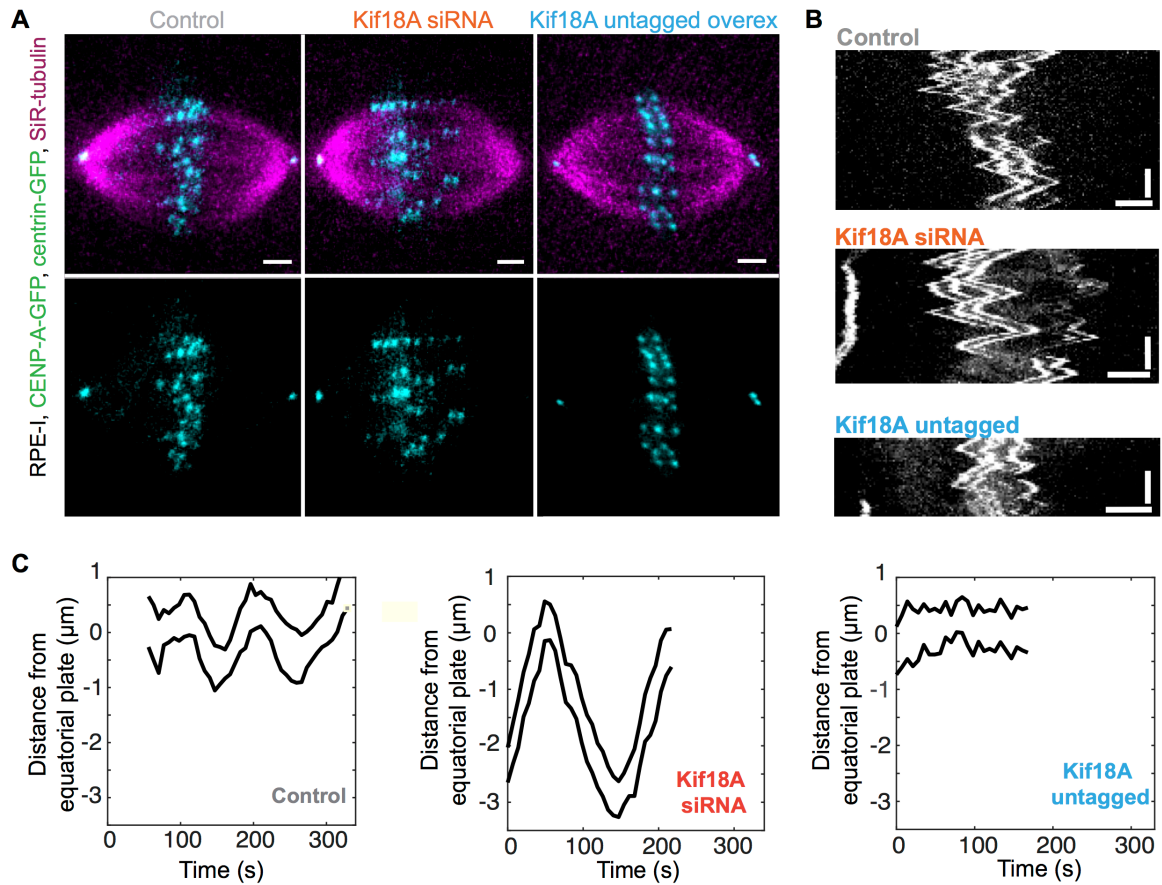
Figure 24. Alterations in Kif18A levels affect the extent of kinetochore oscillations. A. Still images of metaphase spindles in RPE-1 cells stably expressing CENP-A-GFP and centrin-GFP (cyan) with microtubules stained with 50 nM SiR-tubulin dye (magenta) in control (left), Kif18A siRNA treated (middle) and Kif18A-untagged transfected (right) cells. Top:merge, bottom:GFP only. **B**. Representative kymographs of CENP-A-GFP fluorescence (gray) (right) in control (top), Kif18A siRNA treated (middle) and Kif18A-untagged transfected (bottom) cell. **C.** Representative distance versus time plots of individual kinetochore pairs in control (left), Kif18A siRNA treated (middle) and Kif18A-untagged transfected (right) cell. Thick black lines, kinetochore trajectories. Position 0 µm indicates equatorial plate. Horizontal scale bars, 2 µm; vertical scale bar, 2 min.

To explore the effects of Kif18A on kinetochore movements and positioning in more detail in these three groups of cells, positions of poles and kinetochores were tracked in time to obtain their x, y coordinates from which several parameters were calculated for each pair (scheme in **Fig. 25 A**). The most striking effect of alteration of Kif18A levels was on positioning of kinetochore pairs with respect to the equatorial plate (EQ) (**Fig. 25 A**). Depletion of Kif18A increased the mean distance of each kinetochore pair from the equatorial plate (dEQ) from 0.7 ± 0.3 µm (n=79 pairs, N=15 cells) in control cells to 1.2 ± 0.8 µm (n=80 pairs, N=14 cells) in

Kif18 siRNA treated cells (p-value: $3*10^{-7}$), whereas elevated level of Kif18A decreased dEQ to 0.4 ± 0.3 µm (n=64 pairs, N=13 cells, p-value: $9.8*10^{-7}$) (**Fig. 25 B**). Similar extent of dEQ changes upon altered Kif18A levels is also obtained if every data point (each tracked time-frame) was taken into account (**Fig. 25 C**). Note the more frequent occurrence of dEQ above 2 µm in Kif18A siRNA treated cells and the tendency toward lower values in cells with elevated Kif18A levels compared to control (**Fig. 25 B,C**). These data indicate that Kif18A dampens oscillations by limiting the extent of bi-oriented kinetochore movements in a narrow region closer to the equatorial plate, in agreement with (Stumpff et al., 2008).

Alterations of Kif18A levels also affected interkinetochore tension reflected as changes in interkinetochore distance (dKC) (**Fig. 25 A**). Depletion of Kif18A caused a mild decrease of mean interkinetochore distance of each pair from 0.89 ± 0.01 µm in control cells (n=79 pairs from 15 cells) to 0.82 ± 0.01 µm in Kif18A siRNA treated cells (n=80 pairs from 14 cells) (p-value: 4.65*10-4), compared to the distance between kinetochores prior to attachment to microtubules in prometaphase (0.60 ± 0.01 µm; n=75; N=6). In contrast, elevated levels of Kif18A increased the stretch between sister kinetochores to 1.05 ± 0.02 µm (n= 64 pairs, N=13 cells, p-value: $1.55*10^{-9}$) (**Fig. 25 D**). Similar extent of changes in interkinetochore distance upon altered Kif18A levels is also obtained if every data point (each tracked time-frame) was taken into account (**Fig. 25 D**). These results indicate Kif18A is involved in regulation of tension between sister kinetochores. Measured effects of altered Kif18A levels on the extent of kinetochore oscillations and inter-kinetochore tension in RPE-1 cells are consistent with similar experiments in HeLa cell line, where depletion elevated oscillations, while overexpression of Kif18A dampened oscillation movements (Mayr et al., 2007; Stumpff et al., 2008). However, in contrast to these studies, where modulation of Kif18A levels changed spindle length, in RPE-1 cells these alterations did not affect spindle length significantly, indicating this effect could be cell type dependent (**Fig. 25 E**).

To investigate the influence of Kif18A on kinetochore orientation within the spindle, an angle between sister kinetochore axis and a line perpendicular to equatorial plate was measured (α_{KC}) (**Fig. 25 A**). Alterations of Kif18A expression levels did not affect α_{KC} significantly as can be seen from distribution histograms for mean values of each tracked kinetochore pair ($8.6 \pm 0.4°$ in control cells, n=79 pairs, N=15 cells ; $9.6 \pm 0.5°$ in Kif18 siRNA treated cells, n=80 pairs, N=14 cells; $8.2 \pm 0.8°$ in cells expressing untagged Kif18A, n=64 pairs, N=13 cells) (**Fig. 26 A**). The distributions of α_{KC} for each data point were similar to those obtained for mean values of each kinetochore pair in all treatments (**Fig. 26 B**). These results together with the mild decrease in interkinetochore distance upon Kif18A depletion are

in line with the notion that human kinesin-8 Kif18A does not control establishment and maintenance of kinetochore-microtubule attachments in contrast to *Drosophila* kinesin-8 Klp67A, as kinetochore dettachments would result in more frequent 'flipping' events of kinetochore pairs and more dynamic changes in αKC (Edzuka and Goshima, 2019).
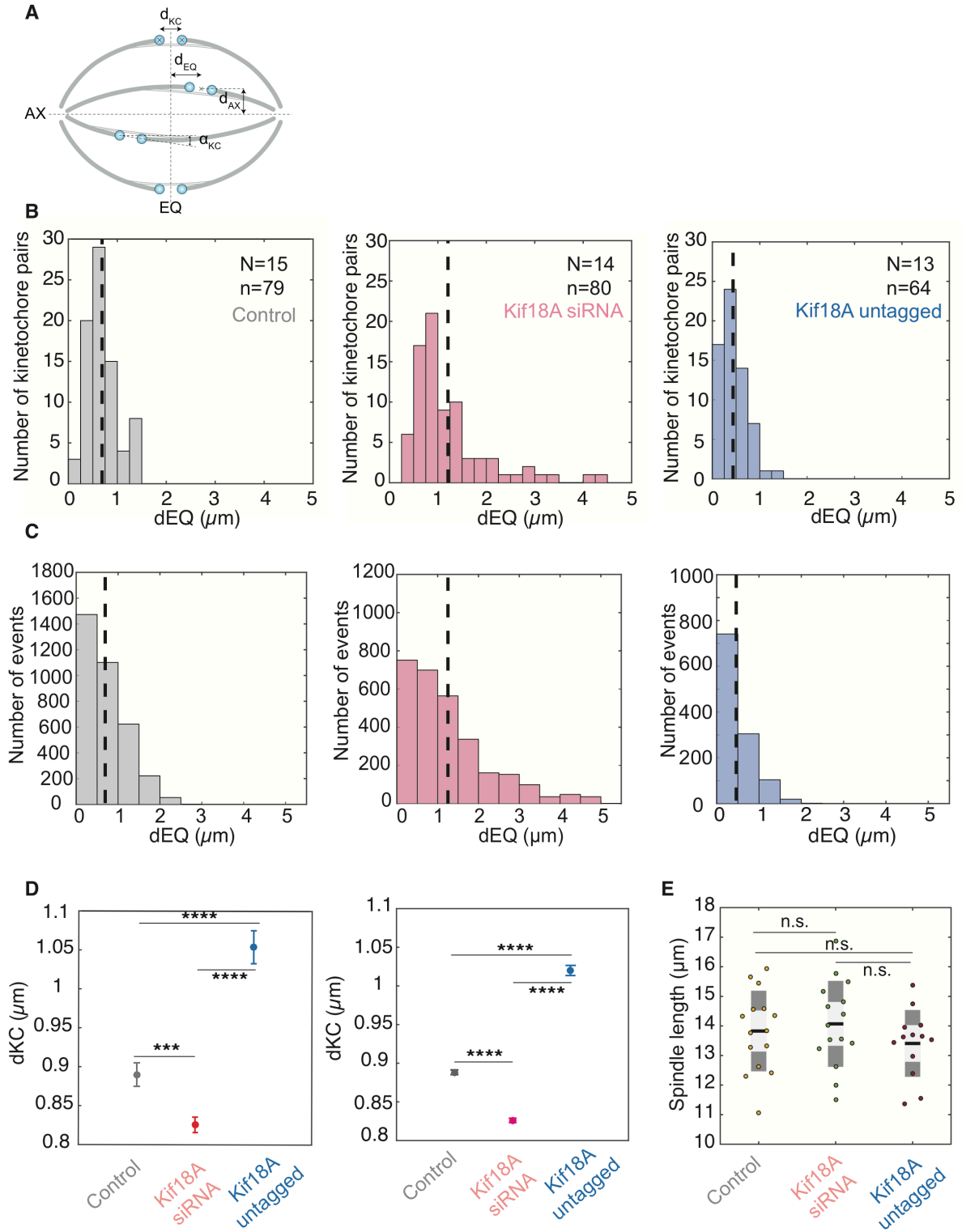
Figure 25. Kif18A regulates the extent of kinetochore movements around equator and affects inter-kinetochore tension. A. Scheme of measured parameters. dEQ, distance of sister kinetochore midpoint from equatorial plate (EQ); dAX, distance of sister kinetochore midpoint from the long spindle axis (AX); dKC, interkinetochore distance or distance between sister kinetochores and α_{KC}, the angle between sister kinetochore pair axis and a line perpendicular on the equatorial plate. **B.** Histograms of mean dEQ values for each kinetochore pair in control (left), Kif18A siRNA treated

(middle) and cells expressing untagged Kif18A (right;). Bin width is set to 0.25 μm. **C.** Histograms of dEQ values for each measured time point for cells as in B. Bin width is set to 0.5 μm. **D.** Measurements of dKC per kinetochore pair (left) and for every time point (right) in cells as in B **E.** Measurements of spindle length (univariate scatter plots) for cells as in B. Boxes represent standard deviation (dark gray), 95% standard error of the mean (light gray) and mean value (black). Thick dashed black lines on histograms indicate mean values. N, number of cells; n, number of kinetochore pairs. Statistical analysis; t-test. p-value legend: < 0.0001 (****), 0.0001 to 0.001 (***), 0.001 to 0.01 (**), 0.01 to 0.05 (*), ≥ 0.05 (ns).
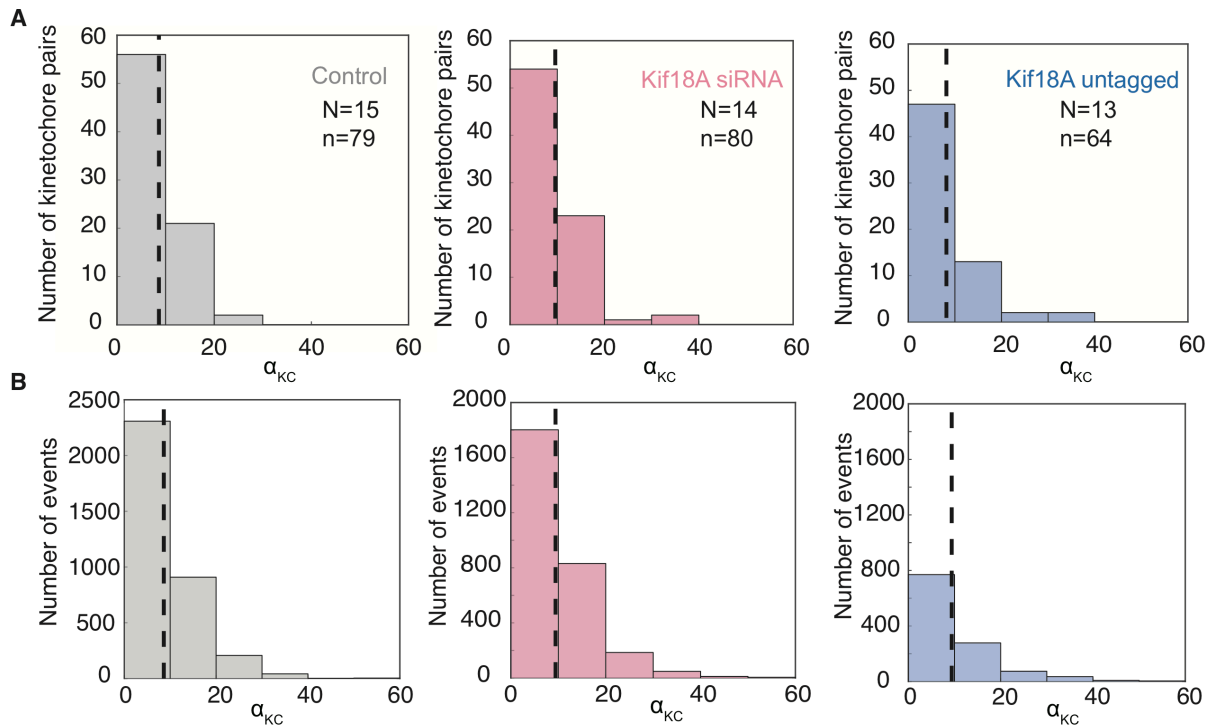
Figure 26. Changes in Kif18A expression levels does not affect sister kinetochore pair orientation. **A.** Histograms of mean α_{KC} of individual kinetochore pairs in control (left), Kif18A siRNA treated (middle) and cells expressing untagged Kif18A (right;). **B.** Histograms of α_{KC} for values of each measured time frame. Bin widths are set to $10^{°}$. Thick dashed black lines on histograms indicate mean values. N, number of cells; n, number of kinetochore pairs.

Corellations of measured parameters revealed mild positive correlation of α_{KC} versus corresponding dEQ in control cells meaning that those kinetochores whose mean position was more distant from equatorial plate had more tilted inter-sister axis. Also, in control cells and in cells expressing untagged Kif18A those kinetochore pairs with higher α_{KC} had lower interkinetochore tension. Finally, in Kif18A siRNA cells there was a negative correlation of

dEQ and corresponding distance from the long spindle axis, dAX, suggesting that displaced kinetochore pairs were preferentially localized in the central part of the spindle, closer to the long spindle axis (**Fig. 27**).
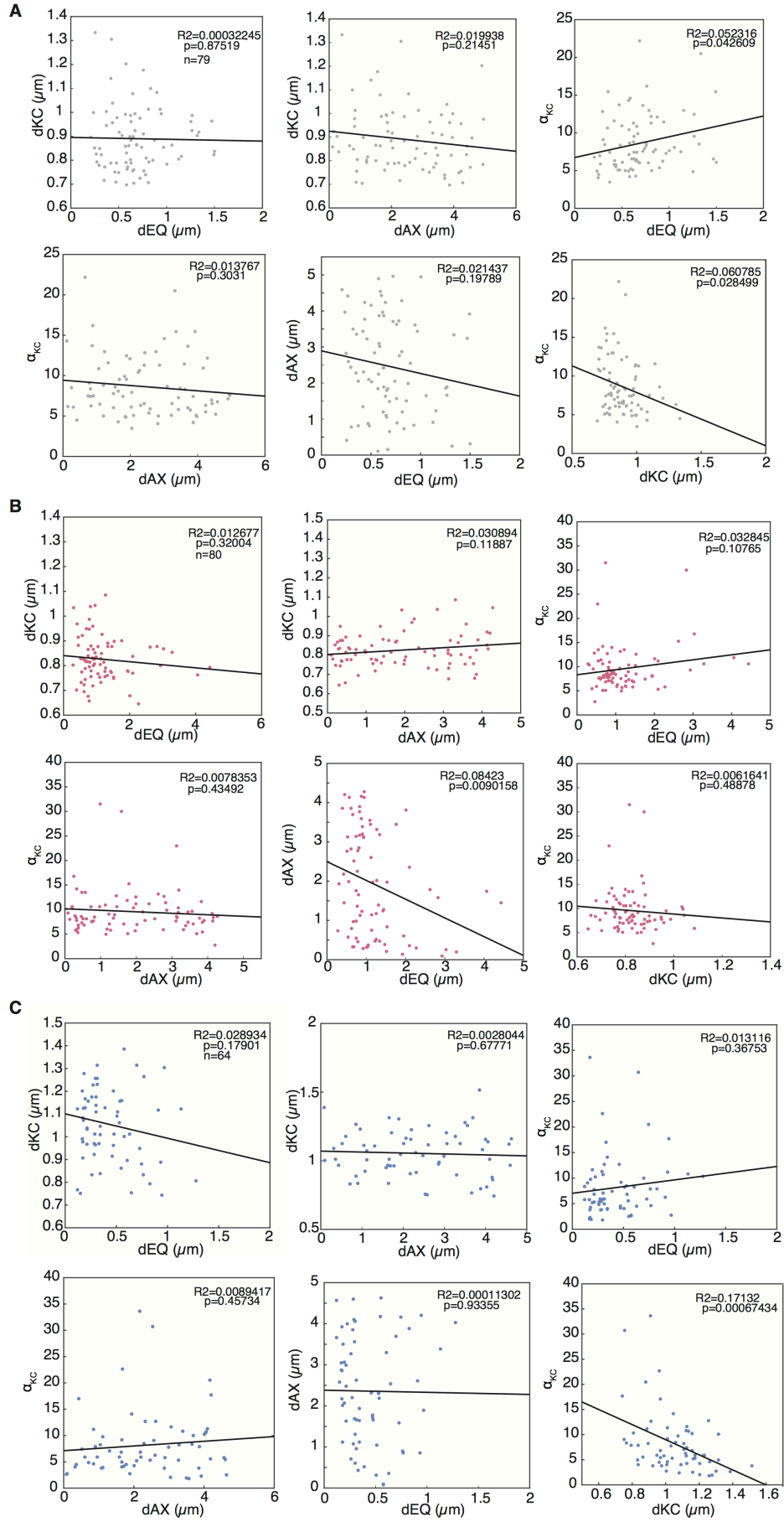
Figure 27. A. Plots of mean values for each kinetochore pair of: dKC verus corresponding dEQ, dKC versus corresponding dAX, α_{KC} versus corresonding dEQ, α_{KC} versus corresonding dAX, dAX versus corresponding dEQ and α_{KC} versus corresonding dKC for in control cells. **B.** Plots as in A for Kif18 siRNA treated cells. **C.** Plots as in A for cells expressing untagged Kif18A. Black lines show linear regression; R^2, coefficient of determination.

4.2 Kif18A regulates movements of both inner and outer kinetochore pairs

Although kinetochore oscillations are a general feature of metaphase, not all kinetochores within the spindle behave equally in this sense. Differences in the extent of kinetochore movements were observed to depend on the location within the spindle in PtK$_1$ cells, with those on the outer parts of the spindle, at a larger distance from the long spindle axis, oscillating to a less extent compared to those in the inner parts of the spindle (Canman et al., 2002; Cimini et al., 2004). Such behavior in PtK$_1$ cells was explained by the model in which large, acrocentric chromosomes that localize preferentially on the periphery of the spindle are subjected to a larger PEF that limits their movements (Civelekoglu-Scholey et al., 2013). Such position-dependent differences in kinetochore behavior were also reported for human HeLa cells (Stumpff et al., 2008). In the same study Kif18A was observed to accumulate more on plus-ends of k-fibers at the spindle periphery compared to those closer to the spindle centre, which can be attributed to differences in the length of k-fibers, where those at the spindle periphery are longer and therefore accumulate more Kif18A that restricts movements of the respective kinetochore pairs more strongly compared to those positioned closer the the long spindle axis.

Inspired by the same idea, this was also tested in RPE-1 cells with different levels of Kif18A. In control cells, the mean dEQ values for individual kinetochore pairs were greater for pairs localized closer to the long spindle axis (dAX $\leq$ 2 µm) than those at the spindle periphery (dAX > 2 µm), indicative of outer pairs oscillating to a less extent compared to the inner ones (**Fig. 28**). Depletion of Kif18A by siRNA increased mean dEQ of both inner and outer kinetochore pairs, implying that oscillations of both groups of kinetochore pairs are regulated by Kif18A (**Fig. 28**). In cells expressing untagged Kif18A dEQ of inner and outer pairs was not significantly different (**Fig. 28**). These data show that Kif18A restricts movements of both central kinetochore pairs and those at the periphery of the spindle (Stumpff et al., 2008).
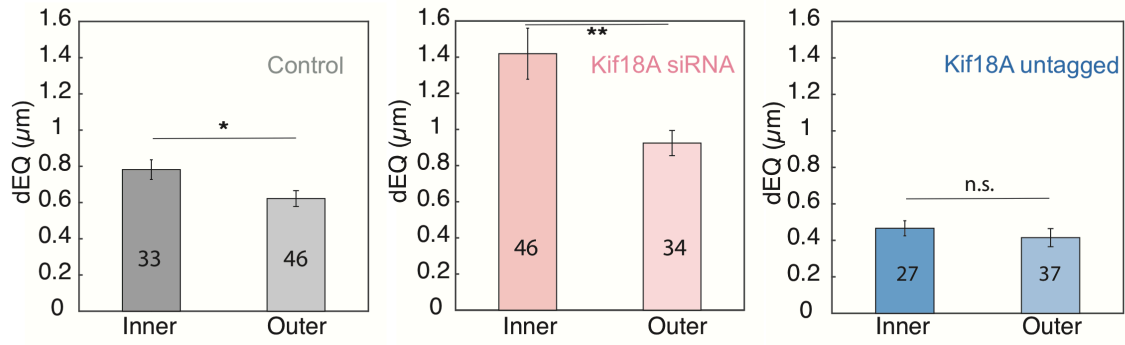
Figure 28. Mean dEQ values for inner kinetochore pairs, closer to the long spindle axis (dAX ≤2 μm) and outer pairs, positioned at the spindle periphery (dAX >2 μm) in control (left), Kif18 siRNA treated (middle) and untagged Kif18A transfected (right;) cells. Numbers in bars; kinetochore pairs. Statistical analysis; t-test. P-value legend as in Fig. 25.

4.3 Kif18A regulates kinetochore oscillation velocity and switch rates

The stronger kinetochore oscillations upon Kif18A depletion can occur due to changes in two important parameters of kinetochore movement: kinetochore velocity and rate of directional switches. Previous study reported Kif18A depletion decreases kinetochore switching rate (Stumpff et al., 2008), while reports on its influence on kinetochore velocity were somewhat conflicting (Mayr et al., 2007; Stumpff et al., 2008).

These parameters were also measured in RPE-1 cells to elucidate how Kif18A depletion leads to elevated extent of kinetochore movements. The velocity was calculated as a ratio of the traveled distance over time between two directional switches, while the rate of directional switches was calculated by counting the number of times kinetochore pairs switched direction divided by the duration of the imaging to obtain number of switches per minute (see scheme in **Fig. 29**). Depletion of Kif18A by siRNA increased the velocity of kinetochore movements from 1.61 ± 0.07 μm/min in control cells to 2.16 ± 0.08 μm/min in siRNA treated cells (control: 47 measurements from 13 pairs in 11 cells; Kif18 siRNA: 54 measurements from 14 pairs in 7 cells; p-value $3.5 *10^{-6}$) (**Fig. 29**). Also, kinetochore swich rates decreased from 1.06 ± 0.04 min^{-1} to 0.85 ± 0.05 min^{-1} upon treatment with Kif18A siRNA (control: 279 switches from 52 pairs in 15 cells; Kif18 siRNA: 243 switches from 67 pairs in 13 cells; p-value=0.002) (**Fig. 29**). Note that measurements of kinetochore velocity and switching rates could not be performed in cells expressing untagged Kif18A due to dampened kinetochore oscillations.

These results suggest that in Kif18A depleted RPE-1 cells higher velocity of kinetochore movements together with decrease in kinetochore swiching rates lead to increase in the extent of kinetochore movements, a mechanism consistent with the one reported in HeLa cells (Stumpff et al., 2008).
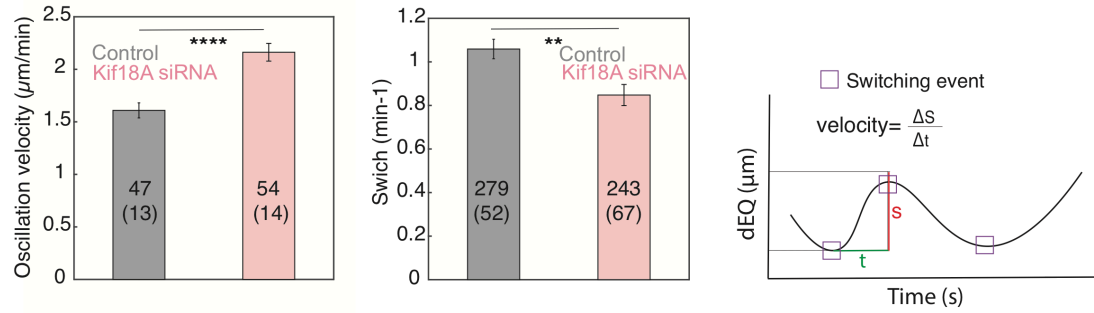
Figure 29. Kif18A affects kinetochore oscillations by regulating velocity of kinetochore movements and the rate of directional switches. Velocity of kinetochore movements (left) in control and Kif18 siRNA treated cells. Rate of directional switches (middle) in control and Kif18 siRNA treated cells. Scheme of measurements of kinetochore velocity and definition of directional switches (right) from time plots of sister pair midpoint distance from the equatorial plate (dEQ). Numbers in bars; switches and kinetochore pairs. Statistical analysis; t-test. P-value legend as in Fig. 25.

4.4 Laser ablation assay for studying the role of Kif18A in force generation at kinetochores

During oscillations, kinetochore movements could be generated by pulling or pushing force exerted by shrinking or leading k-fiber and growing or trailing k-fiber, respectively. To explore the forces acting on the kinetochores during metaphase, force balance was changed by laser ablation experiments of k-fibers in RPE-1 cells, similar to our previous experiments (Buda et al., 2017; Kajtez et al., 2016; Milas and Tolić, 2016; Vukusic et al., 2017). Experiments were divided in three groups: cutting of k-fibers in front of the leading kinetochore, which moves towards the pole it is attached; behind trailing kinetochore or the one that is moving away from its respective pole; and cutting of k-fibers of kinetochores that were in the pausing state in the moment of cutting (Fig. 30). The behavior of kinetochore pairs after laser cutting, in the terms of the direction of their movement, should give an insight in the forces that drive their movements. Furthermore, comparison of kinetochore behaviour

after laser cutting in cells with altered levels of Kif18A should reveal the role of Kif18A in force generation at kinetochores.
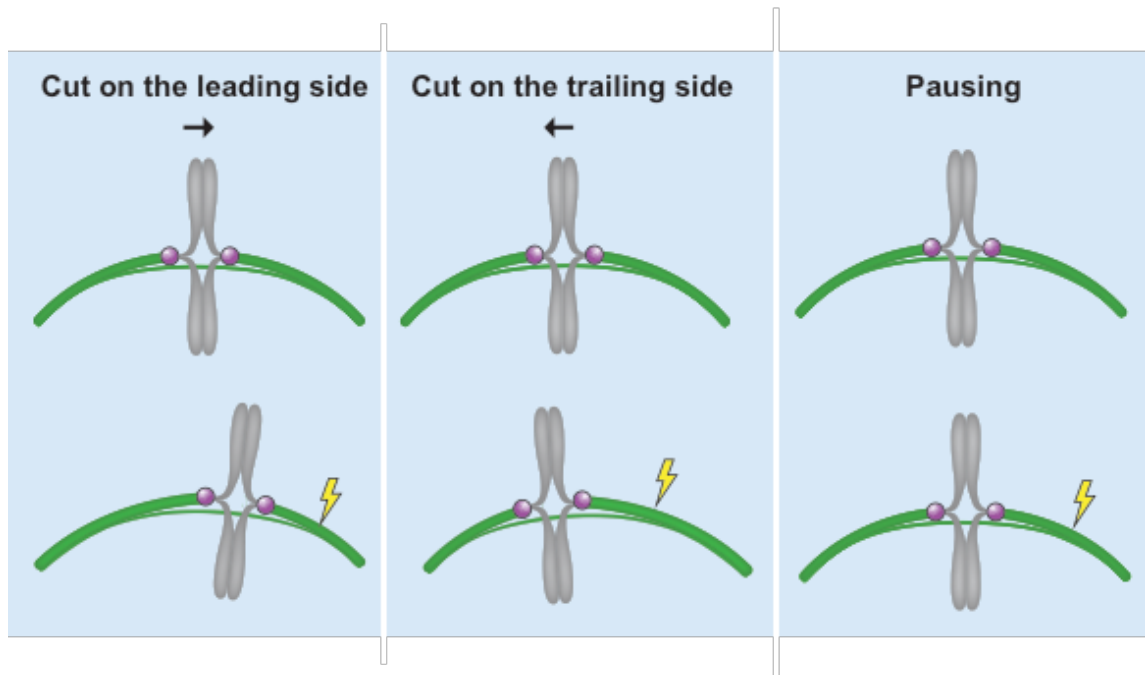
Figure 30. Scheme of laser ablation assay of k-fibers for studying the forces that drive kinetochore movements. A. Cutting of k-fiber on the leading side, in front of the kinetochore that moves towards its pole. **B**. Cutting of k-fiber on the trailing side, behind the kinetochore that moves away from its respective pole. **C.** Cutting of k-fiber for kinetochore pairs in the pausing state of movement. Black arrows denote the direction of kinetochore pair movement. Laser cutting is indicated with the yellow lightning bolt.

4.5 Chromosome movements along the spindle are caused by pulling forces

Laser cutting experiments were performed on the outermost k-fibers, since they could be more easily distinguished from their neighbours compared to those positioned in the inner parts of the spindle. The reincorporation of k-fibers after they were severed by ablation back to the spindle was observed previously (Chen and Zhang, 2004; Elting et al., 2014; Maiato et al., 2004a; Snyder et al., 1991), and higher microtubule density in the inner parts of the spindle could facilitate this process, which was shown to be mediated by NuMa and dinein/dynactin enrichment at newly produced minus ends that reanchor severed bundle back into the spindle (Elting et al, 2014).

Cuts were performed at a mean distance of 1.32 ± 0.06 μm from kinetochore, measured as a length of resulting k-fiber stub in SiR-tubulin one time-frame after ablation.

Successful ablation was defined as a gap in SiR-tubulin signal at the place of the cut, outer movement of ablated element away from the spindle axis accompanied with a decrease in interkinetochore distance (**Fig. 31 A**) (Buda et al., 2017; Kajtez et al., 2016; Milas and Tolić, 2016; Vukusic et al., 2017). In many cases, the ablated pair did not move outwards, but since other two criteria were satisfied, it was considered as a successful cut and analysed until the interkinetochore distance restored, indicative of a structural reintegration of severed k-fiber back into the spindle, probably through NuMa and dynein/dynactin recruitment on newly formed minus ends (Elting et al., 2014).

In the moment of the cut, ablated kinetochore pairs were observed to persist in three possible states regarding their movement, so ablations were divided in three groups: cuts on the leading side, cuts on the trailing side and the so called pausing referring to pairs that did not exhibit any directional movement in the moment of the cut. These three groups were observed in cutting experiments in both control and Kif18A siRNA treated cells, whereas in cells with elevated levels of Kif18A all ablated pairs were in undetermined state of movement since oscillations in these cells were greatly suppressed (Fig 31 B-D). Therefore, results regarding kinetochore behaviour after cuts on the leading and trailing side could be obtained only in control and Kif18A siRNA treated cells.

In all cells laser cutting resulted in poleward movement of ablated kinetochore pairs regardless of their state of movement before cutting, as can be observed on representative plots of kinetochore-to-unablated-pole distances of individual kinetochore pairs (**Fig 31 B-D,** see **Fig. 32** for all cells). In the case of cuts on the leading side, initially poleward moving pair switched its direction of motion towards the pole on the unablated side of the spindle. Interestingly, in both control and Kif18A siRNA treated cells, there was a pause before kinetochore pair switched to poleward movement. However, in control cells it lasted for about one time frame (4.7 ± 1.5 s), whereas in Kif18 siRNA this delay was longer (26 ± 9 s). Kinetochore pairs for which the cuts were performed behind their trailing kinetochores maintained their initial continuous movement towards pole on unablated side of the spindle. These results suggest that kinetochores are moved by pulling forces in both control and Kif18A siRNA treated cells, with Kif18A affecting the timing of directional switch of poleward moving kinetochore pair after cut on the leading side.
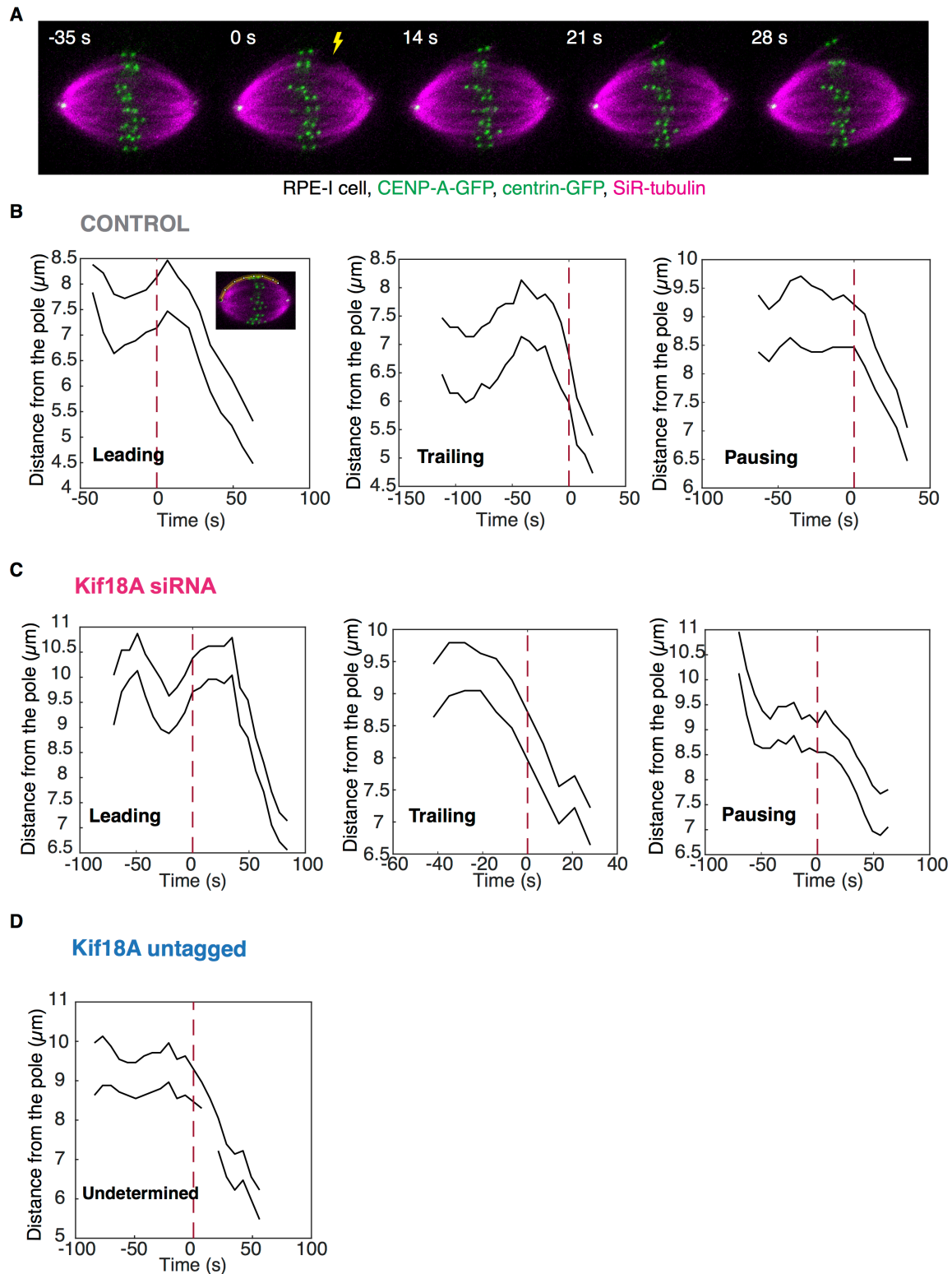
Figure 31. Laser cutting of outer k-fibers in RPE-1 cells induces poleward kinetochore movement. A. Time-lapse of laser ablation of outermost k-fiber in control metaphase RPE-1 cell stably expressing CENP-A-GFP and centrin-GFP (green) and tubulin stained with SiR-tubulin dye (magenta). Time of ablation is set to 0 s. Cutting site is indicated with the yellow lightning bolt. Note the outward movement of ablated k-fiber. Images are maximun intensity projections of 5 z-planes.

Scale bar, 2 µm. **B.** Representative plots of kinetochores-to-unablated-pole distance for pairs where cuts were performed in front of the leading kinetochore (left), behind trailing kinetochore (middle) and on k-fiber of pausing (right) pair in control cells. The image in the first graph indicates how tracking of kinetochore positions was performed (see Methods). **C.** Plots as in B for Kif18A siRNA treated cells**. D.** Plots as in B for cells expressing untagged Kif18A. Note that in this group all pairs were in undetermined state in the moment of ablation due to dampened oscillations. Dashed red lines on the graphs indicate the moment of the cut that is set to correspond to 0 s. Thick black lines mark position of kinetochores.

Laser cutting caused a decrease of interkinetochore distance in control cells. As majority of the cuts were performed at the distance less than 2 µm away from kinetochore, which was shown to correspond to a hypothetical junction point where k-fibers and bridging fibers start to interact with each other, this further supports the role of bridging fibers in maintainence of tension between sister kinetochores (**Fig. 32 C**) (Kajtez et al., 2016; Milas and Tolić, 2016). Interestingly, in Kif18A depleted cells the extent of interkinetochore stretch was similar both before and after the cut implying that depletion of Kif18A possibly reduces the tension to a minimal level for bi-oriented kinetochores and severing of interaction between k-fiber and bridging fiber does not affect it further from that (**Fig. 32 C**).

Plotting of sister kinetochore midpoint distances from unablated pole revealed leading, trailing and pausing pairs in control exhibited similar velocities of poleward movement after cutting with the mean value for all ablated pairs of -2.5 ± 0.4 µm/min, calculated by fitting a line on the trajectory of each individual ablated kinetochore pair from the moment it started moving poleward after the cut. This velocity was somewhat higher than the one extracted from switches of individual kinetochore pairs (see Fig. 29) (**Fig. 33**). After depletion of Kif18A the velocity of poleward movement of those pairs that were pausing in the moment of the cut was somewhat higher compared to leading and trailing in Kif18A siRNA and control (**Fig. 33 A,B**). The overall velocity for all ablated kinetochore pairs in Kif18A siRNA treated cells was -3.4 ± 0.4 µm/min, consistent with depletion of Kif18A increasing the velocity of kinetochore movements (**Fig. 33 C**).
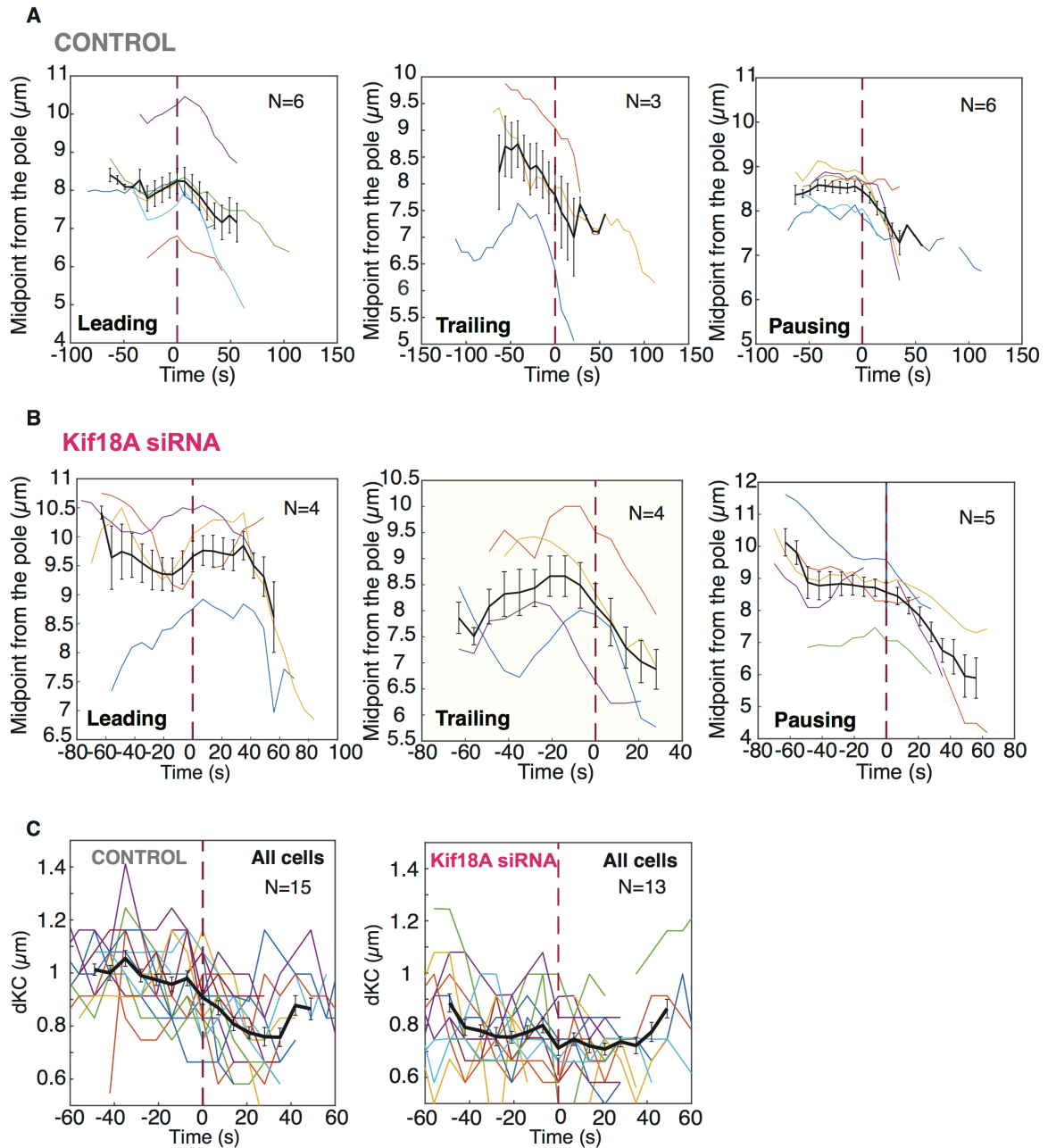
Figure 32. A. Distances of sister kinetochore pair midpoints from unablated pole after laser cutting for all leading (left), trailing (middle) and pausing (right) pairs in control cells. Note the short pause before switch to poleward movement for pairs that were cut on the leading side. **B.** Distances of sister kinetochore pair midpoints from unablated pole after laser cutting for all leading (left), trailing (middle) and pausing (right) pairs in Ki18A siRNA treated cells. Note the delay before switch to poleward movement for pairs that were cut on the leading side and compare with A. **C.** Interkinetochore distance for all ablated kinetochore pairs in control (left) and cells treated with Kif18 siRNA (right) before and after laser cutting. Dashed red lines on the graphs indicate the moment of the cut that is set to correspond to 0 s. Single colored line represent individual cell. Thick black lines, mean; errorbars, SEM.
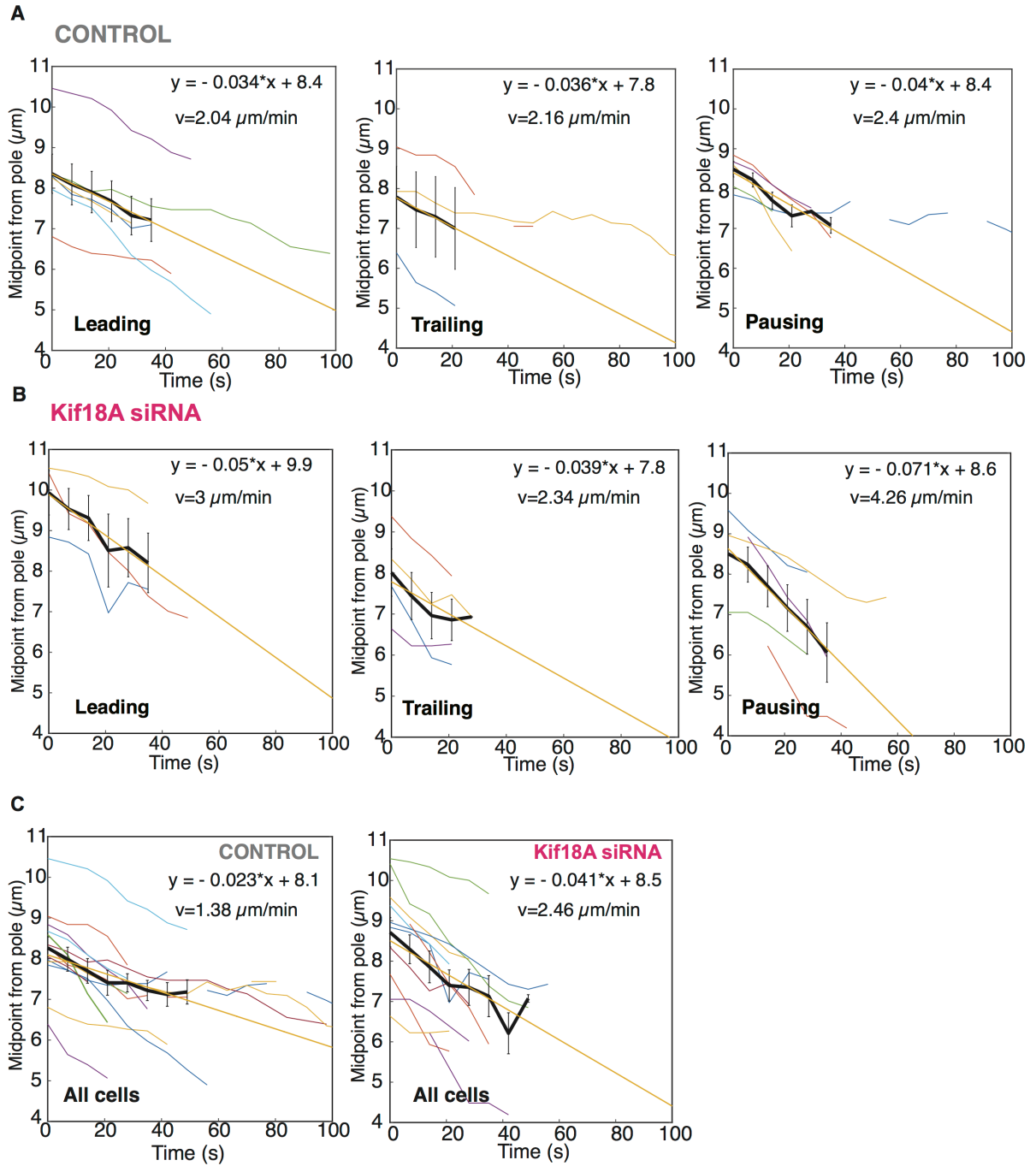
Figure 33. Velocity of poleward kinetochore movement after laser ablation. A. Plots of sister kinetochore midpoint distances from the unablated pole during poleward movement for leading (left), trailing (middle) and pausing (right) pairs after ablation in control cells. **B.** Corresponding plots as in A in Kif18A siRNA treated cells. **C.** Corresponding plots as in A for all ablated pairs in control (left) and Kif18A siRNA treated cells (right). Single colored lines correspond to individual cells. Thick black line, mean; errorbar, SEM; thick yellow line, linear regression on the average line. Equation of the regression line in the form y=ax + b is indicated in the upper left corner. Note that velocities indicated on the graphs were calculated from the slope of the average lines, while those in the main text are obtained by fitting lines on trajectories of individual kinetochore pairs.

4.6 Development of optogenetic system for fast and reversible removal of PRC1 from the spindle

As evident from previous chapters, forces produced by dynamics of k-fiber plus ends strongly influence kinetochore alignment, with kinesin-8s being the most important among regulators of k-fiber dynamics since their perturbations have the strongest individual effect on kinetochore alignment (Mayr et al., 2007; Stumpff et al., 2008). However, k-fibers were shown not to be isolated from other populations of microtubules in the spindle, but to interact with them (McDonald et al., 1992; O'Toole et al., 2020), meaning they can exert forces on k-fibers and in this way on kinetochores also. Sister k-fibers were shown to be tightly linked by the bridging fiber, a bundle of antiparallel microtubules that balances the tension on sister kinetochores, whose microtubules are crosslinked by PRC1 (Kajtez et al., 2016; Polak et al., 2017; Tolic, 2018; Vukusic et al., 2017). However, the role of forces exerted by bridging fiber in chromosome alignment at the metaphase plate is unknown.

To study the role of PRC1 and forces arising from coupling of bridging and k-fibers in chromosome alignment, an optogentic approach for fast and reversible removal of PRC1 from the spindle to the cell membrane was developed, based on the previously designed improved light inducible dimmer (iLID) system (Guntas et al., 2015). In this system, PRC1 is fused with red fluorescent protein tgRFPt and SspB protein from *E. coli*, while the iLID, which contains bacterial peptide SsrA and the light-oxygen-voltage (LOV2) domain from *Avena sativa* plant, is bound to the cell membrane by a short peptide, CAAX. Upon exposure to the blue light, LOV2 adopts a conformation that allows dimerization of SsrA and SspB upon exposure to the blue light (**Fig. 34 A**). After cessation of exposure to the blue light, LOV2 adopts its initial conformation leading to decreased affinity of SsrA to SspB. Therefore, exposure to the blue light should induce translocation of PRC1 from the central region of the metaphase spindle, from now on referred to as the spindle midzone, to the cell membrane, whereas cessation of exposure to blue light should restore PRC1 localization on the spindle (**Fig. 34 A**).

This approach was tested in human osteosarcoma U2OS cells with stable expression of kinetochore protein CENP-A-GFP. Cells were transiently transfected with PRC1-tgRFPt-SspB (henceforth opto-PRC1) and iLID-CAAX (**Fig. 34 B**). Before addition of these constructs endogenous PRC1 was depleted by 90 ± 2 % as inferred from immunofluorescence (**Fig. 35 A**). Cells transfected with both these constructs from now on will be called opto cells.
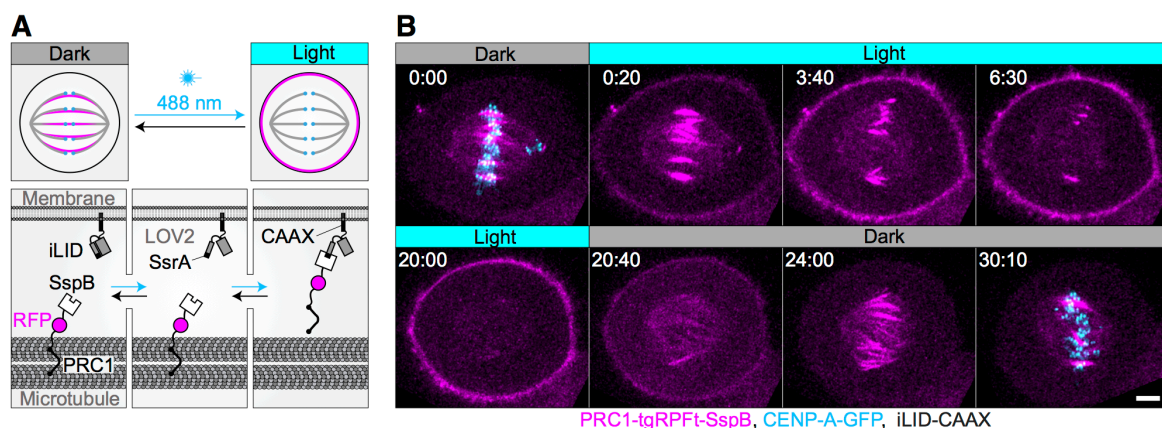
Figure 34. Optogenetic system allows for reversible removal of PRC1 from the spindle. A. PRC1 is fused with SspB and tgRFPt (opto-PRC1). iLID, composed of photosensitive LOV2 domain and SsrA is tagged with CAAX sequence which mediates its binding to the cell membrane. Exposure to the blue light induces conformational change in LOV2 domain, enabling dimerisation of SspB and SsrA, and thus translocation of PRC1 from the spindle to the cell membrane. After the blue light is turned off, LOV2 adopts its initial conformation, leading to decreased affinity of SspB for SsrA, and consequently dissociation of PRC1 from the membrane and its return to the spindle. **B.** Timelapse images of a metaphase spindle in a U2OS cell stably expressing CENP-A-GFP (cyan), depleted for endogenous PRC1, with transient expression of opto-PRC1 (magenta) and iLID-CAAX. Note that kinetochores are shown in first and last image only to point out PRC1 removal. Images are maximum intensity projections of three z-planes, smoothed with 0.1-μm-sigma Gaussian blur. Time; min:sec. Scale bar; 5 μm.

Before exposure to the blue light, opto PRC1 had normal localization on the microtubule bundles in the spindle midzone (**Fig. 34 B**; 0:00 min), with the length of PRC1 streaks 3.77 ± 0.08 μm (n=193 bundles, N=30 cells), consistent with that of endogenous and fluorescently labelled PRC1 in metaphase (Kajtez et al., 2016; Polak et al., 2017), though the total signal intensity of opto-PRC1 on the spindle was higher compared to endogenous PRC1 (**Fig. 35 B**). Addition of opto-PRC1 did not change duration of metaphase as inferred from the fraction of cells that entered anaphase during image acquisition, which was similar in cells with endogenous PRC1 and cells treated with PRC1 siRNA containing opto-PRC1 (79 ± 6 % N=37, and 71 ± 5 % N=72, respectively, p=0.4, Pearson's Chi-squared test) (**Fig. 35 C**). After exposure to the blue light, opto cells were able to progress to cytokinesis (**Fig. 35 D**). Taken together, these data suggest that opto-PRC1 replaces the depleted endogenous PRC1.

Upon exposure to the blue light, opto-PRC1 signal on the spindle decreased and its signal on the membrane increased (**Fig. 34 B**; 0:20-20:00 min). After the blue light was switched off, opto-PRC1 returned to the spindle midzone (**Fig. 34 B**; 20:40-30:10 min). In control experiments without the blue light or without iLID (henceforth control), opto-PRC1 was not removed (**Fig. 35 E**). Thus, optogenetic approach allows for acute and reversible control of PRC1 localization in metaphase.

Figure 35. Metaphase spindles in fixed unlabeled U2OS cells immunostained for PRC1 (AF-488, magenta), tubulin (AF-405, green) and stained with SiR-DNA (not shown) (left) in untreated (top) and PRC1 siRNA treated cells (bottom). All images are sum intensity projections of five z-planes. Graph (right;) of PRC1 intensity in untreated (magenta) and PRC1 siRNA treated (green) cells. Data obtained from three independent experiments. **B.** Metaphase spindles in fixed unlabeled U2OS cells

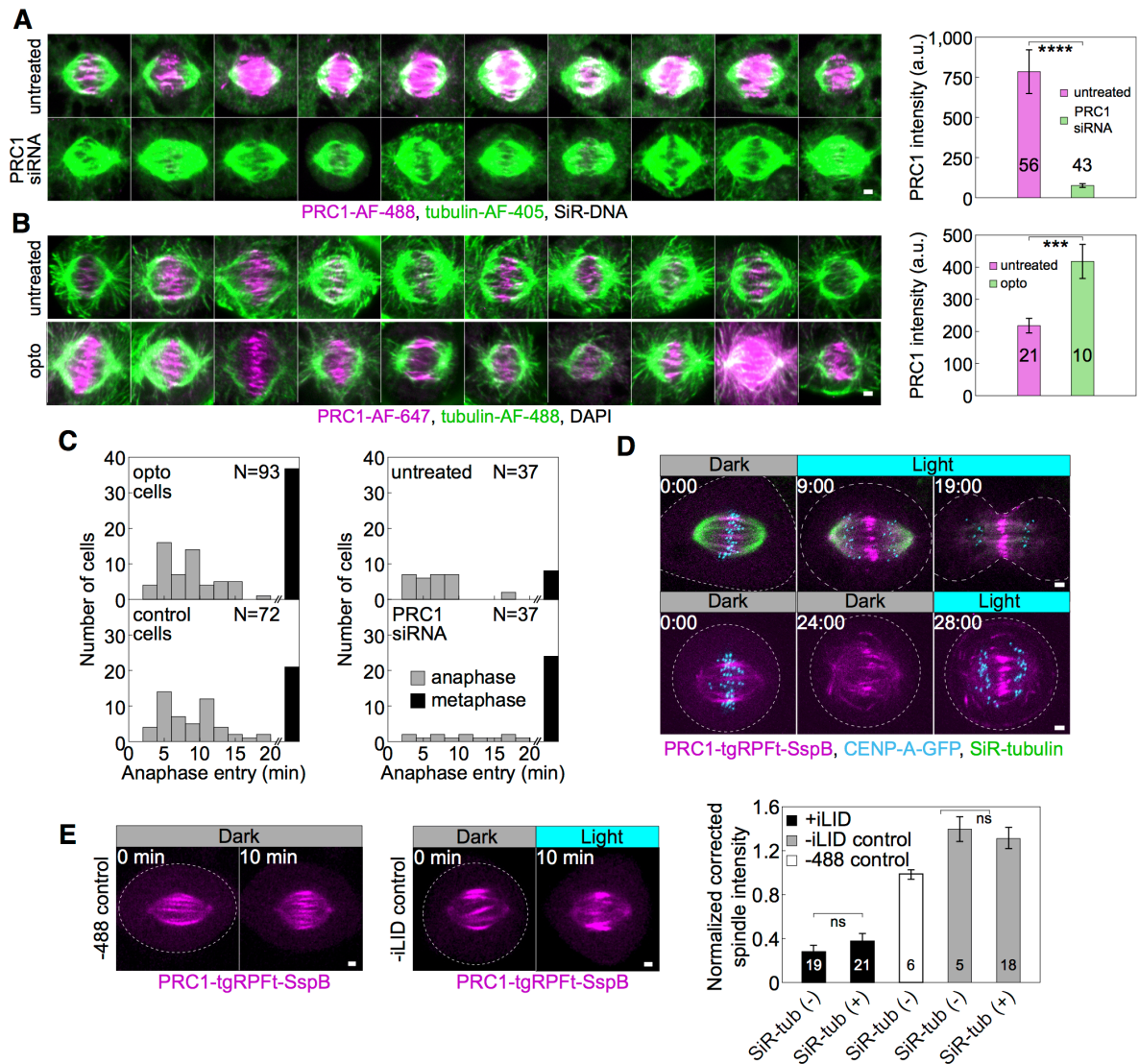immunostained for PRC1 (AF-647, magenta), tubulin (AF-488, green) and stained with DAPI (not shown) (left) in untreated (top) and PRC1 siRNA treated cells with addition of opto-PRC1 (bottom). All images are sum intensity projections of five z-planes. Graph (right;) of PRC1 intensity in untreated (magenta) and cells with depleted endogenous and added opto-PRC1 (green). Data obtained from two independent experiments. **C.** Number of cells that entered anaphase (gray bars) and those remained in metaphase (black bars) during 20 min of exposure to the blue light for opto and control cells (left), and untreated and PRC1 siRNA treated cells (right;). **D.** Time-lapse images of U2OS cells with stable expression of CENP-A-GFP (cyan) where control cell (top) progresses to anaphase during and opto cell (bottom) after 20-min exposure to the blue light. **E.** Time-lapse images of U2OS cells with stable expression of CENP-A-GFP (not shown) and transient expression of opto-PRC1 and iLID-CAAX, non-exposed to the blue light (-488 control, left) and exposed to blue light, but without iLID-CAAX (-iLID control, middle), before and after 10 min of imaging. Graph (right;) shows opto-PRC1 intensities after 10 min of imaging in +iLID cells with and without SiR-tubulin (black), -488 control cells (white) and –iLID control cells with and without SiR tubulin (gray). Note that SiR-tubulin does not affect opto-PRC1 removal. Images are max projection of 3 z-planes. N and numbers inside bars; number of cells. Scale bars; 2 μm. Statistical analysis; t-test. p-value legend as in Fig. 25.

4.7 Dynamics of opto-PRC1 removal and return

The dynamics and spatial pattern of opto-PRC1 removal and return was quantified by measuring the opto-PRC1 intensity on the spindle (**Fig. 36 A,B**). In metaphase cells, 88 ± 3% of opto-PRC1 was removed with a half-time of 4.2 ± 0.1 min after 20 min of exposure to the blue light (**Fig. 36 C**). During opto-PRC1 removal, there was simultaneous decrease in both signal intensity and length of the overlap region (**Fig. 36 B,D**), which may be due to fewer antiparallel regions being positioned laterally than in the central part of the bundle (Mastronarde et al., 1993). The signal of the outermost midzone bundles typically lasted longer than of the inner ones (**Fig. 34 B;** 3:40-6:30). After the blue light was switched off, opto-PRC1 signal restored to 65 ± 1% of the initial intensity within 10 minutes, with return half-time being 0.71 ± 0.04 min (**Fig. 36 C**). The faster PRC1 return to the spindle in comparison with its removal may be due to the higher affinity difference between PRC1 binding to the spindle and to the membrane in the dark than under the light. During the opto-PRC1 return, it initially localized throughout the spindle, with gradual increase in intensity in the spindle midzone (**Fig. 36 B,D**), suggesting that PRC1 has higher unbinding rate outside than within the overlap bundles in the spindle. This result is consistent with PRC1 having a

life-time of several seconds on single microtubules and a 10-fold preference for overlap regions *in vitro* (Subramanian et al., 2010).
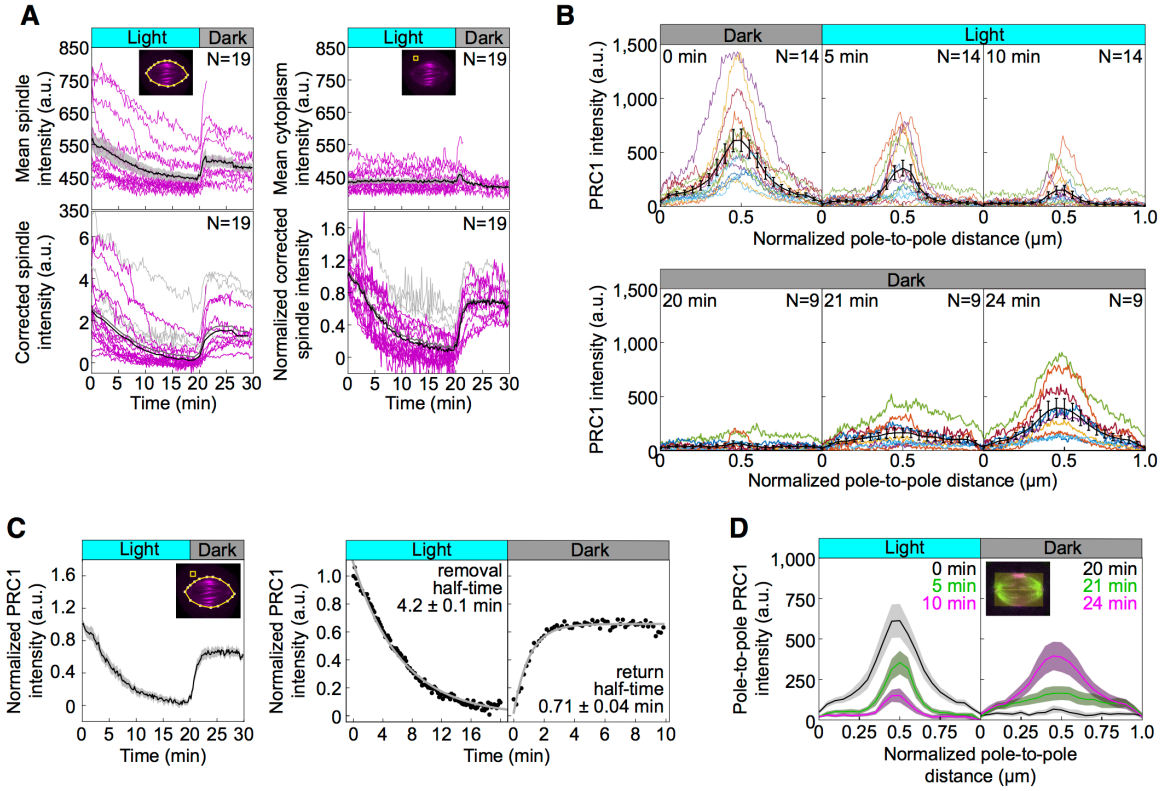
Figure 36. Dynamics of opto-PRC1 removal and return to the spindle. A. Raw opto-PRC1 intensities from individual cells (magenta lines) at the metaphase spindle (top left) and in cytoplasm (top right) during removal and return to the spindle. Mean (thick black line) and s.e.m. (shaded area). Opto-PRC1 intensities at the metaphase spindle corrected for cytoplasm (bottom left) and normalized to the initial value (bottom right). Outliers (gray lines), mean without outliers (thick black line), mean with outliers (thick gray line). Note that outliers are excluded in C. **B.** Pole-to-pole opto-PRC1 intensity during removal (top) and return (bottom) to the spindle as in D. Individual cells (colored lines), mean (thick black line), s.e.m (error bars). **C.** Normalized intensity of opto-PRC1 signal on the spindle (left panel) during its removal (0-20 min) and return (20-30 min). N=15 (individual cells in A). Scheme depicts the areas where opto-PRC1 intensity was measured: spindle (large polygon) and cytoplasm (small square). Exponential fit (gray lines in the right panel) on mean normalized opto-PRC1 spindle intensity (black points) during 20 min of removal and 10 min of return. Formulae y=A*exp(-τ*x) and y=A*exp(-τ*x)+c were used for opto-PRC1 removal and return, respectively. Parameters for PRC1 removal: A=1.111, τ=0.00277 s^{-1} (RSE=0.03), and return: A=-0.635, c=0.656, τ=0.01622 s^{-1} (RSE=0.03). The half-time was calculated by ln2/τ. **D.** Pole-to-pole opto-PRC1 intensity during removal and return to the spindle. Number of cells as in B. Mean and s.e.m are color-coded

corresponding to the time when measured (upper right corners). Scheme depicts the area where opto-PRC1 intensity was measured (yellow) to obtain the mean intensity projection onto the pole-to-pole axis. Mean (thick lines); s.e.m. (shaded areas); N (number of cells).

Interestingly, in the cells that entered anaphase during exposure to the blue light, opto-PRC1 could not be removed with the same efficiency compared to those that remained in metaphase during our optogenetic approach (**Fig. 37 A,** compare with **Fig. 34**). Although opto-PRC1 signal on the membrane appeared upon exposure to the blue light in these cells, it remained in the spindle midzone during imaging (**Fig. 37 A**). To quantify this observation, we perfromed measurements of opto-PRC1 intensity on spindles in anaphase cells in three reference time-points: at the beggining of imaging, while the cells were still in metaphase; at anaphase onset; and 3 min from onset. We found that opto-PRC1 intensities remained similar in all three time points for cells in the experiment, while these intensities decreased significantly in cells that remained in metaphase during exposure to the blue light at comparable time-points (**Fig. 37 B,** see caption). Futhermore, these intensities increased in -iLID control cells (**Fig. 37 B**). Opto-PRC1 intensities at anaphase onset were lower in the experiment compared to -iLID control cells (n=25 and n=31, respectively, p=0.0223). Thus, in the experiment exposure to the blue light prevented additional accumulation of PRC1 on the spindle towards anaphase onset.
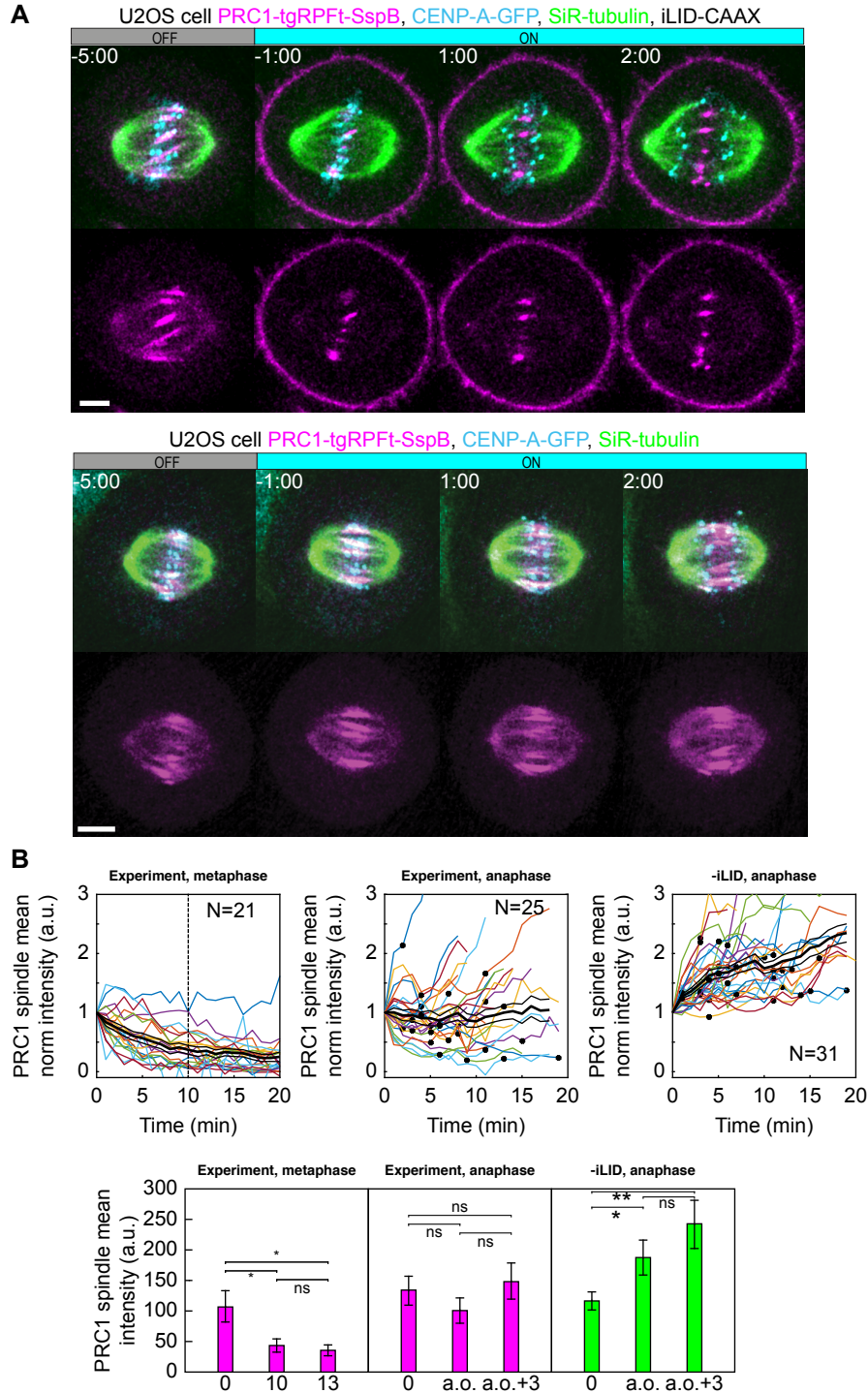
Figure 37. In anaphase opto-PRC1 remains in the spindle midzone. A. Time-lapse images of the spindle in a U2OS cell stably expressing CenpA-GFP (cyan), depleted for endogenous PRC1, with transient expression of opto-PRC1 (magenta) and iLID-CAAX and tubulin stained with SiR-tubulun dye (green) (top). Time-lapse images of the spindle in U2OS cell stably expressing CenpA-GFP (cyan), depleted for endogenous PRC1, with transient expression of opto-PRC1 (magenta), but without iLID-CAAX (-iLID control) (bottom). Anaphase onset is set as time 0. Images are single z-plane, smoothed with 0.1-µm-sigma Gaussian blur. **B.** Normalized mean intensities of opto PRC1

(top) on the spindle in cells with iLID (experiment) that remained in metaphase during exposure to the blue light (left), cells with iLID that entered anaphase (middle) and cells without iLID (control) that entered anaphase (right). Colored lines; opto-PRC1 intensity of individual cells. Thick black lines; mean. Black lines; SEM. Black dots denote time of anaphase onset for each cell. Mean values of opto-PRC1 intensities of these three groups of cells (bottom). For anaphase cells mean values at the beginning of imaging, anaphase onset and three minutes after onset are indicated. In order to be able to compare opto-PRC1 removal in metaphase and anaphase, we calculated mean time of anaphase onset in +iLID cells upon start of imaging, which was 10 min, and therefore intensities in anaphase were to compared to metaphase cells at the beginning of imaging, 10 min and 13 min after beginning of exposure to the blue light. Scale bars 5 μm. N, number of cells. Statistical analysis; t-test. p-value legend as in Fig. 25.

It is known that in metaphase-to-anaphase transition phosphorylation status of PRC1 changes affecting its affinity for binding and bundling of microtubules in overlap regions and thus its turnover, as demonstated for yeast ortholog Ase1 (Cundell et al., 2013; Loiodice et al., 2005; Mollinari et al., 2002). To find the origin of this difference in efficiency of PRC1 removal, we analysed the dynamics of PRC1 in metaphase and anaphase by using florescence recovery after photobleaching (FRAP) in HeLa cells stably expressing PRC1-GFP. We measured the signal intensity over time in a photobleached region on a PRC1-labeled bundle (**Fig. 38**). We found that PRC1 recovery half-time was 3.2 ± 0.1 s in metaphase (N=23 cells) and 6.8 ± 0.2 s in anaphase (N=8) (**Fig. 38**). Moreover, there was a difference of immobile fraction of PRC1 as photobleached region recovered to 64.1 ± 0.5 % of the initial value in metaphase and to 49.1 ± 0.7 % in anaphase (**Fig. 38**). These results indicate that the dynamics of PRC1 decreases from metaphase to anaphase, consistent with similar measurements for the yeast ortholog Ase1 (Loiodice et al., 2005) and provide possible explaination why opto-PRC1 could not be removed in anaphase with the same efficienty as in metaphase.
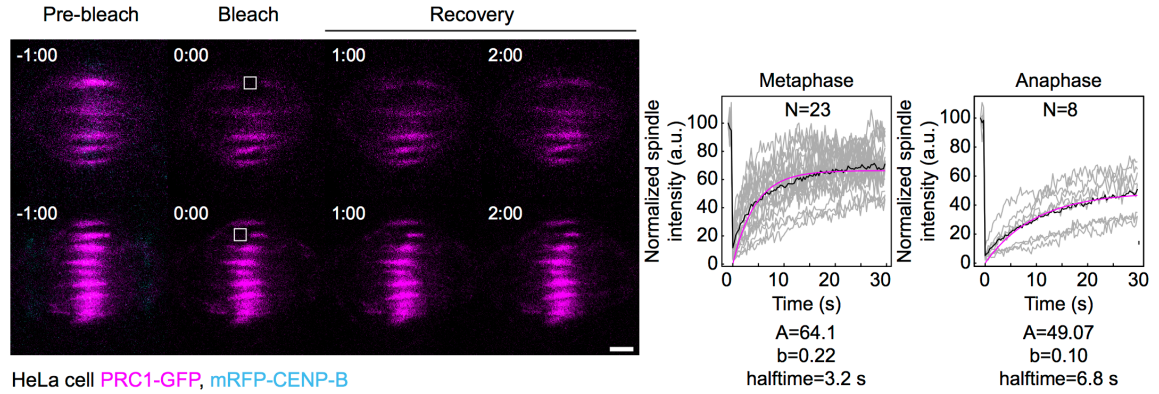
Figure 38. PRC1 is less dynamic in anaphase. Time-lapse images (left) of FRAP in HeLa cells expressing PRC1-GFP (magenta) and transient expression of mRFP-CENP-B (cyan) in metaphase (top row) and anaphase (bottom row). White rectangles show regions of interest (ROIs). Percentage of recovered intensity after photobleaching measured at photobleached regions (ROIs) (right). Gray lines, individual cells. Exponential fit, magenta line. Mean, black line. Scale bar, 2 μm.

4.8 Acute PRC1 removal during metaphase leads to misaligned kinetochores

To test whether bridging fiber has a role in the maintenance of chromosome alignment, acute optogenetic removal of PRC1, a depletion of which is known to perturb bridging fibers (Polak et al., 2017), should affect chromosome positioning at the spindle equator (**Fig. 39 A**). Surprisingly, we observed that the acute removal of opto-PRC1 resulted in movement of sister kinetochore pairs away from the metaphase plate (**Fig. 39 B**), which is not found after long-term PRC1 depletion by siRNA (Polak et al., 2017). Upon opto-PRC1 removal, the distances of sister kinetochore midpoints from the equatorial plane increased (d_{EQ}, **Fig. 39 B,C,D**; **Fig. 40 A,B**). While >95% of kinetochore pairs were found within the region of PRC1 streaks, i.e., less than 2 μm away from the equatorial plane before removal of opto-PRC1, 9.3 ± 2.7% of kinetochore pairs made excursions far outside this region after opto-PRC1 removal (**Fig. 40 B**). The displaced kinetochores were found more often in the inner part of the spindle, i.e., close to the long spindle axis, than in the outer regions (**Fig. 39 E**). Kinetochores fluctuated to a similar extent in the presence and absence of opto-PRC1, but in its absence the displaced kinetochores fluctuated within a region that was offset from the equatorial plane (**Fig. 40 C**). These displaced kinetochores upon opto-PRC1 removal had lower inter-kinetochore distance in comparison to non-displaced ones, suggesting that kinetochore displacement was related to a more severe reduction of tension (**Fig. 39 F**). On average,

kinetochores remained displaced even after opto-PRC1 return (**Fig. 39 D**). These results suggest that PRC1 has a role in keeping kinetochores in tight alignment on the metaphase plate.

The mean inter-kinetochore distance (d_{KC}, **Fig. 39 C**) was reduced when opto-PRC1 was removed (**Fig. 39 G**; **Fig. 40 D**), and the distance after 20 min of exposure to the blue light (0.79 ± 0.01 μm) was closer to metaphase (0.87 ± 0.01 μm) than prometaphase (0.66 ± 0.01 μm) values (see Methods), suggesting that tension was not completely lost and that these changes were not due to kinetochore detachment from k-fibers (**Fig. 40 D**). In agreement with this, the fraction of cells that entered anaphase during image acquisition was similar in control and opto cells (71 ± 5 % N=72, and 60 ± 5 % N=93, respectively; p=0.1, Pearson's Chi-squared test; **Fig. 35 C**), indicating that PRC1 removal did not prevent spindle assembly checkpoint satisfaction. After opto-PRC1 return to the spindle, inter-kinetochore distance increased, implying restoration of tension, though not to the original value (**Fig. 39 G**).
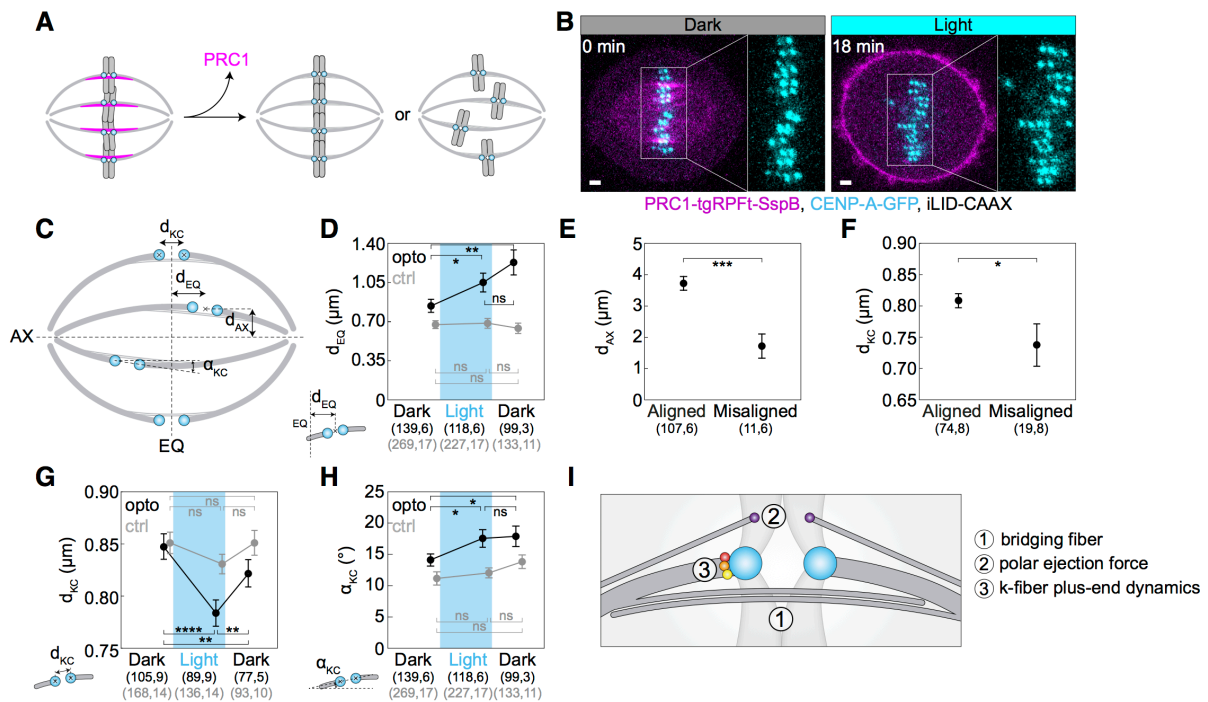
Figure 39. Optogenetic removal of PRC1 disrupts kinetochore alignment on the metaphase plate. A. Schematic representation of possible outcomes of acute removal of PRC1 from the spindle on chromosome alignment. **B.** Spindle in a U2OS cell stably expressing CENP-A-GFP (cyan) with transient expression of opto-PRC1 (magenta) and iLID-CAAX before (0 min, Dark), and at the end of continuous exposure to the blue light (18 min, right). Enlargements show kinetochores only. Images are maximum intensity projections of three z-planes, smoothed with 0.5-pixel-sigma Gaussian blur. Scale bar; 2 μm. **C.** Schematic of measured parameters. d_{KC}, inter-kinetochore distance; d_{EQ}, distance

between sister kinetochore midpoint and equatorial plane (EQ); α_{KC}, angle between sister kinetochore axis and spindle long axis; d_{AX}, distance between sister kinetochore midpoint and spindle long axis. **D.** Measurements of d_{EQ} in opto (black) and control (gray) cells before (0 min, Dark), at the end of continuous exposure (20 min, Light) and 10 min after cessation of exposure to the blue light (30 min, Dark), in U2OS cells expressing CENP-A-GFP. **E.** d_{AX} of aligned (d_{EQ}<2 µm) and misaligned (d_{EQ}=2.5 ± 0.2 µm) kinetochore pairs upon PRC1 removal. **F.** d_{KC} of aligned and misaligned kinetochore pairs upon PRC1 removal. **G.** Measurements of d_{KC}. Legend as in D. **H**. Measurements of α_{KC}. Legend as in D. **I.** Schematic of three mechanisms that could be involved in kinetochore alignment. Cyan rectangles inside graphs indicate exposure to the blue light. Numbers in brackets denote measurements and cells. In D, G, H opto cells are without SiR-tubulin, and control cells include those with and without SiR-tubulin. Error bars; s.e.m. Statistical analysis; t-test (D-H). p-value legend as in Fig. 25.
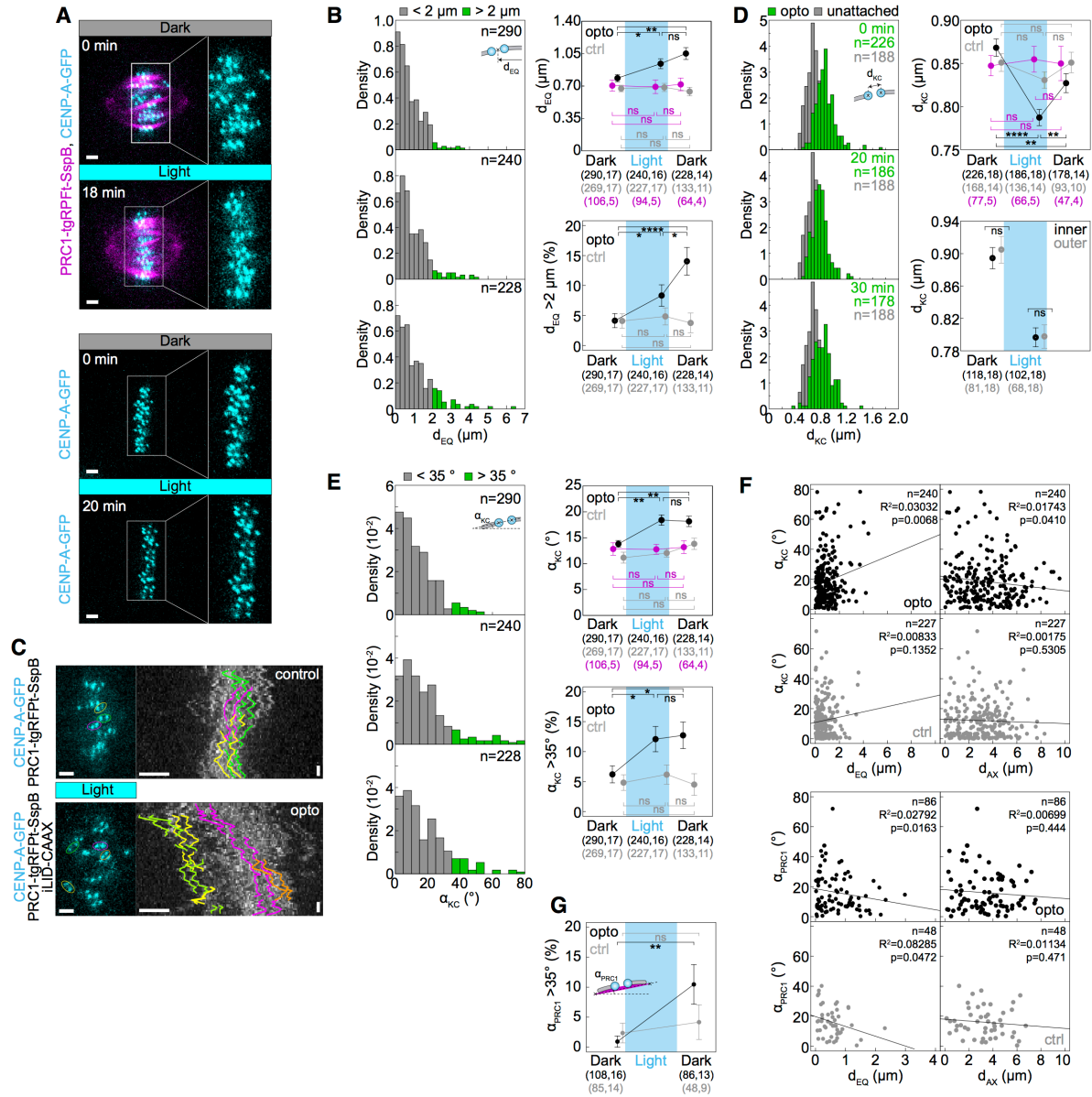
Figure 40. A. Spindle in a U2OS cell stably expressing CENP-A-GFP (cyan) with (top) and without (bottom) transient expression of opto-PRC1 (magenta) before (0 min, Dark) and at the end of continuous exposure to the blue light (18 min, bottom). Enlargements of the boxed regions show kinetochores only. Images are maximum intensity projections of three z-planes, smoothed with 0.5-pixel Gaussian blur. **B.** Density histograms (left) of the distance from the midpoint between sister kinetochores to the equatorial plane, d_{EQ}, for opto U2OS cells before (0 min, top), at the end of continuous exposure (20 min, middle) and 10 min after cessation of exposure to the blue light (30 min, bottom). d_{EQ} greater (green) and lesser than 2 μm (gray) is shown. This corresponds to roughly 95th percentile of opto data before system activation. Percentage of d_{EQ} greater than 2 μm in opto (black) and control (gray) cells (bottom right). Graph (top right) showing d_{EQ} in control (gray) and opto cells with and without SiR-tubulin (black), and cells only expressing CENP-A-GFP (magenta) in corresponding timepoints. **C.** Metaphase plates (left) of control (top) and opto (bottom) U2OS cell

78

expressing CENP-A-GFP (cyan). Corresponding kymographs show kinetochore fluctuations during last 10 min of 20-min exposure to the blue light, when there was no PRC1 on the spindle in opto cells. Kinetochore tracks are color-coded with respect to corresponding sister pairs (left). Note that in opto cell (bottom) the displaced kinetochores (yellow, green) showed similar extent of oscillations as non-displaced kinetochores in opto (bottom) and all in control (top) cells (N=10 cells in each condition). Vertical scale bar; 1 min. **D.** Density histograms (left) of inter-kinetochore distance, d_{KC}, for opto U2OS cells (green) for time-points as in B, overlaid on density histogram of unattached d_{KC} from early prometaphase cells (mean: 0.66 ± 0.01 µm, N=7, n=188) (gray). Inter-kinetochore distance (d_{KC}) (top right) in control (gray) and opto cells with and without SiR-tubulin (black), and cells only expressing CENP-A-GFP (magenta) in same timepoints. Inter-kinetochore distance (d_{KC}) (bottom right) of inner (black) and outer (gray) kinetochore pairs before and 20 min after exposure to the blue light. **E.** Density histogram (left) of angle between sister kinetochore axis and the long spindle axis, α_{KC}, for opto U2OS cells for time-points as in B. α_{KC} greater (green) and lesser than 35° (gray) is shown. This corresponds to roughly 95th percentile of opto data before system activation. Percentage of α_{KC} greater than 35° in opto (black) and control (gray) cells (bottom right). Graph (top right) showing α_{KC} in control (gray) and opto cells with and without SiR-tubulin (black), and cells only expressing CENP-A-GFP (magenta) in timepoints as in B. **F.** Graphs show α_{KC} versus corresponding d_{EQ} and the distance from the midpoint between sister kinetochores to the long spindle axis, d_{AX} (left), and α_{PRC1} versus d_{EQ} and d_{AX} in opto (top, black) and control (bottom, gray) cells. Kinetochore parameters correspond to 20 min after continuous exposure to the blue light, and PRC1 parameters correspond to 10 min after cessation of exposure. Note that PRC1 is not on the spindle at 20 min in opto cells. Black lines show linear regression. **G.** Percentage of angles between the line connecting the end points of the PRC1 streak and the long spindle axis, α_{PRC1}, greater than 35° in opto (black) and control (gray) cells before exposure and 10 min after cessation of exposure to the blue light. Cyan rectangles inside graphs indicate exposure to the blue light. Numbers in brackets; number of measurements and cells, respectively. Time; min. n; number of measurements. Horizontal scale bars; 2 µm. Statistical analysis; t-test and two-proportions z-test. R2, coefficient of determination. p-value legend as in Fig. 25.

To investigate the influence of acute PRC1 removal on the orientation of sister kinetochores, we measured the angle between sister kinetochore axis and long spindle axis (α_{KC}, **Fig. 39 C**). We observed that removal of opto-PRC1 caused misorientation of sister kinetochores, i.e., increased α_{KC} (**Fig. 39 B,H**; **Fig. 40 A,E**). Misoriented kinetochores were found at a larger distance from the equatorial plane and closer to the long spindle axis (**Fig. 40 F**). Interestingly, sister kinetochore pairs remained misoriented even after opto-PRC1 return (**Fig. 39 H**). Similarly, PRC1 bundles were misoriented upon PRC1 return (see Methods, **Fig. 40**

G). These results suggest that when PRC1 returns to the overlaps whose geometry was perturbed by PRC1 removal, it likely confines the chromosomes in new positions and orientations.

The observed effects of PRC1 removal on inter-kinetochore distance, kinetochore alignment and orientation did not change when SiR-tubulin was added (compare **Fig. 39 D,G,H** without SiR-tubulin and **Fig. 40 B,D,E** including SiR-tubulin stained cells). The effects of PRC1 removal were found neither in control experiments without iLID, nor in a different set of control experiments where cells without opto-PRC1 and without iLID were exposed to the same laser illumination protocol (**Fig. 39 D,G,H**; **Fig. 40 A,B,D,E**), suggesting that the observed effects were not a consequence of laser photodamage. We conclude that PRC1 plays a role in maintaining kinetochore alignment and orientation within the metaphase plate.

4.9 PRC1 removal during metaphase increases the frequency of lagging kinetochores in anaphase

To test to what extent the acute removal of PRC1 during metaphase affects chromosome segregation, we measured the frequency of lagging kinetochores. We found that lagging kinetochores occurred more frequently when opto-PRC1 was being removed than in control cells (**Fig. 41 A**). Opto cells that showed lagging kinetochores in anaphase had a slightly smaller inter-kinetochore distance before anaphase than opto cells without lagging kinetochores (**Fig. 41 B**), suggesting that a decrease in tension may be involved in the imperfect kinetochore segregation. The cells with lagging kinetochores did not have a larger average kinetochore misalignment in metaphase (**Fig. 41 B**), which indicates that misalignment and lagging kinetochores are not linked on the cell level, though they may be linked locally on individual kinetochores.

As perturbation of the PRC1-CLASP1 interaction and the consequent absence of CLASP1 from the spindle midzone results in lagging chromosomes (Liu et al., 2009), we inspected the localization of CLASP1 and found that it did not accumulate between segregating chromosomes in opto HeLa cells stably expressing EGFP-CLASP1 (**Fig. 41 C**). Thus, the observed higher occurrence of lagging kinetochores could be attributed to changes in tension during metaphase, perturbed recruitment of CLASP1 to the spindle midzone by PRC1 during early anaphase, or a combination of both effects.
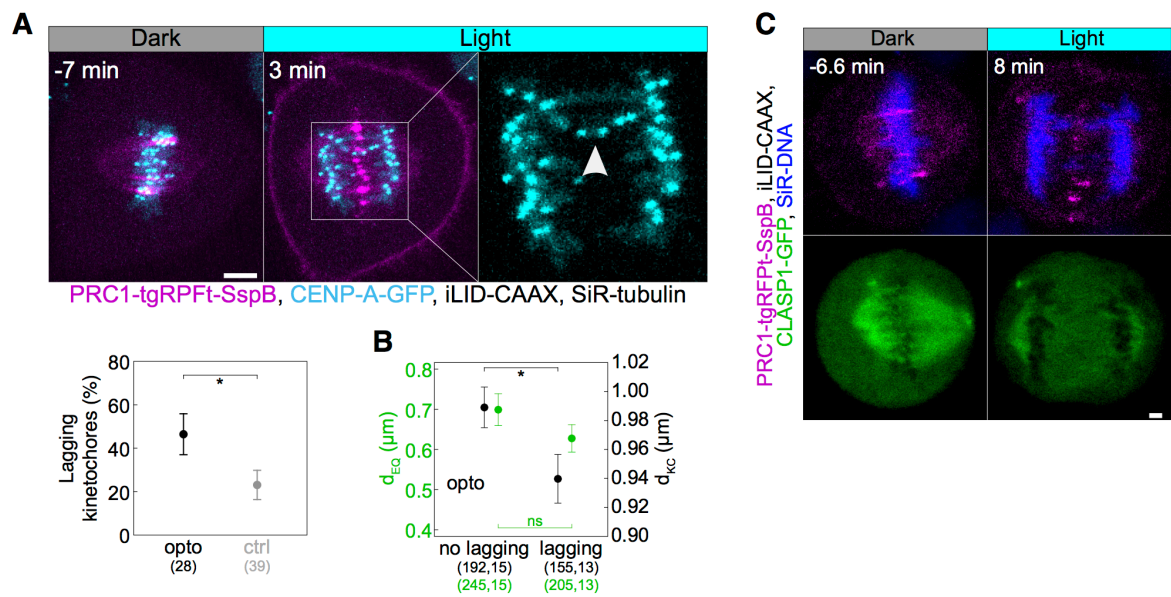
Figure 41. Lagging chromosomes appear in early anaphase after opto-PRC1 removal in metaphase. A. Time-lapse images of a spindle in a U2OS cell as in Fig. 34 B, stained with SiR-tubulin (not shown). Anaphase onset is at time 0 min. Lagging kinetochores can be seen at 3 min (middle). Enlargement shows kinetochores only, where lagging kinetochores are indicated with a white arrowhead. Occurrence of lagging kinetochores in anaphase of opto (black) and control (gray) U2OS cells (bottom left). **B.** dKC (black) and dEQ (green) in opto anaphase cells with and without lagging kinetochores. **C.** Time-lapse images of HeLa cell stably expressing EGFP-CLASP1 with transient expression of opto-PRC1 (magenta) and iLID-CAAX, and stained with SiR-DNA (blue). Top (merge tgRFPt and SiR-DNA), bottom (GFP). Anaphase onset is set as time 0 min. Note the absence of GFP signal in the spindle midzone and lagging chromosomes at 8 min. Images are maximum intensity projections of 3 z-planes, smoothed with 0.5-pixel Gaussian blur. Numbers in brackets denote measurements and cells; single numbers denote cells. Statistical analysis; two-proportions z-test (A), t-test (B).

4.10 Acute PRC1 removal leads to longer antiparallel overlap zones within the bridging fibers

Factors that could contribute to the altered chromosome alignment and occurrence of lagging kinetochores upon opto-PRC1 removal are changes related to 1) microtubules in the bridging fibers, 2) polar ejection forces, and/or 3) proteins that modulate the dynamics of k-fiber plus-ends (**Fig. 39 I**). Because PRC1 crosslinks microtubules within bridging fibers (Kajtez et al., 2016; Polak et al., 2017), effects of PRC1 removal on those microtubules were firstly tested.

An important aspect of the bridging fiber that may affect chromosome alignment is the dynamics of microtubules that make up these fibers. To explore their dynamics, an assay for tracking the growing plus ends of individual microtubules in the bridging fiber was developed by using cells expressing the plus end marker EB3 (Stepanova et al., 2003) tagged with GFP (**Fig. 42**). We followed individual EB3 spots in the spindle and identified the ones belonging to a bridging fiber as the spots that move towards a kinetochore, cross the region between this kinetochore and its sister, and move beyond it towards the other spindle pole (**Fig. 42 A-C**). We found 1.8 ± 0.2 EB3 spots per minute per bridging fiber in control cells, consistent with our previous work (Kajtez et al., 2016), showing that bridging fibers are dynamically remodeled during metaphase (**Fig. 42 D**). This number was similar after opto-PRC1 removal (**Fig. 42 D**), suggesting that the number of dynamic microtubules in the bridge is largely independent of PRC1.

To assess the changes in the dynamics of bridging microtubules, EB3 spots in the bridge were followed from the time when they can be distinguished from neighboring spots near the pole until they disappear in the opposite spindle half, which is interpreted as the moment when the microtubule stops growing (Maurer et al., 2012). Interestingly, EB3 tracks were longer after opto-PRC1 removal than in control cells (**Fig. 42 B,C**), but the velocities of the EB3 spots were not affected by opto-PRC1 removal (**Fig. 42 E**). In agreement with these results, kymographs of the central region of the spindle show that EB3 spots reach deeper into the opposite half of the spindle after opto-PRC1 removal (**Fig. 42 F**; **Fig. 43 A**). Thus, acute removal of PRC1 results in longer bridging microtubules, which is not a consequence of altered microtubule growth rate, but most likely due to a reduced microtubule catastrophe rate.
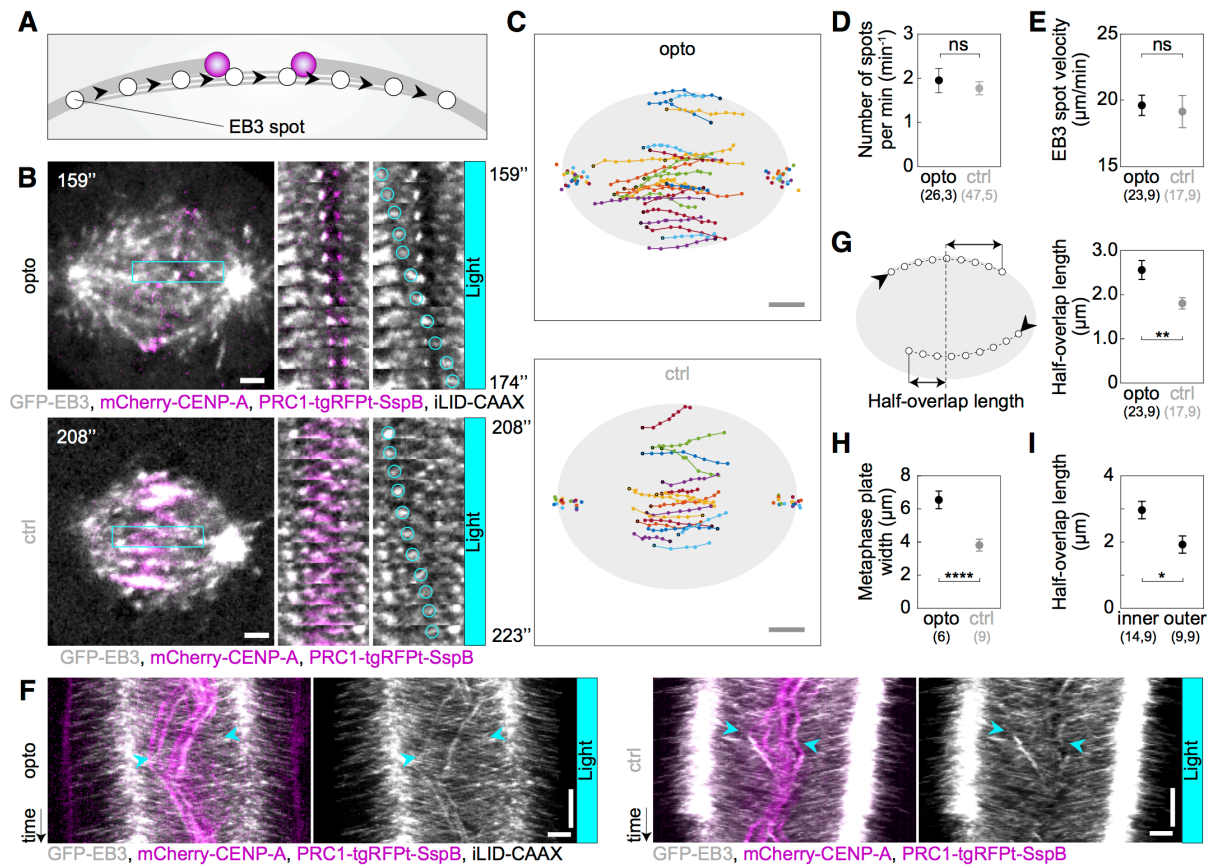
Figure 42. Acute removal of PRC1 elongates antiparallel overlaps within the bridging fibers. A. Schematic of the trajectory of an EB3-marked plus end (white circles) within the bridging fiber, defined as a spot passing the sister kinetochore region (magenta). **B.** Spindles (left) in U2OS cells with stable expression of 2xGFP-EB3 (gray) and mCherry-CENP-A (magenta), depleted for endogenous PRC1, with transient expression of opto-PRC1 and iLID-CAAX (opto; top) and opto-PRC1 only (control; bottom). Montage of the boxed region over time is shown as merged channels (middle) and GFP (right; the tracked spot is encircled). Time after 10 min of imaging protocol required for removal of PRC1 is shown. Note that in opto cell (top) PRC1 is removed from the spindle. Images are single z-planes smoothed with 0.5-pixel-sigma Gaussian blur. **C**. Trajectories of tracked EB3 spots (connected dots) in opto (top) and control (bottom) cells. Black dot; start of trajectory. Single dots on the sides; spindle poles. **D.** Number of EB3 spots per minute within the bridging fiber in opto (black) and control (gray) cells. **E.** EB3 spot velocity within the bridging fiber in opto (black) and control (gray) cells. **F.** Kymographs of opto (left) and control (right;) cells after 10 min of imaging protocol required for removal of PRC1, merge (left) and GFP (right;). Cyan arrowheads mark the beginning and end of an individual EB3 spot trajectory. Note the difference in the position of indicated track ends with respect to the equatorial plane. **G.** Half-overlap length (left) defined as the distance (double arrow) between the end-point of the EB3 spot trajectory and the equatorial plane (dashed line). Black arrowhead; start of trajectory. Half-overlap length in opto (black) and control (gray) cells measured as in scheme (left) and retrieved from tracks shown in B (right;). **H.** Metaphase plate width in opto (black) and control

83

(gray) cells measured from kymographs as the largest distance between kinetochore pairs positioned on the opposite sides of the spindle equator in the first two minutes after 10 min of imaging protocol required for removal of PRC1. As kinetochores remain within the PRC1-labeled region in control cells, the metaphase plate width in these cells was measured as the PRC1 streak length. **I.** Half-overlap length in opto cells for inner (dAX≤2 μm) and outer (dAX>2 μm) overlaps. Filled cyan rectangles indicate exposure to the blue light. Numbers in brackets denote measurements and cells; single numbers denote cells. Error bars; s.e.m. Scale bars; 2 μm. Statistical analysis; t-test. p-value legend as in Fig. 25.

EB3 tracks allowed us to estimate the length of the overlap zone of antiparallel microtubules in the bridging fiber, which currently cannot be measured after PRC1 removal because PRC1 itself is the only available marker of antiparallel overlaps in the spindle. The overlap half-length was defined as the distance beyond the equatorial plane that an EB3 spot covers while moving within the bridging fiber from one spindle half into the other (**Fig. 42 G**, left), where this microtubule can form antiparallel overlaps with the oppositely oriented microtubules extending from the other pole. In control cell, the overlap half-length was 1.8 ± 0.2 μm (n=17 spots in N=9 cells; **Fig. 42 G,** right), which corresponds well to the overlap half-length measured as the half-length of PRC1 streaks in this cell line, 0.5x(3.8 ± 0.4) μm (N=9 cells; **Fig. 42 H**), validating our method for overlap length measurement based on EB3 tracks. After opto-PRC1 removal, the overlap half-length increased to 2.6 ± 0.2 μm (n=23 spots in N=9 cells; **Fig. 42 G**). In contrast, treatment with PRC1 siRNA did not result in a change of overlap length with respect to mock siRNA (**Fig. 43, B-E**). Thus, the antiparallel overlaps became on average 40% longer after acute, but unchanged after long-time PRC1 removal.

Interestingly, the overlaps were especially long in the inner part of the spindle, whereas those on the spindle periphery were similar to overlaps in control cells (**Fig. 42 I**). This spatial difference is correlated with our findings that PRC1 is removed faster from the inner bundles (see **Fig. 34 B**) and that displaced and misoriented kinetochores are found more often in the inner than in the outer spindle region (see **Fig. 39 D,E,H**), suggesting a mechanistic link between the overlap length and kinetochore positioning.
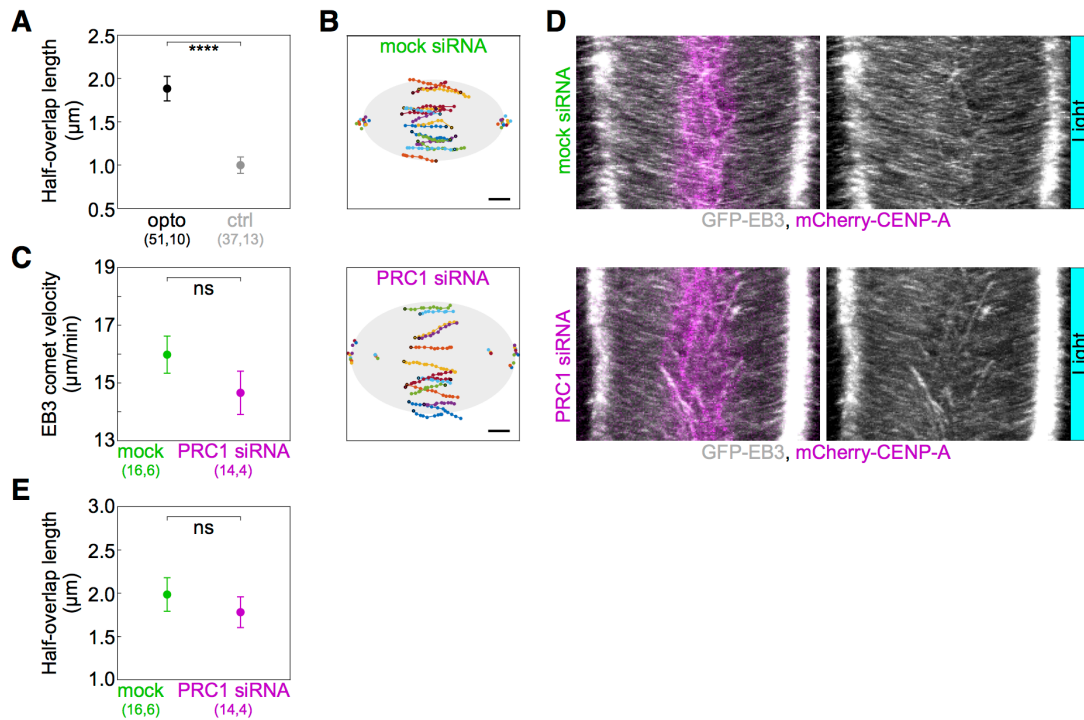
Figure 43. A. Half-overlap length in opto (black) and control (gray) U2OS cells expressing 2xGFP-EB3 measured from kymographs as in Fig. 7 F, as the distance of spot's track end-point to the equatorial plane. All measurements were performed within 2 min following the 10 min imaging protocol required for removal of PRC1. **B.** Trajectories of all tracked EB3 spots (connected dots) in mock (top) and PRC1 siRNA (bottom) treated U2OS cells expressing 2xGFP-EB3. Black dot; start of trajectory. Single dots on the left and the right side; spindle poles. **C.** Velocity of EB3 spots within the bridging fiber in mock (green) and PRC1 siRNA treated (magenta) cells. **D.** Kymographs of mock (top) and PRC1 siRNA (bottom) treated U2OS cells expressing 2xGFP-EB3 after 10 min of imaging protocol required for removal of PRC1. Left (merge mCherry and GFP), right (GFP). **E.** Half-overlap length in mock (green) and PRC1 siRNA (magenta) treated U2OS cells expressing 2xGFP-EB3 measured as in Fig. 42 G and retrieved from tracks showed in B.

Filled cyan rectangles indicate exposure to the blue light. Numbers in brackets denote measurements and cells; single numbers denote cells. Error bars; s.e.m. Scale bars; 2 μm. Statistical analysis; t-test. p-value legend as in Fig. 25.

4. 11 Removal of PRC1 reduces the number of microtubules in the bridging fibers

To test to what extent PRC1 removal in metaphase affects the number of microtubules in the bridging fibers (**Fig. 44 A**), we visualized microtubules by using SiR-tubulin, a far-red tubulin dye excited by red light (Lukinavicius et al., 2014), which allowed us to observe microtubules both when the blue light is turned on and switched off. Intensity profiles across the spindle midzone revealed that SiR-tubulin intensity maxima were lower upon PRC1 removal and increased after its return (**Fig. 45 A**). Measurements of SiR-tubulin signal intensity between and lateral from sister kinetochores showed that upon PRC1 removal the tubulin signal was reduced specifically in the bridging fibers (**Fig. 44, A-C**). As an alternative to SiR-tubulin, which is a taxol-based dye that may affect microtubule dynamics (Lukinavicius et al., 2014), we tested YFP-tubulin, but the excitation laser for YFP also activated the optogenetic system (Wang and Hahn, 2016) (**Fig. 45 B**).

Finally, we used tubulin-GFP to determine tubulin signal intensities of the bridging fibers and k-fiber tips upon acute removal of PRC1 (**Fig. 44 A,D,E**; **Fig. 45 C-F**; see Methods). Upon exposure to the blue light, tubulin signal intensity in the bridging fibers decreased ~2.5 fold, which corresponds to 5.6 ± 0.9 microtubules given that the average number of microtubules in the bridging fiber is 14 (Kajtez et al., 2016). Together with the finding that the number of growing microtubules in the bridging fiber is similar with and without PRC1 (**Fig. 42 D**), this result implies that in the presence of PRC1 the bridge contains more microtubules with a smaller fraction of them being dynamic than without PRC1, and that PRC1 removal leads mainly to disassembly of non-dynamic microtubules. Upon PRC1 return the intensity and thus the number of microtubules remained low (**Fig. 44, D-F**; **Fig. 45 D**), possibly as a consequence of the perturbed spindle architecture in the absence of PRC1, which may be able to recover after a longer time period. Importantly, the intensity at the position lateral from the k-fiber tips was unaltered (**Fig. 44 G**), suggesting that the k-fibers were not affected by PRC1 removal. Thus, acute removal of PRC1 and its return change the number of microtubules specifically in the bridging fibers.
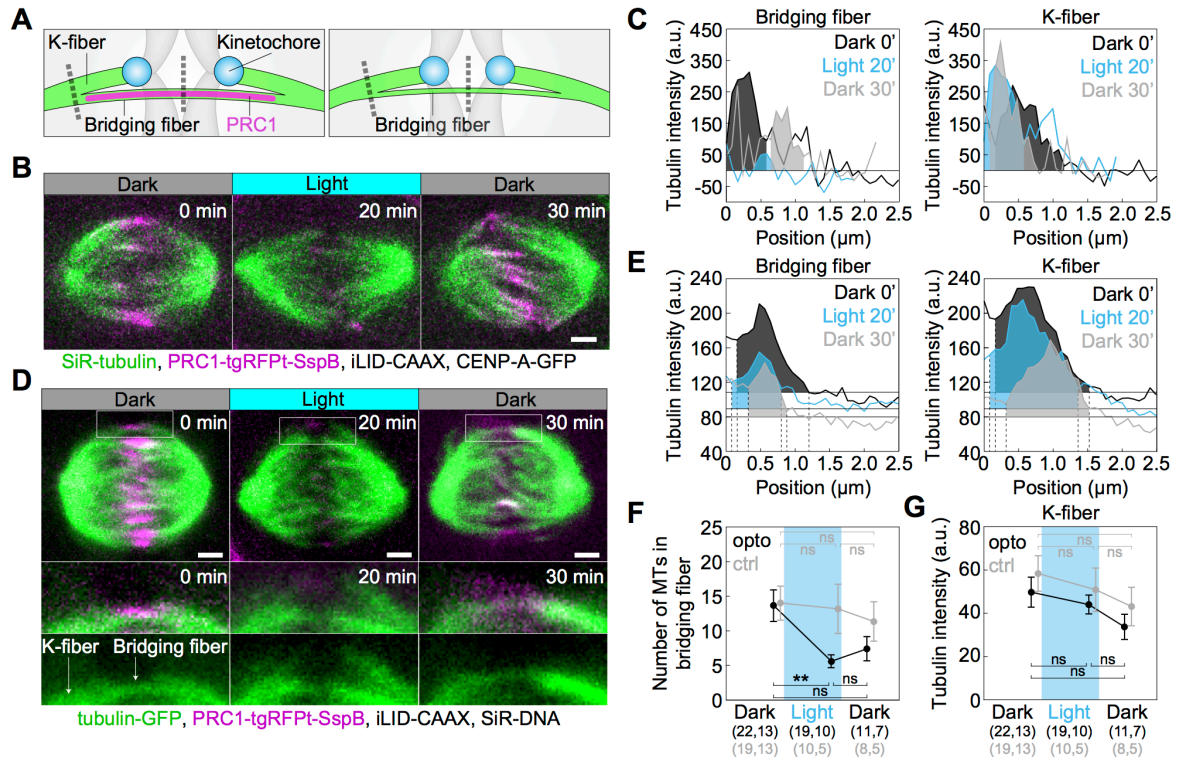
Figure 44. Optogenetic removal of PRC1 reduces bridging fibers and straightens the spindle contour. A. Schematic of PRC1 (magenta) removal from bridging fibers and positions where bridging fiber and k-fiber intensities were measured (dashed lines). **B.** Spindle in a U2OS cell with stable expression of CENP-A-GFP (not shown), depleted for endogenous PRC1, with transient expression of opto-PRC1 (magenta) and iLID-CAAX, and stained with SiR-tubulin (green), before exposure to the blue light (0 min, Dark), at the end of continuous exposure to the blue light (20 min, Light), and 10 min after cessation of exposure to the blue light (30 min, Dark). Images are a single z-plane smoothed with 0.5-pixel-sigma Gaussian blur. **C.** Background-corrected SiR-tubulin intensity profiles of the bridging fiber (left) and k-fiber (right) for cell shown in B (0 min, black; 20 min, cyan; 30 min, gray). **D.** Spindle in a HeLa cell with stable expression of tubulin-GFP (green), depleted for endogenous PRC1, with transient expression of opto-PRC1 (magenta) and iLID-CAAX, and stained with SiR-DNA (not shown), before exposure to the blue light (0 min, Dark, left), at the end of continuous exposure to the blue light (20 min, Light, middle) and 10 min after cessation of exposure to the blue light (30 min, Light, right). Enlargements of the boxed region (middle: merge, bottom: GFP) are shown. Note that at 20 min opto-PRC1 is absent from the spindle. **E.** Graphs showing tubulin-GFP intensity profiles of the bridging fiber (left) and k-fiber (0 min, black; 20 min, cyan; 30 min, gray) for cell shown in D. Horizontal line marks the background signal, vertical dashed lines delimit the area (shaded) where signal was measured. **F.** Number of microtubules in the bridging fiber in opto HeLa cells (i.e., where PRC1 was removed; black) and control (gray) in same time-points as in D. The bridging fiber intensity in control cells before exposure to the blue light is set to correspond to 14 microtubules (see Fig. 45 D). **G.** Tubulin-GFP signal intensity laterally from k-fiber tip in opto (black)

and control (gray) at time-points as in D. Cyan rectangles inside graphs indicate exposure to the blue light. Numbers in brackets; number of measurements and cells, respectively. Error bars; s.e.m. Scale bars; 2 μm. Statistical analysis; t-test. p-value legend as in Fig. 25.

Given that the bridging fiber is under compression (Kajtez et al., 2016), reduction of number of microtubules in the bridging fiber is expected to reduce this compression and thus to straighten the k-fibers (**Fig. 45 G**). Tracking of the pole-to-pole contour of the outermost k-fibers revealed that PRC1 removal indeed straightened the k-fibers and thus made the spindle diamond-shaped (**Fig. 45, H-K**). This result provides further support to the finding that the bridging fibers largely disassemble upon acute PRC1 removal.

Since bridging fibers are nevertheless present upon PRC1 removal, we asked how the residual microtubules are bundled together. Eg5/kinesin-5, which localizes in the bridging fibers (Kajtez et al., 2016; Mann and Wadsworth, 2018), was still detectable in these fibers after PRC1 siRNA (**Fig. 45 L**). Thus, we propose that microtubule crosslinkers such as Eg5 crosslink the remaining microtubules in the bridge after acute PRC1 removal.
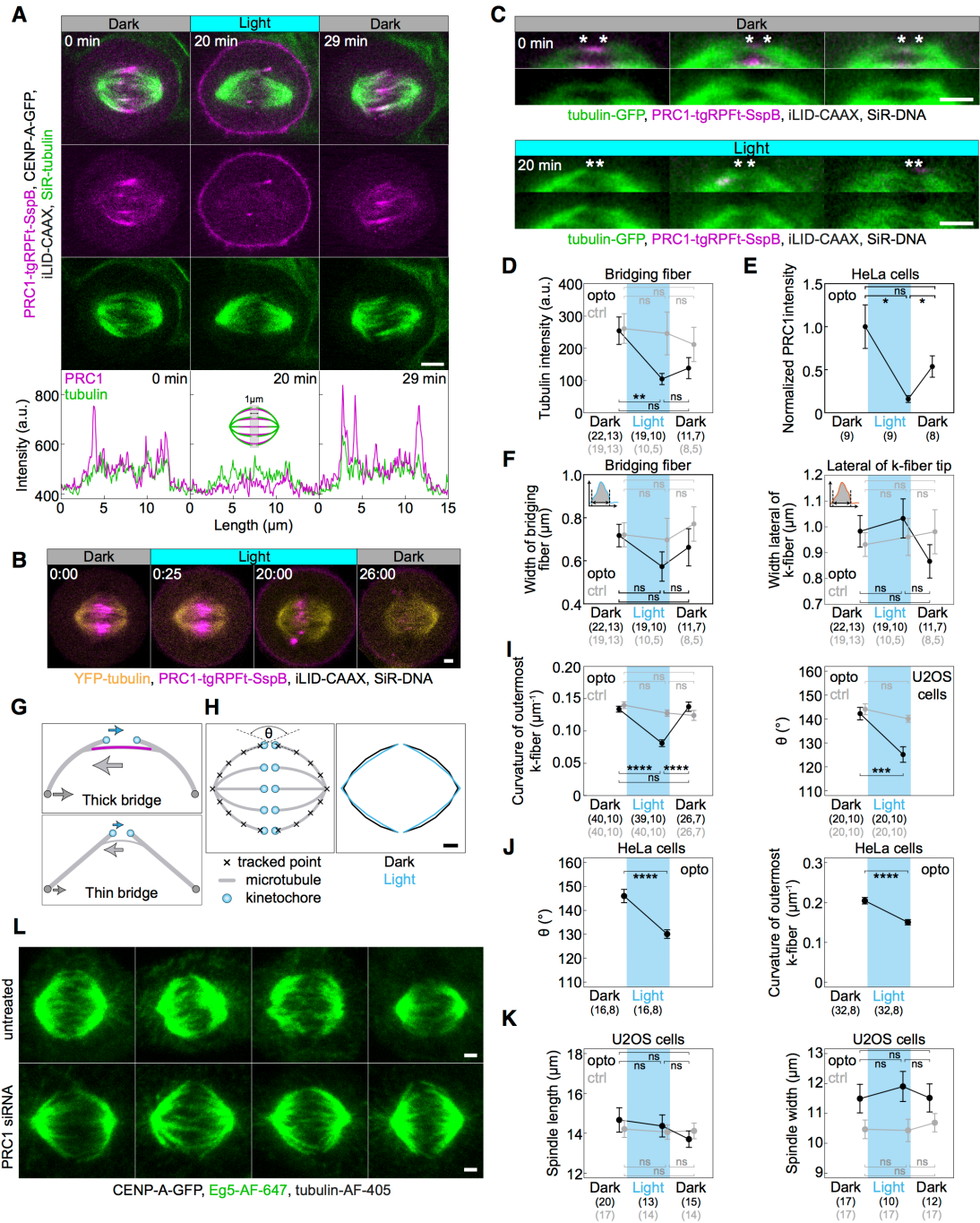
Figure 45. A. Spindle in a U2OS cell stably expressing CENP-A-GFP (not shown), with transient expression of opto-PRC1 (magenta) and iLID-CAAX, and stained with SiR-tubulin (green) before (0 min, Dark), at the end of continuous exposure (20 min, Light) and 9 min after cessation of exposure to the blue light (29 min, Dark). Top (merge), middle (tgRFPt), bottom (SiR). Graphs (bottom) correspond to signal intensity profiles of opto-PRC1 (magenta) and SiR-tubulin (green) taken across equatorial plane in shown spindles. Profile intensities were acquired on individual z-planes using a 1-μm thick line across the spindle midzone. Images are individual z-plane, smoothed with 0.5-pixel-sigma Gaussian blur. Scale bar; 5 μm. **B.** Time-lapse image of a HeLa cell stably expressing YFP-tubulin (yellow), transiently opto-PRC1 (magenta) and iLID-CAAX and stained with SiR-DNA dye

(not shown). In 0:00 (Dark), 561 (opto-PRC1), and 514 (tubulin) + 652 (SiR-DNA) nm lasers are used stack-sequentially. From 0:25-20:00 (Light), 561 and 488+514+652 nm lasers are used stack-sequentially, every 25 s. Note that in 0:00 min, opto-PRC1 is not present on the membrane as in Fig. 1 B. However, in the first frame of Light sequence, 0:25, weak signal of opto-PRC1 is present on the membrane even though opto-PRC1 was imaged in stack before 488 nm laser was on. Also, opto-PRC1 is visible on the membrane 6 min after (26:00, Dark) 488 nm laser was turned off. This is a consequence of 514 nm laser, used to visualize YFP, being able to activate optogenetic system. **C.** Enlargements of spindles in HeLa cells with stable expression of tubulin-GFP (green), depleted for endogenous PRC1, with transient expression of opto-PRC1 (magenta) and iLID-CAAX, and stained with SiR-DNA (not shown), before exposure to the blue light (0 min, Dark, top; first row: merge, second row: GFP) and at the end of continuous exposure to the blue light (20 min, Light, bottom; first row: merge, second row: GFP). Note that at 20 min opto-PRC1 is absent from the spindle. Images do not belong to the same cell. Asterisks mark the position of kinetochores. All images are single z-plane smoothed with 0.5-pixel-Gaussian blur. Scale bar; 2 μm. **D.** Tubulin-GFP signal intensity of the bridging fibers in opto (black) and control (gray) HeLa cells before (0 min, Dark), at the end of continuous exposure (20 min, Light) and 10 min after cessation of exposure to the blue light (30 min, Dark). Signal intensity is measured as the area under the peak shown in Fig. 9 E. **E.** Graph showing normalized PRC1 intensity on the spindle in opto HeLa tubulin-GFP cells used for measurements in D. **F.** Width of the bridging fiber (left) and microtubule bundle lateral from k-fiber tip (right) in opto (black) and control (gray) HeLa cells at time-points as in D, measured as shown in schemes (upper left corners). **G.** Top: Schematic of force-balance in the spindle where compression in the bridging fiber (green arrow) balances compression at the poles (gray arrow) and tension at kinetochores (cyan arrow). Bottom: Upon PRC1 removal, reduction of number of microtubules in the bridging fiber is expected to reduce compression in the bridging fiber and at the poles, leading to k-fiber straightening. **H.** Outermost k-fiber contours in opto U2OS cells before (black, Dark) and at the end of continuous exposure to the blue light (cyan, Light) plotted by connecting mean positions of all tracked points. Scheme (left) depicts how contours were tracked. θ; angle between outermost k-fibers. **I.** Curvature of the outermost k-fibers (left) in opto (black) and control (gray) U2OS cells in same time-points as in B. Angle between outermost k-fibers (right) in opto (black) and control (gray) U2OS cells at first two time-points as in B. **J.** Angle between (left) and curvature (right) of the outermost k-fibers in HeLa cells. **K.** Spindle length (left) and width (right) in opto (black) and control (gray) U2OS cells at timepoints as in D. **L.** Metaphase spindles in fixed U2OS cells stably expressing CENP-A-GFP (not shown) immunostained for Eg5 (AF-647, green) and tubulin (AF-405, not shown) in untreated (top) and PRC1 siRNA treated cells (bottom). All images are sum intensity projections of five z-planes. Scale bar; 2 μm. Cyan rectangles inside graphs indicate exposure to the blue light. Numbers in brackets; number of measurements and cells, respectively. Statistical analysis; t-test. p-value legend as in Fig. 25.

4.12 Kif4A, Kif18A, and MKLP1 localize in the bridge during metaphase in a PRC1-dependent manner

To investigate the mechanism of bridging microtubule regulation via PRC1, we analyzed the localization of major proteins that regulate spindle microtubule dynamics and/or are binding partners of PRC1: Kif4A, CLASP1, Kif18A, CENP-E and MKLP1 (Al-Bassam et al., 2010; Bieling et al., 2010b; Bringmann et al., 2004; Gruneberg et al., 2006; Kurasawa et al., 2004; Liu et al., 2019; Maiato et al., 2003; Mayr et al., 2007; Stumpff et al., 2008; Stumpff et al., 2012; Yu et al., 2016) before and after PRC1 removal in metaphase (**Fig. 46** and **Table 1**).

We first looked at the localization of these proteins in the bridging fiber. Surprisingly, we found that Kif4A, Kif18A, and MKLP1 localize in the bridge during metaphase, visible as thin lines across or next to the location of sister kinetochores (**Fig. 46 A**). These proteins were not detectable in the bridge after both acute (opto) and long-term (siRNA) PRC1 removal, and returned to the bridge upon PRC1 return (**Fig. 46 B,C,** see also **Fig. 47 A,B** for Kif18A; **Table 1**). CLASP1 and CENP-E also showed weak localization in the bridge, which in the case of CENP-E agrees with a recent study that clearly showed its presence in the bridge by using super-resolution microscopy (Steblyanko et al., 2020).

Among the tested proteins, only MKLP1 was exclusively localized in the bridging fibers, co-localizing with PRC1 (**Fig. 46, A-C**; **Fig. 47, C-F**). Even though MKLP1 was completely removed from the spindle by acute PRC1 removal, it was not detected at the cell membrane together with PRC1. It may be that MKLP1 binds rather weakly to PRC1 in metaphase and/or that the absence of PRC1 decreases its affinity for microtubules. In addition, the ability of MKLP1 to bind along scaffold of antiparallel overlaps could depend on the role of PRC1 in dictating 35-nm-inter-microtubule spacing, proposed to be important to enable localization of specific proteins within these structures (Kellogg et al., 2016; Subramanian et al., 2010).

Kif4A and Kif18A are known to regulate microtubule length (Mayr et al., 2007; Varga et al., 2006; Wandke et al., 2012). Thus, we hypothesized that these kinesins may also regulate the length of bridging microtubules and hence their antiparallel overlaps during metaphase. Indeed, removal of Kif4A or Kif18A by siRNA resulted in longer PRC1-labeled overlaps (**Fig. 46 D**). Given that Kif4A and MKLP1 are involved in microtubule sliding within the bridging fiber in anaphase (Vukusic et al., 2019a), our results suggest that Kif4A,

Kif18A, and MKLP1 regulate bridging microtubule dynamics and/or sliding in metaphase, thereby controlling the geometry of their overlaps.

4.13 Kif4A localization on chromosome arms and CLASP1, Kif18A, and CENP-E on kinetochore fiber tips does not depend on PRC1

As an alternative to the changes in the bridging fiber, disruption of polar ejection forces may be the cause of kinetochore misalignment upon PRC1 removal (**Fig. 39 I**), in particular because these forces are modulated by Kif4A (Stumpff et al., 2012). The most prominent Kif4A localization in metaphase is on chromosomes (Gruneberg et al., 2006; Kurasawa et al., 2004; Zhu and Jiang, 2005) (**Fig. 46 B**; **Fig. 47 G,H**). Neither acute nor long-term PRC1 removal had an effect on the Kif4A signal on the chromosomes (**Fig. 46 B,C**; **Fig. 47 I**; **Table 1**). Thus, Kif4A localization on chromosomes does not depend on PRC1, suggesting that the observed changes in kinetochore alignment are not caused by disruption of polar ejection forces. In early anaphase, the amount of Kif4A on segregated chromosomes was similar in opto and control cells (**Fig. 47 J**), indicating that increased occurrence of lagging kinetochores was neither due to perturbed polar ejection forces in that phase nor defects in chromosome architecture/condensation.

Finally, kinetochore misalignment and lagging kinetochores upon PRC1 removal may be due to disrupted localization of proteins that regulate microtubule dynamics at the plus-end of the k-fiber (**Fig. 39 I**). To investigate this possibility, we analyzed the k-fiber localization of the key proteins with this function, CLASP1, Kif18A, and CENP-E (Al-Bassam et al., 2010; Maffini et al., 2009; Maiato et al., 2003; Mayr et al., 2007; Stumpff et al., 2008; Stumpff et al., 2012; Yu et al., 2016). These proteins were localized at the plus-ends of k-fibers before and after acute and long-term removal of PRC1 (**Fig. 46 B,C**; **Table 1**), indicating that kinetochore misalignment upon PRC1 removal is not caused by simultaneous removal of proteins that regulate microtubule dynamics at the k-fiber plus ends.
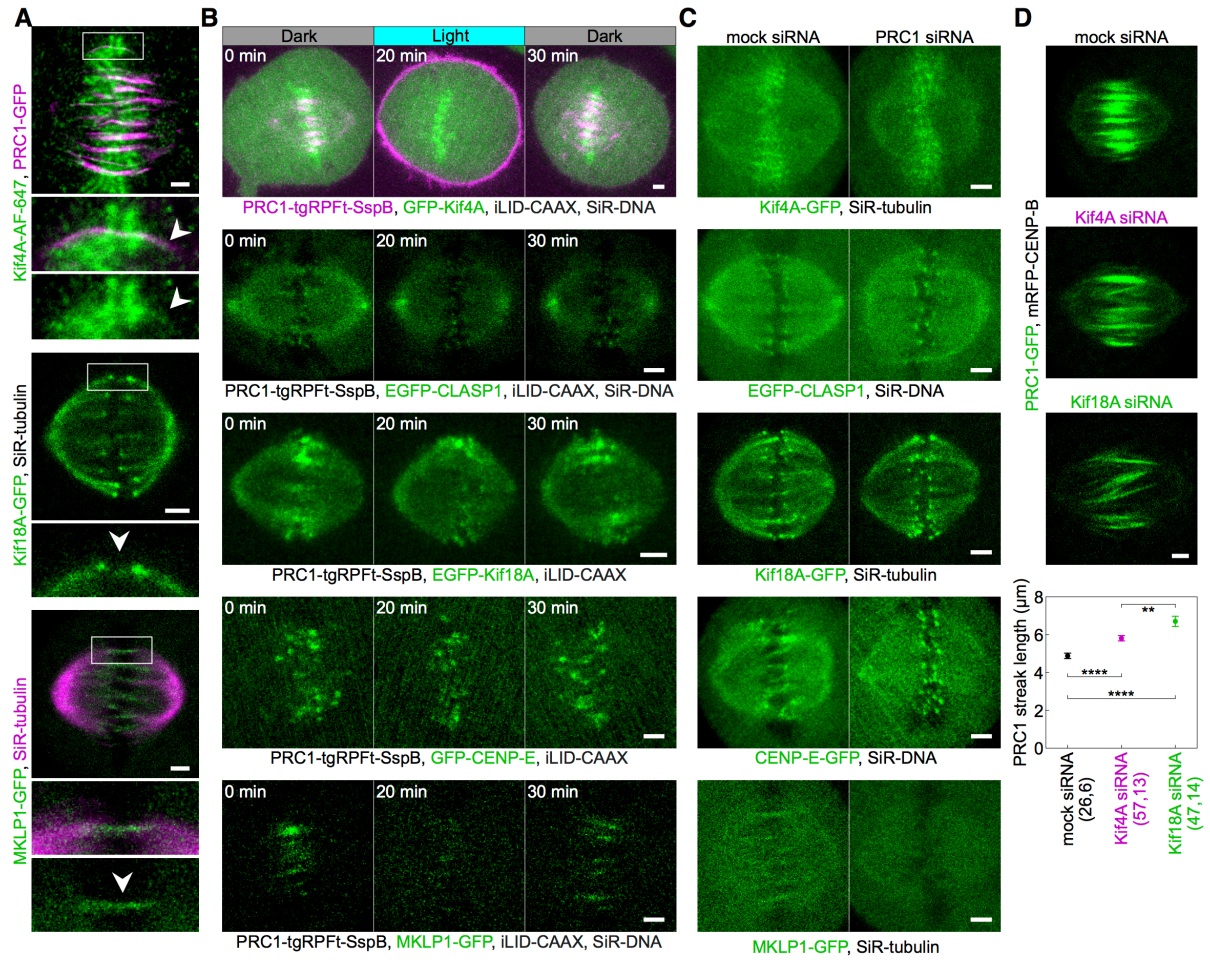
Figure 46. Localization of Kif4A, CLASP1, Kif18A, CENP-E and MKLP1 after acute removal and long-term depletion of PRC1. A. Spindle (top block) in a HeLa cell stably expressing PRC1-GFP (magenta) immunostained for Kif4A-AF-647 (green). Arrows in the enlargements of the boxed region point to Kif4A outside chromosomes, at the positions where PRC1-GFP is found. Spindle (middle block) in a HeLa cell stably expressing Kif18A-GFP (green) and stained for SiR-tubulin (not shown) and spindle (bottom block) in a HeLa cells stably expressing MKLP1-GFP (green) and stained for SiR-tubulin (magenta). Arrows in the enlargements of the boxed regions point to the bridging fiber. **B**. Time-lapse images of: unlabeled U2OS cell with transient expression of opto-PRC1 (magenta), iLID-CAAX and GFP-Kif4A (green), and stained with SiR-DNA (not shown) (first row); HeLa cell with stable expression of EGFP-CLASP1 (green) with transient expression of opto-PRC1 and iLID-CAAX, and stained with SiR-DNA (not shown) (second row); unlabeled U2OS cell with transient expression of opto-PRC1, iLID-CAAX and EGFP-Kif18A (green) (third row); unlabeled U2OS cell with transient expression of opto-PRC1, iLID-CAAX and GFP-CENP-E (green) (fourth row); HeLa BAC cell stably expressing MKLP1-GFP (green) and with transient expression of opto-PRC1 and iLID-CAAX, and stained with SiR-DNA (not shown) (fifth row). All time points are before (0 min, Dark), at the end of continuous exposure (20 min, Light) and 10 min after cessation of exposure to the blue light (30 min, Dark). Note that opto-PRC1 is not shown in order to point out

93

localization of visualized proteins. **C**. Images of mock (left column) and PRC1 siRNA treated (right column): HeLa BAC cell expressing Kif4A-GFP (green) (first row); HeLa cell stably expressing EGFP-CLASP1 (green) (second row); HeLa BAC cell expressing Kif18A-GFP (green) (third row); HeLa BAC cell expressing CENP-E-GFP (green) (fourth row); HeLa BAC cell expressing MKLP1-GFP (green) (fifth row). Cells are stained with SiR-DNA or SiR-tubulin (not shown). **D**. Spindles from HeLa cells stably expressing PRC1-GFP (green), treated with mock (top), Kif4A (middle), and Kif18A (bottom) siRNA. Graph shows the lengths of PRC1 streaks per treatment. Numbers in brackets; number of measurements and cells, respectively. Images in A (bottom), B, and C are maximum intensity projections of 2-3 z-planes, smoothed with 0.5-pixel-sigma Gaussian blur. Scale bars; 2 μm.
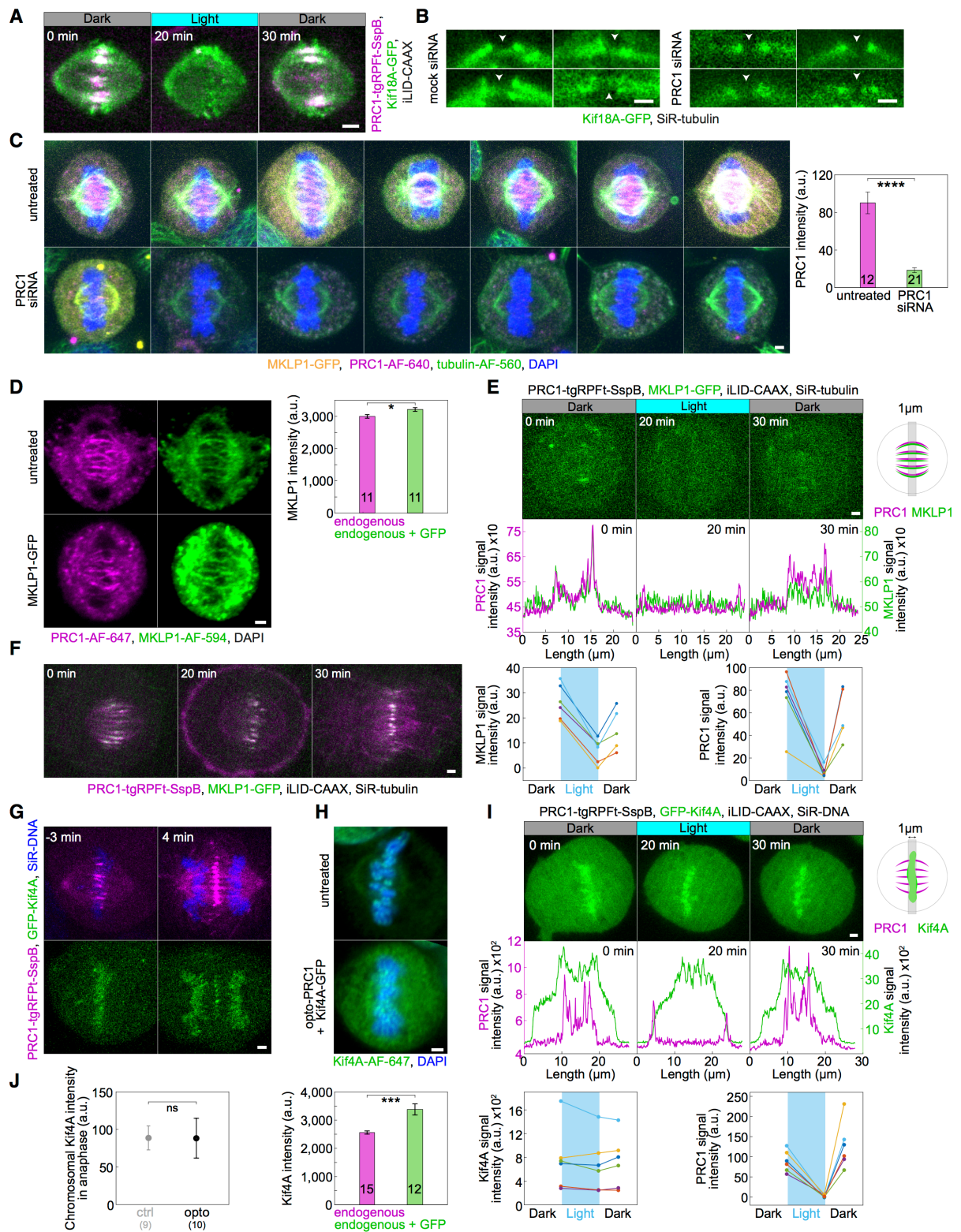
Figure 47. **A**. Time-lapse of unlabeled U2OS cell with transient expression of opto-PRC1 (magenta), iLID-CAAX and EGFP-Kif18A (green) as in Fig. 46 B. Note the co-localization of opto-PRC1 and EGFP-Kif18A in the bridging fibers. **B**. Enlargements of control (left) and PRC1 siRNA treated (right) HeLa BAC cells expressing Kif18A-GFP (green). Note the presence of Kif18A-GFP in the bridging fibers of control cells, and its absence in PRC1 siRNA treated cells (white arrowheads). **C**. Spindles in fixed HeLa cells stably expressing MKLP1-GFP (yellow) and immunostained for PRC1

(AF-640, magenta), tubulin (AF-560, green) and stained with DAPI (blue) in untreated (top) and PRC1 siRNA treated (bottom) cells (left). All images are sum intensity projections of five z-planes. Graph (right) shows PRC1 intensity in untreated (magenta) and PRC1 siRNA treated (green) cells. Numbers inside bars; number of cells. **D**. Spindle in a fixed unlabeled untreated HeLa cell (top left) and HeLa BAC cell expressing MKLP1-GFP (bottom left), immunostained for MKLP1 (AF-594, green), PRC1 (AF-647, magenta) and stained with DAPI (not shown). Images are sum-intensity projections of 5 z-planes smoothed with 0.5-pixel-Gaussian blur. Graph (right) shows MKLP1 intensity in untreated unlabeled (magenta) and BAC cells (green). The signal intensity of MKLP1 in these cells was 6% higher compared to endogenous MKLP1. **E**. Time-lapse of HeLa BAC cell expressing MKLP1-GFP, depleted for endogenous PRC1, with transient expression of opto-PRC1 and iLID-CAAX (only MKLP1-GFP is shown) in time-points as in Fig. 46 B (top). Graphs (middle) correspond to membrane-to-membrane intensity profiles of MKLP1-GFP (green) and opto-PRC1 (magenta) retrieved from the same position perpendicular to the midzone in time-points as in Fig. 46 B, acquired by 1-μm wide line on maximum projection of three z-planes. Schematic representation of performed measurement is given on the right. Graphs (bottom) show individual MKLP1-GFP (left) and opto-PRC1 intensities. **F**. Time-lapse of a cell as in E, which progresses to cytokinesis during time-points as in E. **G**. Time-lapse images of U2OS cells with transient expression of opto-PRC1 (magenta) and GFP-Kif4A (green). Top (merge tgRFPt and SiR-DNA), bottom (GFP). Anaphase onset is set as time 0 min. **H**. Spindle in a fixed untreated unlabeled U2OS cell (top) and unlabeled U2OS cell, depleted for endogenous PRC1 and transiently expressing Kif4A-GFP (not shown) and opto-PRC1 (not shown) (middle), immunostained for Kif4A (AF-647, green) and stained with DAPI (blue). Images are sum-intensity projections of 5 z-planes smoothed with 0.5-pixel-Gaussian blur. Graph (bottom) shows Kif4A intensity in untreated (magenta) and cells with transient expression of Kif4A-GFP (green). The signal intensity of Kif4A in these cells was 30% higher compared to endogenous Kif4A. **I**. Time-lapse of U2OS cell as in Fig. 11 B (only GFP-Kif4A channel) (top). Graphs (middle) correspond to membrane-to-membrane intensity profiles of GFP-Kif4A (green) and opto-PRC1 (magenta) retrieved from the same position perpendicular to the midzone and in time-points as in Fig. 11 B, acquired by 1-μm wide line on a single z-plane. Schematic representation of performed measurement is given on the right. Graphs (bottom) show individual GFP-Kif4A (left) and opto-PRC1 (right) intensities. **J**. GFP-Kif4A intensity on chromosomes in opto (black) and control (gray) cells 4 min after anaphase onset. Anaphase onset is defined as a timeframe of sister chromatid separation. Numbers in brackets; number of cells. Scale bars; 2 μm.

Table 1. Localization of proteins in the bridging fiber and at kinetochores after acute and long-term removal of PRC1. For long-term depletion, p-values for localization in the bridging fiber - Kif4A: 0.043; MKLP1: $8*10^{-6}$; CLASP1: 0.113; Kif18A: 0.033. Statistics: Pearson's Chi-squared test.

In acute removal protein is considered present if at least 83% of cells had it in the bridge and absent if it was undetectable in at least 66% of inspected cells.

Numbers in brackets; number of cells. Legend: + present, - absent, +/- unclear.

*in the case of Kif4A kinetochore (KC) localization includes chromosome arms.

	Acute removal				Long-term depletion			
	Dark (0 min)		Light (20 min)		mock		siRNA	
	Bridge	KC	Bridge	KC	Bridge	KC	Bridge	KC
Kif4A*	+ (6)	+ (6)	+/- (6)	+ (6)	+ (10)	+ (10)	- (16)	+ (16)
CLASP-1	+/- (5)	+ (5)	+/- (5)	+ (5)	+ (15)	+ (15)	+ (8)	+ (8)
Kif18A	+ (6)	+ (6)	- (6)	+ (6)	+ (18)	+ (18)	- (8)	+ (8)
CENP-E	+/- (5)	+ (5)	+/- (5)	+ (5)	+/- (6)	+ (6)	+/- (10)	+ (10)
MKLP-1	+ (6)	- (6)	- (6)	- (6)	+ (19)	- (19)	- (9)	- (9)

4.14 Acute and long-term removal of PRC1 result in partially different effect on spindle microtubules and kinetochores

Previous reports have shown that acute rapamycin-dependent protein translocation and long-term depletion by siRNA can yield different and even opposite phenotypes (Cheeseman et al., 2013; Wordeman et al., 2016). To explore to what extent acute optogenetic removal of PRC1 affects the spindle differently than long-term depletion by siRNA, we compared the phenotypes obtained by these two approaches (**Table 2**). Similarly as acute removal, long-term depletion of PRC1 decreased the number of microtubules in the bridging fiber and caused straightening of outermost k-fibers, whereas spindle length and width was unchanged (**Fig. 48, A-D**). However, the effects of acute removal of PRC1 were more severe than those of siRNA (**Table 2**). Those two methods decreased the inter-kinetochore distance to a similar extent (**Fig. 48 E**), even though unlike acute removal, long-term removal reduced the fraction

of cells that entered anaphase (35 ± 8 % N=37, and 79 ± 6 % N=37, for PRC1 siRNA treated and untreated, respectively; p=0.046, Pearson's Chi-squared test; **Fig. 35 C**). Strikingly, in contrast to acute removal, the long-term depletion did not cause kinetochore misalignment or misorientation (**Fig. 48 F,G**). Moreover, only acute removal resulted in longer antiparallel overlaps within bridging fibers (**Fig. 42; Fig. 43 E**). Finally, both long-term and acute PRC1 reduction increased the frequency of lagging kinetochores during early anaphase (**Fig. 48 H**).

Table 2. Comparison of effects of acute optogenetic removal of PRC1 and long-term depletion by siRNA. All values are given as mean ± s.e.m. The numbers in the brackets denote the number of measurements and cells, respectively; a single number is the number of cells. Symbols (arrows and equal signs) denote trend of change of parameters; equal sign means no change; longer arrow marks stronger effect. Measurements include cells without and with SiR-tubulin.

*calculated from our previous study (Polak et al., 2017)

#consistent with our previous studies (Kajtez et al., 2016; Polak et al., 2017)

Parameter	Acute removal (opto)				Long-term depletion (siRNA)			
	0 min	20 min	p-value		untreated	siRNA	p-value	
d_{EQ} (μm)	0.78 ± 0.04 (290, 17)	0.94 ± 0.05 (240, 16)	0.035	↑	0.69 ± 0.05 (107, 8)	0.69 ± 0.03 (333, 17)	0.64	=
d_{EQ} >2 μm (%)	4.1 ± 1.2 (290, 17)	8.3 ± 1.8 (240, 16)	0.043	↑	3.3 ± 1.0 (107, 8)	0.9 ± 0.9 (333, 17)	0.33	=
d_{KC} (μm)	0.87 ± 0.01 (226, 18)	0.79 ± 0.01 (186, 18)	$1*10^{-8}$	↓	0.85 ± 0.01 (75, 8)#	0.780 ± 0.008 (202, 17)#	$4*10^{-6}$	↓
α_{KC}	13.8 ± 0.7 (290, 17)	18.4 ± 1.0 (240, 16)	0.0013	↑	13.3 ± 1.0 (107, 8)	10.3 ± 0.7 (333, 17)	$1*10^{-4}$	↓
α_{KC} >35° (%)	6.2 ± 1.4 (290, 17)	12.1 ± 2.1 (240, 16)	0.018	↑	4.7 ± 2.0 (107, 8)	3.6 ± 1.0 (333, 17)	0.83	=
N (microtubules) in the bridging fiber	14 ± 2 (22, 13)	5.6 ± 0.9 (19, 10)	0.0038	↓	14 ± 1 (16, 9)*	10 ± 1 (21, 6)*	0.048	↓
Curvature (μm^{-1})	0.134 ± 0.004 (40, 10)	0.081 ± 0.005 (39, 10)	$6*10^{-11}$	↓	0.137 ± 0.006 (20, 5)	0.108 ± 0.004 (52, 13)	0.0014	↓
θ (°)	142 ± 3 (20, 10)	125 ± 3 (20, 10)	$2*10^{-4}$	↓	145 ± 3 (10, 5)	137 ± 2 (26, 13)	0.051	=
Lagging kinetochores (%)	23 ± 7 (39) control	46 ± 9 (28) opto	0.044	↑	5 ± 4 (37)	40 ± 11 (20)	0.0036	↑
Half-overlap length (μm)	1.8 ± 0.1 (17, 9) control	2.6 ± 0.2 (23, 9) opto	0.009	↑	2.0 ± 0.2 (16, 6)	1.8 ± 0.2 (14, 4)	0.45	=
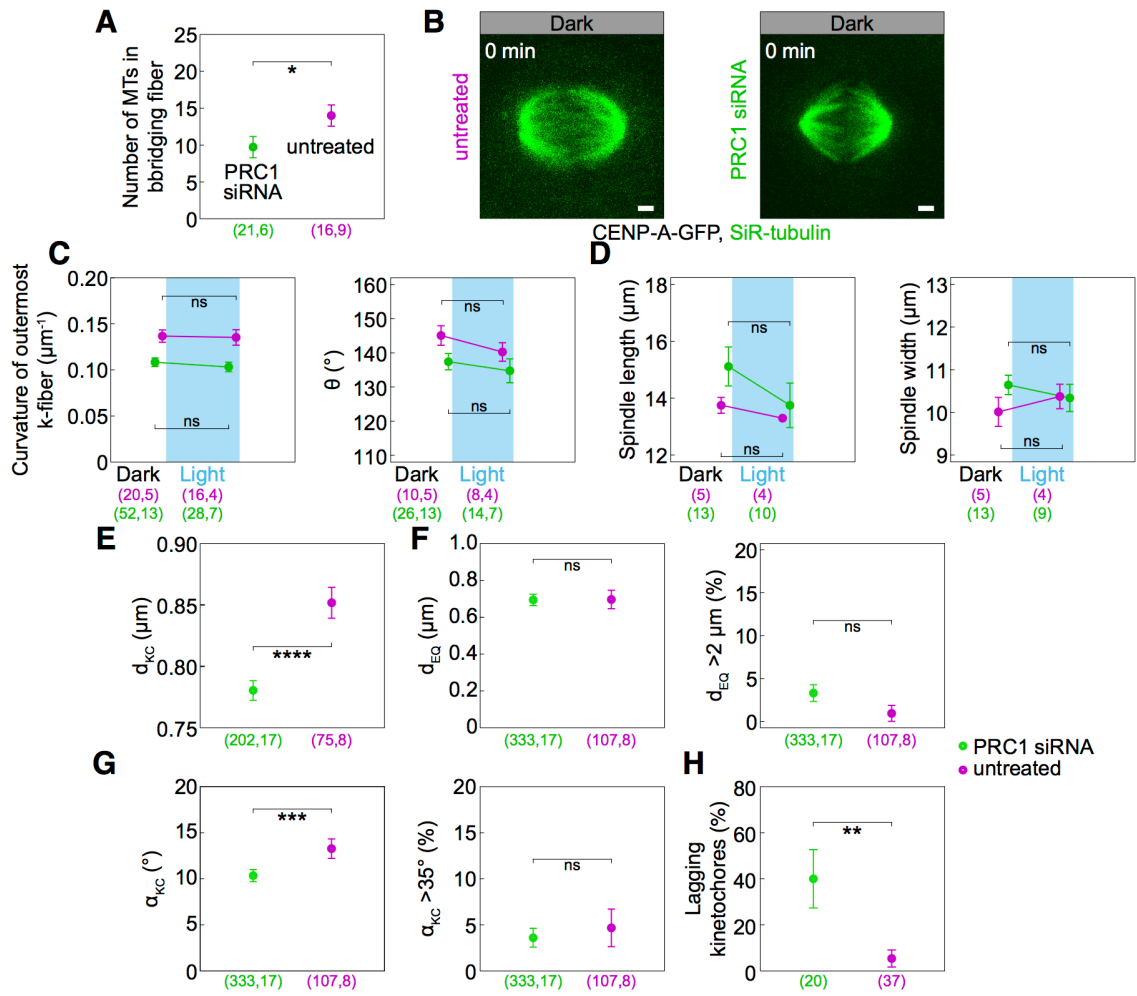
Figure 48. A. Number of microtubules in the bridging fiber in untreated (magenta) and PRC1 siRNA treated HeLa cells (green) retrieved from our previous study (Polak et al., 2017). **B**. Spindles of untreated (left) and PRC1 siRNA treated U2OS cells with stable expression of CENP-A-GFP (not shown) and stained with SiR-tubulin (green). **C.** Curvature (left) and θ, angle between (right) the outermost k-fibers in cells as in B, untreated (magenta) or PRC1 siRNA treated (green), before (0 min, Dark) and at the end of continuous exposure to the blue light (20 min, Light). **D.** Spindle length (left) and width (right) in cells as in B. **E**. Measurements of dKC in untreated (magenta) and PRC1 siRNA treated (green) U2OS cells with stable expression of CENP-A-GFP and stained with SiR-tubulin. **F.** Measurements of dEQ in cells as in B (left) and percentage of dEQ greater than 2 μm in untreated (magenta) and PRC1 siRNA treated (green) cells. **G**. Measurements of αKC in cells as in B (left) and percentage of αKC greater than 35° in untreated (magenta) and PRC1 siRNA treated (green) cells. **H.** Occurrence of lagging kinetochores in anaphase of untreated (magenta) or PRC1 siRNA treated (green) U2OS cells with stable expression of CENP-A-GFP and stained with SiR-tubulin.

Cyan rectangles inside graphs indicate exposure to the blue light. Numbers in brackets denote measurements and cells; single numbers denote cells. Scale bars: 2 μm. Statistical analysis; t-test (A,
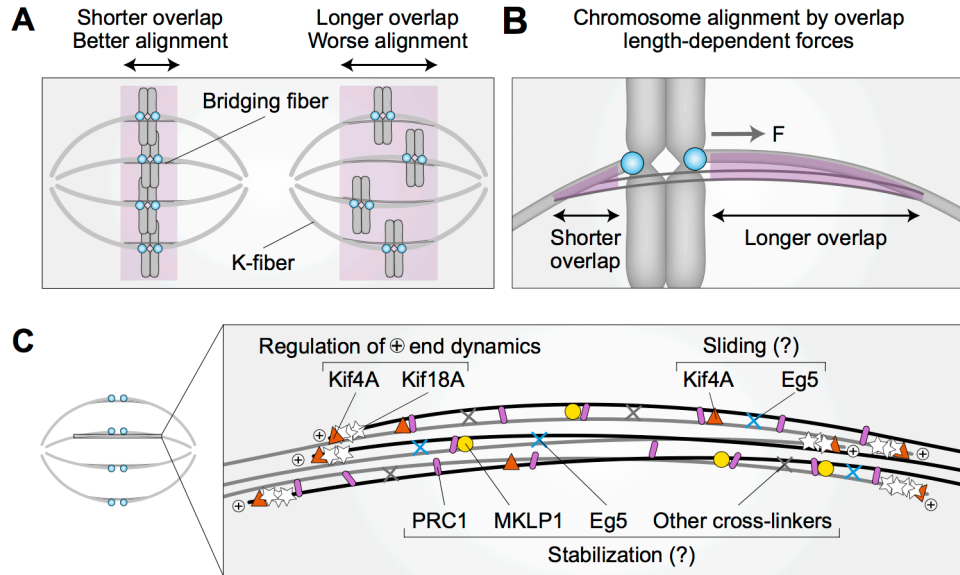
Figure 49. Model for chromosome alignment by overlap length-dependent forces within the bridging fiber. A. We propose that the interactions between k-fibers and bridging fibers regulate the movement of bi-oriented chromosomes by forces that depend on the length of the antiparallel overlaps (purple). Shorter overlaps lead to more precise alignment of kinetochores (cyan) than longer ones. **B.** If a kinetochore pair is displaced away from the equatorial plane towards one pole, the overlap between the k-fiber and the bridging fiber (purple) is shorter on this side and longer on the opposite side. More motors and/or crosslinkers accumulate in the longer overlap, pulling the kinetochore back to the center (F, pulling force). The efficiency of centering depends on the relative asymmetry in the overlap length on either side. This asymmetry is larger if the overlap is short, which explains why short overlaps lead to better alignment than long ones (see A). **C**. The overlap length is regulated by Kif4A and Kif18A at the plus ends of bridging microtubules. Kif4A and Eg5 within the bridging fiber possibly slide the microtubules apart, whereas PRC1 stabilizes the overlaps probably together with MKLP1, Eg5, and other crosslinkers.

5. CONCLUDING DISCUSSION

5.1 Kif18A strongly affects chromosome alignment in RPE-1 cells

Chromosomes in vertebrate cells exhibit oscillatory movements around spindle equator during metaphase, and regulation of these movements is believed to be involved in establishment and maintenance of alignment (Kapoor and Compton, 2002; Skibbens et al., 1993). Kinesin-8 was shown to regulate both microtubule growth and shrinkage *in vitro* (Erent et al., 2012; Mayr et al., 2007; Varga et al., 2006) and affect kinetochore movements *in vivo* (Garcia et al., 2002; Mayr et al., 2007; Stumpff et al., 2008).

In line with previous studies in HeLa cell line (Mayr et al., 2007; Stumpff et al., 2008), Kif18A depletion in RPE-1 cells caused stronger kinetochore oscillations reflected as the increase of the mean positions of kinetochore pairs from the equatorial plate, whereas elevated levels caused dampening of kinetochore oscillations. More detailed analysis of kinetochore movements in control and Kif18A siRNA treated cells revealed that Kif18A regulates kinetochore movements and alignment in RPE-1 cells by affecting kinetochore velocity and rates of directional switches, similarly as in HeLa cells (Stumpff et al., 2008), implying that Kif18A could have a similar mode of action in transformed and non-transformed human cell lines. Depletion of Kif18A increased velocity, but decreased switch rates of kinetochore pairs that led to prolonged movement of kinetochores before switch in direction, which generated excursions of kinetochores further from the equatorial plate compared to control cells.

5.2 Kif18A generates length- dependent pulling forces

The role of Kif18A in force generation at kinetochores was explored by laser cutting experiments in cells with altered amount of Kif18A. In both control and Kif18 siRNA treated cells laser cutting on the trailing (AP moving) side did not change the direction of movement of ablated pair, while cuts on the leading side (P moving) induced directional switch of ablated pair toward pole on the unablated side of the spindle. Similar behavior was reported for cuts between sister kinetochores where one that moved poleward (P) continued its movement in the same direction, while AP moving one stopped and changed its direction (Khodjakov and Rieder, 1996; Maiato et al., 2004a). These results indicate that there is no

substantial pushing force on the trailing side of the moving kinetochore pair, where the pulling on the leading side seems to be dominant in determining kinetochore direction. This is futher supported by a more recent study of intrakinetochore dynamics during directed motion in PtK$_1$ cells by labeling inner-and outer-kinetochore components, where P kinetochore is revealed to be compressed relative to AP kinetochore, consistent with force being generated at P kinetochore and AP kinetochore forming rather passive attachment to microtubules (Dumont et al., 2012).

Interestingly, in control cells there was a short delay up to 7 s before P moving kinetochores switched to AP movement, possibly representing the time required for accumulation of Kif18A to a sufficient level on k-fiber plus-end to stop microtubule growth or cause microtubule depolymerization (Du et al., 2010; Varga et al., 2006). This delay time was longer in cells with depleted Kif18A (~26 s). In these cells there is possibly some residual amount of Kif18A that is not silenced and therefore, more time is required for its accumulation on plus-end before affecting dynamics of k-fiber microtubules, or alternatively, catastrophe is induced stochastically, without influence of motors.

Taken together, these results support the model in which regulation of k-fiber dynamics is achieved through length-dependent accumulation of Kif18A also in human cells. In this model, growing microtubules in the k-fiber would accumulate more Kif18A motors that subsequently induce their swich to depolymerisation thus pulling the kinetochore attached to k-fiber, similar to proposed mechanism in yeast cells (Mary et al., 2015; Tischer et al., 2009; Varga et al., 2006). Depolymerising k-fiber would also exert pulling force on its sister k-fiber, thereby inducing polymerisation of the trailing fiber, probably through force dependent rescue that was previously proposed to promote microtubule growth in yeast cells (Gardner et al., 2005; Klemm et al., 2018; Sprague et al., 2003) and is already used in models for higher eukaryotic cells (Armond et al., 2015; Civelekoglu-Scholey et al., 2013).

5.3 An optogenetic system for acute, selective, and reversible removal of spindle proteins

Since mitosis is a fast and dynamic process, studies of the function of spindle proteins require methods that allow precise manipulation of proteins inside cells. For this reason, an optogenetic approach was developed here that allows acute light-controlled removal of proteins from a normally formed spindles at a precise phase of mitosis. The main advantage of this approach over similar chemically-induced protein translocation (Cheeseman et al.,

2013; Haruki et al., 2008; Robinson et al., 2010; Wordeman et al., 2016) are its reversibility, allowing the protein to return to its initial location within about a minute, and applicability to individual cells. Unlike previous optogenetic approaches (Fielmich et al., 2018; Okumura et al., 2018; van Haren et al., 2018; Yang et al., 2013; Zhang et al., 2017), this method allows for global loss-of-function of full-length spindle proteins, relying on simple protein tagging rather than domain splitting, with no need of chromophore addition. Moreover, we recently demonstrated how this method can be easily implemented with other optical perturbations, thus providing a powerful tool for studying mitotic spindle dynamics (Milas et al., 2018). Finally, an optogenetic approach developed here could also serve as an '*in vivo* pull-down' assay for probing protein-protein interactions in different phases of the cell cycle. However, it needs to be pointed out that this approach depends on the affinity and turnover of the protein in comparison with the time scale of interest.

In experiments performed here, there were some differences in phenotypes upon acute PRC1 removal from the spindle by optogenetics and the long-term depletion by siRNA. Similar observations of somewhat different phenotypes upon acute and long-term removal of proteins were reported before (Cheeseman et al., 2013; Wordeman et al., 2016). The observed differences are hard to explain by different levels of PRC1 on the spindle as both methods decreased PRC1 by ~90%. It is also unlikely that the differences are caused by the interaction of the membrane-translocated PRC1 with astral microtubules because of the uniform PRC1 signal on the membrane, fast return to the spindle, and no change in spindle positioning. Therefore, the generally weaker effects of siRNA in comparison with the acute optogenetic removal are most likely due to compensatory mechanisms being triggered during long-term depletion. At this point these mechanisms remain elusive, but probably rely on different behavior of yet unknown protein(s) between these two approaches in the terms of their removal together with PRC1 in one case, but not the other, or alternatively, on upregulation of expression of certain protein(s) during long-term depletion by siRNA. However, this still needs to be explored.

5.4 PRC1 dynamics decreases from metaphase to anaphase

Optogenetic removal of PRC1 gave an information regarding PRC1 dynamics and turnover in metaphase and anaphase, as it could not be completely removed in cells that entered anaphase compared to those that remained in metaphase during exposure to the blue light. We further

tested this by FRAP analaysis which revealed high turnover rate of PRC1 in human cells similar to the turnover of a plant ortholog MAP65 (Chang et al., 2005; Smertenko et al., 2008) and faster than the turnover of yeast ortholog Ase1, which recovers during anaphase in ~7.5 min in budding yeast (Schuyler et al., 2003) and in ~7 min in fission yeast (Loiodice et al., 2005). These differences could be due to the multimerization of Ase1, a feature not observed for PRC1 (Kapitein et al., 2008). Also, these differences in turnover rates between fungi and higher eucaryotes could be explained by differences in their spindle architectures. As spindle midzone in fungi consists of only very few microtubules (Ding et al., 1993; Winey et al., 1995), the limited number of Ase1 molecules has to associate to microtubules more tightly in order to preserve stability of the midzone architecture. On the other hand, spindles of higher eucaryotes are far more complex, with midozne consisiting of hundreds of antiparallel microtubules (Mastronarde et al., 1993; McIntosh and Landis, 1971; O'Toole et al., 2020), where weaker interactions might be more beneficial to prevent excessive microtubule crosslinking.

FRAP analysis also revealed differences in immobile fraction of PRC1 between metaphase and anaphase, which indicates a larger fraction of dephosporylated PRC1, which bundles MTs, is present in the overlaps, corresponding to the observed decrease in levels of phosphorylated PRC1 when cells enter anaphase (Zhu and Jiang, 2005). Moreover, we speculate that fast turnover of PRC1, both in metaphase and anaphase, suggests that predominantly, PRC1 is randomly added and replaced in MT overlaps, not translocated toward plus ends, as previous experiments demonstrated that single PRC1 molecules can maintain associations with the MT lattice with a lifetime of ~ 3.5 s (Forth et al., 2014). It was proposed that PRC1 crosslinks are compliant to microtubule sliding driven by Eg5/kinesin-5 (Subramanian et al., 2010), this high dynamics could be critical to permit MT sliding while maintaining MT stability in the spindle midzone.

5.5 A model for chromosome alignment by overlap length-dependent forces within the bridging fibers

By overcoming temporal limitations of siRNA, this work revealed an unexpected role of PRC1 and bridging fibers in the regulation of chromosome alignment on the metaphase spindle via overlap length-dependent forces (**Fig. 49**). We propose that the interactions between k-fibers and bridging fibers regulate the movement of bi-oriented chromosomes

along the pole-to-pole axis. If a kinetochore pair is displaced towards one spindle pole, more motors and/or crosslinkers are expected to accumulate in the overlap facing the opposite pole because this overlap is longer, and pull the kinetochores back to the center (**Fig. 49 B**). As the efficiency of this type of centering depends on the relative asymmetry in the overlap length on either side, shorter overlap length leads to more precise centering of the kinetochores (**Fig. 49 A,B**).

The finding that acute PRC1 removal leads to chromosome misalignment and elongation of overlap zones supports this model. Moreover, elongation of overlaps correlates with chromosome misalignment within spindles, as elongated overlaps and misaligned chromosomes are mostly found in the central part of the spindle rather than on the periphery. In contrast to the acute PRC1 removal, long-term PRC1 depletion by siRNA leads neither to overlap elongation nor chromosome misalignment, providing further support to our model. These differences between the acute and long-term depletion give an indication on the nature of abovementioned compensatory mechanism that probably operates through regulation of overlap length and hence maintain chromosome alignment during long-term PRC1 depletion.

How is the length of the bridging microtubules and their overlaps controlled?

Interestingly, we found that Kif4A, Kif18A, and MKLP1 localize in the bridging fibers in metaphase and this localization was lost after optogenetic or siRNA-mediated PRC1 removal. The observation of Kif4A and Kif18A being localized in the bridging fibers is surprising as their localization and therefore function within metaphase spindles is thought to be restricted exclusively to chromosome arms and plus-ends of k-fibers, respectively (Kurasawa et al., 2004; Mayr et al., 2007; Mazumdar et al., 2004; Stumpff et al., 2008). As both Kif4A and Kif18A promote microtubule depolymerization (Bieling et al., 2010b; Bringmann et al., 2004; Mayr et al., 2007; Stumpff et al., 2008; Stumpff et al., 2012; Varga et al., 2006) and our experiments showed that depletion of either of them by siRNA leads to longer PRC1-labeled overlaps, the loss of these kinesins from the bridge upon acute PRC1 removal may underlie the observed increase in length of the bridging microtubules. These elongated PRC1-labeled overlaps provide another line of evidence in support of our model for chromosome alignment by overlap length-dependent forces, as Kif4A and Kif18A siRNA-treated cells exhibit chromosome misalignment (Stumpff et al., 2008; Wandke et al., 2012). Even though it was reported that Kif4A does not directly interact with PRC1 before late mitosis (Gruneberg et al., 2006; Kurasawa et al., 2004; Zhu and Jiang, 2005) there may be a small pool of Kif4A that

does so and binds to the antiparallel overlaps of bridging microtubules in metaphase. PRC1 removal likely results in the removal of this pool of Kif4A from the bridge, which may lead to excessive microtubule polymerization and thus longer overlap zones in metaphase, similar to the long overlaps in anaphase after Kif4A depletion (Hu et al., 2011; Voets et al., 2015). Kif18A, which is known to accumulate at microtubule plus-ends where it promotes depolymerization (Gupta et al., 2006; Mayr et al., 2007; Stumpff et al., 2008; Varga et al., 2006), likely also regulates bridging microtubule length in this manner. However, as Kif18A is not a binding partner of PRC1, it is possible that it remains in the bridge after PRC1 removal, but its signal may be undetectable due to the smaller number of microtubules in the bridge and the fact that their plus ends are positioned away from the equator, thus overlapping with the Kif18A signal along the k-fiber. We propose that both Kif4A and Kif18A regulate the length of bridging microtubules and their overlaps (**Fig. 49 C**), with Kif4A likely being more accountable for overlap elongation upon acute PRC1 removal. However, at this point it is impossible to say with apsolute certainty wheather the removal of either Kif4A or Kif18A or both accounts for overlap elongation and chromosome misalignment observed after acute removal of PRC1.

To clearly discriminate between their contributions, additional expriments could be performed, where PRC1 would be acutely removed by optogenetics, but with simultaneous depletion by siRNA of either Kif4A or Kif18A. The outcomes of these two groups of experiments regarding chromosome alignment would give an insight whether Kif4A or Kif18A is responsible for phenotype in acute removal of PRC1. So, for example, if in cells with siRNA depleted Kif18A acute removal of PRC1 would lead to worse chromosome alignment compared as it was at the beginning of the experimet before PRC1 removal, this would imply that Kif4A in the bridge accounts for overlap elongation and misaligment, since it is removed from the bridge together with PRC1. If the alignment would stay the same before and after PRC1 removal, it could be concluded that Kif18A is an underlying mechanism. Analogous logic could be applied for cells in other group of experiments where Kif4A would be depleted by siRNA prior to acute removal of PRC1. Worsened chromosome alignment would imply involvement of Kif18A, and the same would mean Kif4A is responsible for overlap length regulation and chromosome alignment.

It is important to point out here that both Kif4A and Kif18A were lost from the bridge in both acute removal and long-term depletion of PRC1 by siRNA. This however does not exclude the possibily that removal of Kif18A and/or Kif4A from the bridge accounts for overlap length elongation and chromosome misalignment in acute approach as the underlying

compensatory mecahnism in siRNA treated cells could be an upregulated expression of an additional protein involved in regulation of microtubule dynamics/stabilisation which could ultimately mask the true phenotype and prevent overlap elongation that is observed after acute removal of PRC1.

The proteins that we found in the bridging fiber, Kif4A, Kif18A, and MKLP1, may also slide apart and/or stabilize the bridging microtubules (**Fig. 49 C**). We also observed Eg5 in the bridging fiber (Kajtez et al., 2016; Mann and Wadsworth, 2018), though its localization was independent of PRC1 in contrast to the other kinesins that we tested. During early anaphase, Kif4A and Eg5 drive the sliding of antiparallel microtubules that elongates the spindle (Vukusic et al., 2019a). Thus, these kinesins may have a similar role during metaphase. This possibility is in agreement with previous work showing that Kif4A depletion reduces microtubule poleward flux in metaphase (Wandke et al., 2012). Similarly, Kif18A in the bridging fiber may have microtubule sliding and crosslinking activities equivalent to those of the yeast kinesin-8 (Su et al., 2013). Furthermore, MKLP1 contributes to the stabilization of bridging microtubules in early anaphase (Vukusic et al., 2017), and we suggest that it performs a similar function in metaphase together with other motors and crosslinkers including Eg5 and PRC1. The roles of these and other proteins within bridging fibers in the regulation of microtubule dynamics and sliding will be an intriguing topic for future studies.

The localization of Kif4A on chromosome arms, where it is involved in polar ejection forces (Bieling et al., 2010a; Brouhard and Hunt, 2005) was unaffected by acute PRC1 removal. Similarly, CLASP1, Kif18A, and CENP-E remained on plus-ends of k-fibers. Although we cannot exclude potential subtle changes in the localization of these proteins or mislocalization of other proteins, our results suggest that the perturbed kinetochore alignment is unlikely due to reduced polar ejection forces or perturbed k-fiber plus ends.

The changes upon acute PRC1 removal were not spatially uniform across the spindle. The most affected part was the inner part of the spindle, where the PRC1 signal disappeared faster and the bridging microtubules became longer than on the periphery of the spindle. The inner bridging fibers were more severely affected by PRC1 removal possibly because they are made up of fewer microtubules than the outer bridges. Severely misaligned kinetochores that moved more than 2 μm away from the equatorial plane and lagging kinetochores occurred also more often in the inner part of the spindle. This local effect is in line with weak mechanical coupling between neighboring k-fibers yet strong coupling between sister k-fibers (Elting et al., 2017; Suresh et al., 2020; Vladimirou et al., 2013), and indicative of a mechanistic link between the bridging fiber geometry and kinetochore alignment.

Finally, we propose that overlap length-dependent forces help to position the chromosomes at the equatorial plane of the spindle. The overlap length is regulated by Kif4A and Kif18A within the bridging fiber. Kif4A, Eg5, and possibly other kinesins may slide bridging microtubules apart, whereas PRC1 together with the kinesins stabilizes the overlaps. Thus, in addition to the forces generated at k-fiber tips and polar ejection forces, proper chromosome alignment requires forces generated within the bridging fiber, which are transferred to the k-fiber and rely on precise regulation of the overlap region.

6. CONCLUSION

Before chromosome segregation in anaphase, chromosomes congress to the spindle equator, aligning at the position equidistant from both spindle poles (Walczak et al., 2010). Establishment of proper kinetochore-microtubule attachments, monitored by spindle assembly checkpoint (Musacchio and Salmon, 2007) and the alignment of chromosomes at the spindle equator are a prerequisite for synchronous movement of chromosomes in anaphase, and therefore chromosome inheritance fidelity (Cimini, 2008; Maiato et al., 2017; Walczak et al., 2010), which makes understanding of precise mechanisms involved in congression and maintenance of chromosome alignment extremely important.

Chromosome alignment at the equator is generally thought to depend on two main mechanisms, based on length-dependent pulling and polar ejection forces. Length-dependent pulling forces are exerted by k-fiber tips and are thought to be regulated mostly by kinesin-8 motor proteins. These motors have the ability to move towards plus-ends of microtubules where they promote depolymerization in a length-dependent manner (Gupta et al., 2006; Tischer et al., 2009; Varga et al., 2006; Varga et al., 2009) and were also shown to be required for proper kinetochore alignment in various organisms from yeast to humans (Garcia et al., 2002; Stumpff et al., 2008; Wargacki et al., 2010). In addition to the forces produced by k-fibers, polar ejection forces push chromosome arms away from the pole, powered by arm-bound chromokinesins that walk towards the plus end of microtubules (Bajer et al., 1982; Brouhard and Hunt, 2005).

K-fibers are surrounded by a dense network of spindle microtubules with which they have multiple interactions (McDonald et al., 1992; O'Toole et al., 2020), resulting in forces acting on k-fibers and thus also on kinetochores. In particular, each pair of sister k-fibers is tightly linked by the bridging fiber, a bundle of antiparallel microtubules that

balances the tension on sister kinetochores (Kajtez et al., 2016; Polak et al., 2017; Vukusic et al., 2017). However, the role of forces exerted by bridging fiber in chromosome alignment at the metaphase plate was unknown. In metaphase, overlap regions within bridging fibers are crosslinked by PRC1 (Kajtez et al., 2016; Polak et al., 2017; Tolic, 2018), a non-motor microtubule-associated protein that selectively bundles antiparallel microtubules and provides stable overlaps *in vitro* (Bieling et al., 2010b; Janson et al., 2007; Mollinari et al., 2002; Subramanian et al., 2010).

In this work, an optogenetic approach was developed and applied for acute and reversible removal of PRC1 from the spindle to the cell membrane, building upon ideas of dimerization or dissociation induced chemically (Cheeseman et al., 2013; Haruki et al., 2008; Robinson et al., 2010; Wordeman et al., 2016) or by light (Fielmich et al., 2018; Guntas et al., 2015; Okumura et al., 2018; van Haren et al., 2018; Yang et al., 2013; Zhang et al., 2017) to rapidly redistribute proteins. By using this assay on metaphase spindles, we found that bridging fibers promote kinetochore alignment. PRC1 removal resulted in partial disassembly of bridging fibers and elongation of their overlap zones. Kif4A/kinesin-4 and Kif18A/kinesin-8 were found to localize in the bridging fiber during metaphase and were lost upon PRC1 removal. These results, together with the finding that Kif4A or Kif18A depletion by siRNA led to elongated overlaps, suggest that these proteins regulate the overlap length of bridging microtubules. These discoveries are paradigm shifting since Kif4A and Kif18A were generally thougt to localize and exert their functions on chromosome arms and at plus-ends of k-fibers in metaphase, respectively (Kurasawa et al., 2004; Mazumdar et al., 2004; Stumpff et al., 2008). In particular, laser ablation experiments showed Kif18A promotes alignment by generation of length-dependent pulling forces on plus-ends of k-fibers, and optogenetic experiments suggest it could regulate dynamics of microtubules in the bridge also. These discoveries will certainly motivate further reaseach with the aim to precisely explore functions of these motors in the bridging fibers separately from their functions on other locations within the spindle.

7. BIBLIOGRAPHY

Afonso, O., I. Matos, and H. Maiato. 2014. Spatial control of the anaphase-telophase transition. *Cell Cycle*. 13:2985-2986.

Agrawal, N., P.V. Dasaradhi, A. Mohmmed, P. Malhotra, R.K. Bhatnagar, and S.K. Mukherjee. 2003. RNA interference: biology, mechanism, and applications. *Microbiology and molecular biology reviews : MMBR*. 67:657-685.

Aist, J.R., H. Liang, and M.W. Berns. 1993. Astral and spindle forces in PtK2 cells during anaphase B: a laser microbeam study. *J Cell Sci*. 104 (Pt 4):1207-1216.

Akhmanova, A., and M.O. Steinmetz. 2008. Tracking the ends: a dynamic protein network controls the fate of microtubule tips. *Nat Rev Mol Cell Biol*. 9:309-322.

Al-Bassam, J., H. Kim, G. Brouhard, A. van Oijen, S.C. Harrison, and F. Chang. 2010. CLASP promotes microtubule rescue by recruiting tubulin dimers to the microtubule. *Dev. Cell*. 19:245-258.

Alberts, B., A. Johnson, J. Lewis, D. Morgan, M. Raff, and K. Roberts. 2017. Molecular biology of the cell. Garland Science.

Andrews, P.D., Y. Ovechkina, N. Morrice, M. Wagenbach, K. Duncan, L. Wordeman, and J.R. Swedlow. 2004. Aurora B regulates MCAK at the mitotic centromere. *Dev Cell*. 6:253-268.

Antonio, C., I. Ferby, H. Wilhelm, M. Jones, E. Karsenti, A.R. Nebreda, and I. Vernos. 2000. Xkid, a chromokinesin required for chromosome alignment on the metaphase plate. *Cell*. 102:425-435.

Armond, J.W., E.F. Harry, A.D. McAinsh, and N.J. Burroughs. 2015. Inferring the Forces Controlling Metaphase Kinetochore Oscillations by Reverse Engineering System Dynamics. *PLoS Comput. Biol.* 11:e1004607.

Auckland, P., and A.D. McAinsh. 2015. Building an integrated model of chromosome congression. *J Cell Sci*. 128:3363-3374.

Bajer, A.S., C. Cypher, J. Mole-Bajer, and H.M. Howard. 1982. Taxol-induced anaphase reversal: evidence that elongating microtubules can exert a pushing force in living cells. *Proc Natl Acad Sci U S A*. 79:6569-6573.

Barisic, M., P. Aguiar, S. Geley, and H. Maiato. 2014. Kinetochore motors drive congression of peripheral polar chromosomes by overcoming random arm-ejection forces. *Nat Cell Biol*. 16:1249-1256.

Bence, M., F. Jankovics, T. Lukacsovich, and M. Erdelyi. 2017. Combining the auxin-inducible degradation system with CRISPR/Cas9-based genome editing for the conditional depletion of endogenous Drosophila melanogaster proteins. *The FEBS journal*. 284:1056-1069.

Bieling, P., I. Kronja, and T. Surrey. 2010a. Microtubule motility on reconstituted meiotic chromatin. *Curr Biol*. 20:763-769.

Bieling, P., I.A. Telley, and T. Surrey. 2010b. A minimal midzone protein module controls formation and length of antiparallel microtubule overlaps. *Cell*. 142:420-432.

Boyden, E.S., F. Zhang, E. Bamberg, G. Nagel, and K. Deisseroth. 2005. Millisecond-timescale, genetically targeted optical control of neural activity. *Nature neuroscience*. 8:1263-1268.

Braun, M., Z. Lansky, G. Fink, F. Ruhnow, S. Diez, and M.E. Janson. 2011. Adaptive braking by Ase1 prevents overlapping microtubules from sliding completely apart. *Nat Cell Biol*. 13:1259-1264.

Bringmann, H., G. Skiniotis, A. Spilker, S. Kandels-Lewis, I. Vernos, and T. Surrey. 2004. A kinesin-like motor inhibits microtubule dynamic instability. *Science*. 303:1519-1522.

Brinkley, B.R., and J. Cartwright, Jr. 1975. Cold-labile and cold-stable microtubules in the mitotic spindle of mammalian cells. *Annals of the New York Academy of Sciences*. 253:428-439.

Brouhard, G.J., and A.J. Hunt. 2005. Microtubule movements on the arms of mitotic chromosomes: polar ejection forces quantified in vitro. *Proc Natl Acad Sci U S A*. 102:13903-13908.

Brust-Mascher, I., P. Sommi, D.K. Cheerambathur, and J.M. Scholey. 2009. Kinesin-5-dependent poleward flux and spindle length control in Drosophila embryo mitosis. *Mol Biol Cell*. 20:1749-1762.

Buda, R., K. Vukusic, and I.M. Tolic. 2017. Dissection and characterization of microtubule bundles in the mitotic spindle using femtosecond laser ablation. *Methods Cell Biol*. 139:81-101.

Cameron, L.A., G. Yang, D. Cimini, J.C. Canman, O. Kisurina-Evgenieva, A. Khodjakov, G. Danuser, and E.D. Salmon. 2006. Kinesin 5-independent poleward flux of kinetochore microtubules in PtK1 cells. *J Cell Biol*. 173:173-179.

Cane, S., A.A. Ye, S.J. Luks-Morgan, and T.J. Maresca. 2013. Elevated polar ejection forces stabilize kinetochore-microtubule attachments. *J Cell Biol*. 200:203-218.

Canman, J.C., E.D. Salmon, and G. Fang. 2002. Inducing precocious anaphase in cultured mammalian cells. *Cell Motil Cytoskeleton*. 52:61-65.

Caplen, N.J., S. Parrish, F. Imani, A. Fire, and R.A. Morgan. 2001. Specific inhibition of gene expression by small double-stranded RNAs in invertebrate and vertebrate systems. *Proc Natl Acad Sci U S A*. 98:9742-9747.

Cassimeris, L.U., R.A. Walker, N.K. Pryer, and E.D. Salmon. 1987. Dynamic instability of microtubules. *Bioessays*. 7:149-154.

Chang, H.Y., A.P. Smertenko, H. Igarashi, D.P. Dixon, and P.J. Hussey. 2005. Dynamic interaction of NtMAP65-1a with microtubules in vivo. *J Cell Sci*. 118:3195-3201.

Cheeseman, I.M., and A. Desai. 2008. Molecular architecture of the kinetochore-microtubule interface. *Nat Rev Mol Cell Biol*. 9:33-46.

Cheeseman, L.P., E.F. Harry, A.D. McAinsh, I.A. Prior, and S.J. Royle. 2013. Specific removal of TACC3-ch-TOG-clathrin at metaphase deregulates kinetochore fiber tension. *J. Cell Sci*. 126:2102-2113.

Chen, W., and D. Zhang. 2004. Kinetochore fibre dynamics outside the context of the spindle during anaphase. *Nat Cell Biol*. 6:227-231.

Chen, X., M. Liu, H. Lou, Y. Lu, M.T. Zhou, R. Ou, Y. Xu, and K.F. Tang. 2019. Degradation of endogenous proteins and generation of a null-like phenotype in zebrafish using Trim-Away technology. *Genome biology*. 20:19.

Cimini, D. 2008. Merotelic kinetochore orientation, aneuploidy, and cancer. *Biochimica et biophysica acta*. 1786:32-40.

Cimini, D., L.A. Cameron, and E.D. Salmon. 2004. Anaphase spindle mechanics prevent mis-segregation of merotelically oriented chromosomes. *Curr Biol*. 14:2149-2155.

Civelekoglu-Scholey, G., B. He, M. Shen, X. Wan, E. Roscioli, B. Bowden, and D. Cimini. 2013. Dynamic bonds and polar ejection force distribution explain kinetochore oscillations in PtK1 cells. *J Cell Biol*. 201:577-593.

Clift, D., W.A. McEwan, L.I. Labzin, V. Konieczny, B. Mogessie, L.C. James, and M. Schuh. 2017. A Method for the Acute and Rapid Degradation of Endogenous Proteins. *Cell*. 171:1692-1706.e1618.

Clift, D., C. So, W.A. McEwan, L.C. James, and M. Schuh. 2018. Acute and rapid degradation of endogenous proteins by Trim-Away. *Nature protocols*. 13:2149-2175.

Cooper, G.M. 2019. The cell: A molecular approach. Oxford University Press.

Cross, R.A., and A. McAinsh. 2014. Prime movers: the mechanochemistry of mitotic kinesins. *Nat Rev Mol Cell Biol*. 15:257-271.

Cundell, M.J., R.N. Bastos, T. Zhang, J. Holder, U. Gruneberg, B. Novak, and F.A. Barr. 2013. The BEG (PP2A-B55/ENSA/Greatwall) pathway ensures cytokinesis follows chromosome separation. *Molecular cell*. 52:393-405.

de Gramont, A., and O. Cohen-Fix. 2005. The many phases of anaphase. *Trends in biochemical sciences*. 30:559-568.

Deisseroth, K. 2011. Optogenetics. *Nature methods*. 8:26-29.

Desai, A., P.S. Maddox, T.J. Mitchison, and E.D. Salmon. 1998. Anaphase A chromosome movement and poleward spindle microtubule flux occur At similar rates in Xenopus extract spindles. *J Cell Biol*. 141:703-713.

Desai, A., and T.J. Mitchison. 1997. Microtubule polymerization dynamics. *Annu Rev Cell Dev Biol*. 13:83-117.

Ding, R., K.L. McDonald, and J.R. McIntosh. 1993. Three-dimensional reconstruction and analysis of mitotic spindles from the yeast, Schizosaccharomyces pombe. *J Cell Biol*. 120:141-151.

Dogterom, M., and B. Yurke. 1997. Measurement of the force-velocity relation for growing microtubules. *Science*. 278:856-860.

Dougherty, W.G., J.A. Lindbo, H.A. Smith, T.D. Parks, S. Swaney, and W.M. Proebsting. 1994. RNA-mediated virus resistance in transgenic plants: exploitation of a cellular pathway possibly involved in RNA degradation. *Molecular plant-microbe interactions : MPMI*. 7:544-552.

Du, Y., C.A. English, and R. Ohi. 2010. The kinesin-8 Kif18A dampens microtubule plus-end dynamics. *Curr Biol*. 20:374-380.

Dugue, G.P., W. Akemann, and T. Knopfel. 2012. A comprehensive concept of optogenetics. *Progress in brain research*. 196:1-28.

Dumont, S., E.D. Salmon, and T.J. Mitchison. 2012. Deformations within moving kinetochores reveal different sites of active and passive force generation. *Science*. 337:355-358.

Edzuka, T., and G. Goshima. 2019. Drosophila kinesin-8 stabilizes the kinetochore-microtubule interaction. *Journal of Cell Biology*. 218:474-488.

Elbashir, S.M., J. Harborth, W. Lendeckel, A. Yalcin, K. Weber, and T. Tuschl. 2001. Duplexes of 21-nucleotide RNAs mediate RNA interference in cultured mammalian cells. *Nature*. 411:494-498.

Elting, M.W., C.L. Hueschen, D.B. Udy, and S. Dumont. 2014. Force on spindle microtubule minus ends moves chromosomes. *J Cell Biol*. 206:245-256.

Elting, M.W., M. Prakash, D.B. Udy, and S. Dumont. 2017. Mapping Load-Bearing in the Mammalian Spindle Reveals Local Kinetochore Fiber Anchorage that Provides Mechanical Isolation and Redundancy. *Curr. Biol.* 27:2112-2122.

Erent, M., D.R. Drummond, and R.A. Cross. 2012. S. pombe kinesins-8 promote both nucleation and catastrophe of microtubules. *PloS one*. 7:e30738.

Evans, L., T. Mitchison, and M. Kirschner. 1985. Influence of the centrosome on the structure of nucleated microtubules. *J Cell Biol*. 100:1185-1191.

Ferreira, L.T., B. Orr, G. Rajendraprasad, A.J. Pereira, C. Lemos, J.T. Lima, C. Guasch Boldu, J.G. Ferreira, M. Barisic, and H. Maiato. 2020. alpha-Tubulin detyrosination impairs mitotic error correction by suppressing MCAK centromeric activity. *J Cell Biol*. 219.

Fielmich, L.E., R. Schmidt, D.J. Dickinson, B. Goldstein, A. Akhmanova, and S. van den Heuvel. 2018. Optogenetic dissection of mitotic spindle positioning in vivo. *Elife*. 7:e38198.

Fire, A., S. Xu, M.K. Montgomery, S.A. Kostas, S.E. Driver, and C.C. Mello. 1998. Potent and specific genetic interference by double-stranded RNA in Caenorhabditis elegans. *Nature*. 391:806-811.

Fonseca, C.L., H.L.H. Malaby, L.A. Sepaniac, W. Martin, C. Byers, A. Czechanski, D. Messinger, M. Tang, R. Ohi, L.G. Reinholdt, and J. Stumpff. 2019. Mitotic chromosome alignment ensures mitotic fidelity by promoting interchromosomal compaction during anaphase. *J Cell Biol*. 218:1148-1163.

Forer, A. 1965. LOCAL REDUCTION OF SPINDLE FIBER BIREFRINGENCE IN LIVING NEPHROTOMA SUTURALIS (LOEW) SPERMATOCYTES INDUCED BY ULTRAVIOLET MICROBEAM IRRADIATION. *J Cell Biol*. 25:Suppl:95-117.

Forth, S., K.C. Hsia, Y. Shimamoto, and T.M. Kapoor. 2014. Asymmetric friction of nonmotor MAPs can lead to their directional motion in active microtubule networks. *Cell*. 157:420-432.

Funabiki, H., and A.W. Murray. 2000. The Xenopus chromokinesin Xkid is essential for metaphase chromosome alignment and must be degraded to allow anaphase chromosome movement. *Cell*. 102:411-424.

Gadde, S., and R. Heald. 2004. Mechanisms and molecules of the mitotic spindle. *Curr Biol*. 14:R797-805.

Gandhi, R., S. Bonaccorsi, D. Wentworth, S. Doxsey, M. Gatti, and A. Pereira. 2004. The Drosophila kinesin-like protein KLP67A is essential for mitotic and male meiotic spindle assembly. *Mol Biol Cell*. 15:121-131.

Ganem, N.J., and D.A. Compton. 2006. Functional roles of poleward microtubule flux during mitosis. *Cell Cycle*. 5:481-485.

Ganem, N.J., K. Upton, and D.A. Compton. 2005. Efficient mitosis in human cells lacking poleward microtubule flux. *Curr Biol*. 15:1827-1832.

Garcia, M.A., N. Koonrugsa, and T. Toda. 2002. Two kinesin-like Kin I family proteins in fission yeast regulate the establishment of metaphase and the onset of anaphase A. *Curr Biol*. 12:610-621.

Gardner, M.K., D.J. Odde, and K. Bloom. 2008. Kinesin-8 molecular motors: putting the brakes on chromosome oscillations. *Trends Cell Biol*. 18:307-310.

Gardner, M.K., C.G. Pearson, B.L. Sprague, T.R. Zarzar, K. Bloom, E.D. Salmon, and D.J. Odde. 2005. Tension-dependent regulation of microtubule dynamics at kinetochores can explain metaphase congression in yeast. *Mol Biol Cell*. 16:3764-3775.

Gaska, I., M.E. Armstrong, A. Alfieri, and S. Forth. 2020. The Mitotic Crosslinking Protein PRC1 Acts Like a Mechanical Dashpot to Resist Microtubule Sliding. *Dev Cell*. 54:367-378.e365.

Geda, P., S. Patury, J. Ma, N. Bharucha, C.J. Dobry, S.K. Lawson, J.E. Gestwicki, and A. Kumar. 2008. A small molecule-directed approach to control protein localization and function. *Yeast (Chichester, England)*. 25:577-594.

Goodson, H.V., and E.M. Jonasson. 2018. Microtubules and Microtubule-Associated Proteins. *Cold Spring Harbor perspectives in biology*. 10.

Goshima, G., M. Mayer, N. Zhang, N. Stuurman, and R.D. Vale. 2008. Augmin: a protein complex required for centrosome-independent microtubule generation within the spindle. *J Cell Biol*. 181:421-429.

Gregan, J., S. Polakova, L. Zhang, I.M. Tolic-Norrelykke, and D. Cimini. 2011. Merotelic kinetochore attachment: causes and effects. *Trends Cell Biol*. 21:374-381.

Grill, S.W., P. Gonczy, E.H. Stelzer, and A.A. Hyman. 2001. Polarity controls forces governing asymmetric spindle positioning in the Caenorhabditis elegans embryo. *Nature*. 409:630-633.

Grishchuk, E.L., M.I. Molodtsov, F.I. Ataullakhanov, and J.R. McIntosh. 2005. Force production by disassembling microtubules. *Nature*. 438:384-388.

Grissom, P.M., T. Fiedler, E.L. Grishchuk, D. Nicastro, R.R. West, and J.R. McIntosh. 2009. Kinesin-8 from fission yeast: a heterodimeric, plus-end-directed motor that can couple microtubule depolymerization to cargo movement. *Mol Biol Cell*. 20:963-972.

Gruneberg, U., R. Neef, X. Li, E.H. Chan, R.B. Chalamalasetty, E.A. Nigg, and F.A. Barr. 2006. KIF14 and citron kinase act together to promote efficient cytokinesis. *J. Cell Biol.* 172:363-372.

Gruss, O.J., and I. Vernos. 2004. The mechanism of spindle assembly: functions of Ran and its target TPX2. *J Cell Biol*. 166:949-955.

Guntas, G., R.A. Hallett, S.P. Zimmerman, T. Williams, H. Yumerefendi, J.E. Bear, and B. Kuhlman. 2015. Engineering an improved light-induced dimer (iLID) for controlling the localization and activity of signaling proteins. *Proc Natl Acad Sci U S A*. 112:112-117.

Gupta, M.L., Jr., P. Carvalho, D.M. Roof, and D. Pellman. 2006. Plus end-specific depolymerase activity of Kip3, a kinesin-8 protein, explains its role in positioning the yeast mitotic spindle. *Nat Cell Biol*. 8:913-923.

Hannabuss, J., M. Lera-Ramirez, N.I. Cade, F.J. Fourniol, F. Nedelec, and T. Surrey. 2019. Self-Organization of Minimal Anaphase Spindle Midzone Bundles. *Curr Biol*. 29:2120-2130.e2127.

Hannak, E., M. Kirkham, A.A. Hyman, and K. Oegema. 2001. Aurora-A kinase is required for centrosome maturation in Caenorhabditis elegans. *J Cell Biol*. 155:1109-1116.

Hannon, G.J. 2002. RNA interference. *Nature*. 418:244-251.

Haruki, H., J. Nishikawa, and U.K. Laemmli. 2008. The anchor-away technique: rapid, conditional establishment of yeast mutant phenotypes. *Mol. Cell*. 31:925-932.

Holland, A.J., D. Fachinetti, J.S. Han, and D.W. Cleveland. 2012. Inducible, reversible system for the rapid and complete degradation of proteins in mammalian cells. *Proc Natl Acad Sci U S A*. 109:E3350-3357.

Hu, C.K., M. Coughlin, C.M. Field, and T.J. Mitchison. 2011. KIF4 regulates midzone length during cytokinesis. *Curr Biol*. 21:815-824.

Hu, C.K., N. Ozlu, M. Coughlin, J.J. Steen, and T.J. Mitchison. 2012. Plk1 negatively regulates PRC1 to prevent premature midzone formation before cytokinesis. *Mol Biol Cell*. 23:2702-2711.

Hunter, A.W., M. Caplow, D.L. Coy, W.O. Hancock, S. Diez, L. Wordeman, and J. Howard. 2003. The kinesin-related protein MCAK is a microtubule depolymerase that forms an ATP-hydrolyzing complex at microtubule ends. *Molecular cell*. 11:445-457.

Ito, H. 2013. Small RNAs and regulation of transposons in plants. *Genes & genetic systems*. 88:3-7.

Janke, C., and M.M. Magiera. 2020. The tubulin code and its role in controlling microtubule properties and functions. *Nat Rev Mol Cell Biol*. 21:307-326.

Janson, M.E., R. Loughlin, I. Loiodice, C. Fu, D. Brunner, F.J. Nedelec, and P.T. Tran. 2007. Crosslinkers and motors organize dynamic microtubules to form stable bipolar arrays in fission yeast. *Cell*. 128:357-368.

Jaqaman, K., E.M. King, A.C. Amaro, J.R. Winter, J.F. Dorn, H.L. Elliott, N. McHedlishvili, S.E. McClelland, I.M. Porter, M. Posch, A. Toso, G. Danuser, A.D. McAinsh, P. Meraldi, and J.R. Swedlow. 2010. Kinetochore alignment within the metaphase plate is regulated by centromere stiffness and microtubule depolymerases. *J Cell Biol*. 188:665-679.

Jensen, C.G. 1982. Dynamics of spindle microtubule organization: kinetochore fiber microtubules of plant endosperm. *J Cell Biol*. 92:540-558.

Jiang, W., G. Jimenez, N.J. Wells, T.J. Hope, G.M. Wahl, T. Hunter, and R. Fukunaga. 1998. PRC1: a human mitotic spindle-associated CDK substrate protein required for cytokinesis. *Mol. Cell*. 2:877-885.

Joglekar, A.P. 2016. A Cell Biological Perspective on Past, Present and Future Investigations of the Spindle Assembly Checkpoint. *Biology (Basel)*. 5.

Kajtez, J., A. Solomatina, M. Novak, B. Polak, K. Vukusic, J. Rudiger, G. Cojoc, A. Milas, I. Sumanovac Sestak, P. Risteski, F. Tavano, A.H. Klemm, E. Roscioli, J. Welburn, D. Cimini, M. Gluncic, N. Pavin, and I.M. Tolic. 2016. Overlap microtubules link sister k-fibres and balance the forces on bi-oriented kinetochores. *Nat Commun*. 7:10298.

Kalab, P., A. Pralle, E.Y. Isacoff, R. Heald, and K. Weis. 2006. Analysis of a RanGTP-regulated gradient in mitotic somatic cells. *Nature*. 440:697-701.

Kalinina, I., A. Nandi, P. Delivani, M.R. Chacon, A.H. Klemm, D. Ramunno-Johnson, A. Krull, B. Lindner, N. Pavin, and I.M. Tolic-Norrelykke. 2013. Pivoting of microtubules around the spindle pole accelerates kinetochore capture. *Nat Cell Biol*. 15:82-87.

Kanke, M., K. Nishimura, M. Kanemaki, T. Kakimoto, T.S. Takahashi, T. Nakagawa, and H. Masukata. 2011. Auxin-inducible protein depletion system in fission yeast. *BMC cell biology*. 12:8.

Kapitein, L.C., M.E. Janson, S.M. van den Wildenberg, C.C. Hoogenraad, C.F. Schmidt, and E.J. Peterman. 2008. Microtubule-driven multimerization recruits ase1p onto overlapping microtubules. *Curr Biol*. 18:1713-1717.

Kapoor, T.M., and D.A. Compton. 2002. Searching for the middle ground: mechanisms of chromosome alignment during mitosis. *J Cell Biol*. 157:551-556.

Kapoor, T.M., M.A. Lampson, P. Hergert, L. Cameron, D. Cimini, E.D. Salmon, B.F. McEwen, and A. Khodjakov. 2006. Chromosomes can congress to the metaphase plate before biorientation. *Science*. 311:388-391.

Kapoor, T.M., T.U. Mayer, M.L. Coughlin, and T.J. Mitchison. 2000. Probing spindle assembly mechanisms with monastrol, a small molecule inhibitor of the mitotic kinesin, Eg5. *J Cell Biol*. 150:975-988.

Ke, K., J. Cheng, and A.J. Hunt. 2009. The distribution of polar ejection forces determines the amplitude of chromosome directional instability. *Curr Biol*. 19:807-815.

Kellogg, E.H., S. Howes, S.C. Ti, E. Ramirez-Aportela, T.M. Kapoor, P. Chacon, and E. Nogales. 2016. Near-atomic cryo-EM structure of PRC1 bound to the microtubule. *Proc. Natl. Acad. Sci. USA*. 113:9430-9439.

Kennedy, M.J., R.M. Hughes, L.A. Peteya, J.W. Schwartz, M.D. Ehlers, and C.L. Tucker. 2010. Rapid blue-light-mediated induction of protein interactions in living cells. *Nature methods*. 7:973-975.

Khodjakov, A., R.W. Cole, B.R. Oakley, and C.L. Rieder. 2000. Centrosome-independent mitotic spindle formation in vertebrates. *Curr Biol*. 10:59-67.

Khodjakov, A., L. Copenagle, M.B. Gordon, D.A. Compton, and T.M. Kapoor. 2003. Minus-end capture of preformed kinetochore fibers contributes to spindle morphogenesis. *J Cell Biol*. 160:671-683.

Khodjakov, A., and C.L. Rieder. 1996. Kinetochores moving away from their associated pole do not exert a significant pushing force on the chromosome. *J Cell Biol*. 135:315-327.

Kirschner, M., and T. Mitchison. 1986. Beyond self-assembly: from microtubules to morphogenesis. *Cell*. 45:329-342.

Klemm, A.H., A. Bosilj, M. Glunc ic, N. Pavin, and I.M. Tolic. 2018. Metaphase kinetochore movements are regulated by kinesin-8 motors and microtubule dynamic instability. *Mol Biol Cell*. 29:1332-1345.

Kline-Smith, S.L., A. Khodjakov, P. Hergert, and C.E. Walczak. 2004. Depletion of centromeric MCAK leads to chromosome congression and segregation defects due to improper kinetochore attachments. *Mol Biol Cell*. 15:1146-1159.

Krull, A., A. Steinborn, V. Ananthanarayanan, D. Ramunno-Johnson, U. Petersohn, and I.M. Tolic-Norrelykke. 2014. A divide and conquer strategy for the maximum likelihood localization of low intensity objects. *Opt Express*. 22:210-228.

Kurasawa, Y., W.C. Earnshaw, Y. Mochizuki, N. Dohmae, and K. Todokoro. 2004. Essential roles of KIF4 and its binding partner PRC1 in organized central spindle midzone formation. *EMBO J*. 23:3237-3248.

Kuriyama, R., and G.G. Borisy. 1981. Microtubule-nucleating activity of centrosomes in Chinese hamster ovary cells is independent of the centriole cycle but coupled to the mitotic cycle. *J Cell Biol*. 91:822-826.

LaFountain, J.R., Jr., C.S. Cohan, A.J. Siegel, and D.J. LaFountain. 2004. Direct visualization of microtubule flux during metaphase and anaphase in crane-fly spermatocytes. *Mol Biol Cell*. 15:5724-5732.

Lan, W., X. Zhang, S.L. Kline-Smith, S.E. Rosasco, G.A. Barrett-Wilt, J. Shabanowitz, D.F. Hunt, C.E. Walczak, and P.T. Stukenberg. 2004. Aurora B phosphorylates centromeric MCAK and regulates its localization and microtubule depolymerization activity. *Curr Biol*. 14:273-286.

Lane, N. 2015. The unseen world: reflections on Leeuwenhoek (1677) 'Concerning little animals'. *Philos Trans R Soc Lond B Biol Sci*. 370.

Lansky, Z., M. Braun, A. Ludecke, M. Schlierf, P.R. ten Wolde, M.E. Janson, and S. Diez. 2015. Diffusible crosslinkers generate directed forces in microtubule networks. *Cell*. 160:1159-1168.

Lee, K., and K. Rhee. 2011. PLK1 phosphorylation of pericentrin initiates centrosome maturation at the onset of mitosis. *J Cell Biol*. 195:1093-1101.

Levesque, A.A., and D.A. Compton. 2001. The chromokinesin Kid is necessary for chromosome arm orientation and oscillation, but not congression, on mitotic spindles. *J Cell Biol*. 154:1135-1146.

Levskaya, A., O.D. Weiner, W.A. Lim, and C.A. Voigt. 2009. Spatiotemporal control of cell signalling using a light-switchable protein interaction. *Nature*. 461:997-1001.

Li, S., X. Prasanna, V.T. Salo, I. Vattulainen, and E. Ikonen. 2019. An efficient auxin-inducible degron system with low basal degradation in human cells. *Nature methods*. 16:866-869.

Liu, J., Z. Wang, K. Jiang, L. Zhang, L. Zhao, S. Hua, F. Yan, Y. Yang, D. Wang, C. Fu, X. Ding, Z. Guo, and X. Yao. 2009. PRC1 cooperates with CLASP1 to organize central spindle plasticity in mitosis. *J. Biol. Chem*. 284:23059-23071.

Liu, X., L. Xu, J. Li, P.Y. Yao, W. Wang, H. Ismail, H. Wang, B. Liao, Z. Yang, T. Ward, K. Ruan, J. Zhang, Q. Wu, P. He, X. Ding, D. Wang, C. Fu, Z. Dou, W. Wang, X. Liu, and X. Yao. 2019. Mitotic motor CENP-E cooperates with PRC1 in temporal control of central spindle assembly. *J Mol Cell Biol*.

Loiodice, I., J. Staub, T.G. Setty, N.P. Nguyen, A. Paoletti, and P.T. Tran. 2005. Ase1p organizes antiparallel microtubule arrays during interphase and mitosis in fission yeast. *Mol Biol Cell*. 16:1756-1768.

Lukinavicius, G., C. Blaukopf, E. Pershagen, A. Schena, L. Reymond, E. Derivery, M. Gonzalez-Gaitan, E. D'Este, S.W. Hell, D. Wolfram Gerlich, and K. Johnsson. 2015. SiR-Hoechst is a far-red DNA stain for live-cell nanoscopy. *Nat. Commun*. 6:8497.

Lukinavicius, G., L. Reymond, E. D'Este, A. Masharina, F. Gottfert, H. Ta, A. Guther, M. Fournier, S. Rizzo, H. Waldmann, C. Blaukopf, C. Sommer, D.W. Gerlich, H.D. Arndt, S.W. Hell, and K. Johnsson. 2014. Fluorogenic probes for live-cell imaging of the cytoskeleton. *Nat. Methods*. 11:731-733.

Maddox, P., A. Straight, P. Coughlin, T.J. Mitchison, and E.D. Salmon. 2003. Direct observation of microtubule dynamics at kinetochores in Xenopus extract spindles: implications for spindle mechanics. *J Cell Biol*. 162:377-382.

Maffini, S., A.R. Maia, A.L. Manning, Z. Maliga, A.L. Pereira, M. Junqueira, A. Shevchenko, A. Hyman, J.R. Yates, 3rd, N. Galjart, D.A. Compton, and H. Maiato. 2009. Motor-independent targeting of CLASPs to kinetochores by CENP-E promotes microtubule turnover and poleward flux. *Curr Biol*. 19:1566-1572.

Magidson, V., C.B. O'Connell, J. Loncarek, R. Paul, A. Mogilner, and A. Khodjakov. 2011. The spatial arrangement of chromosomes during prometaphase facilitates spindle assembly. *Cell*. 146:555-567.

Maiato, H., E.A. Fairley, C.L. Rieder, J.R. Swedlow, C.E. Sunkel, and W.C. Earnshaw. 2003. Human CLASP1 is an outer kinetochore component that regulates spindle microtubule dynamics. *Cell*. 113:891-904.

Maiato, H., A.M. Gomes, F. Sousa, and M. Barisic. 2017. Mechanisms of Chromosome Congression during Mitosis. *Biology (Basel)*. 6.

Maiato, H., A. Khodjakov, and C.L. Rieder. 2005. Drosophila CLASP is required for the incorporation of microtubule subunits into fluxing kinetochore fibres. *Nat Cell Biol*. 7:42-47.

Maiato, H., and M. Lince-Faria. 2010. The perpetual movements of anaphase. *Cell Mol Life Sci*. 67:2251-2269.

Maiato, H., C.L. Rieder, and A. Khodjakov. 2004a. Kinetochore-driven formation of kinetochore fibers contributes to spindle assembly during animal mitosis. *J Cell Biol*. 167:831-840.

Maiato, H., P. Sampaio, and C.E. Sunkel. 2004b. Microtubule-associated proteins and their essential roles during mitosis. *International review of cytology*. 241:53-153.

Mann, B.J., and P. Wadsworth. 2018. Distribution of Eg5 and TPX2 in mitosis: Insight from CRISPR tagged cells. *Cytoskeleton (Hoboken)*. 75:508-521.

Mary, H., J. Fouchard, G. Gay, C. Reyes, T. Gauthier, C. Gruget, J. Pecreaux, S. Tournier, and Y. Gachet. 2015. Fission yeast kinesin-8 controls chromosome congression independently of oscillations. *J Cell Sci*. 128:3720-3730.

Mastronarde, D.N., K.L. McDonald, R. Ding, and J.R. McIntosh. 1993. Interpolar spindle microtubules in PTK cells. *J Cell Biol*. 123:1475-1489.

Matos, I., A.J. Pereira, M. Lince-Faria, L.A. Cameron, E.D. Salmon, and H. Maiato. 2009. Synchronizing chromosome segregation by flux-dependent force equalization at kinetochores. *J Cell Biol*. 186:11-26.

Maurer, S.P., F.J. Fourniol, G. Bohner, C.A. Moores, and T. Surrey. 2012. EBs recognize a nucleotide-dependent structural cap at growing microtubule ends. *Cell*. 149:371-382.

Mayer, T.U., T.M. Kapoor, S.J. Haggarty, R.W. King, S.L. Schreiber, and T.J. Mitchison. 1999. Small molecule inhibitor of mitotic spindle bipolarity identified in a phenotype-based screen. *Science*. 286:971-974.

Mayr, M.I., S. Hummer, J. Bormann, T. Gruner, S. Adio, G. Woehlke, and T.U. Mayer. 2007. The human kinesin Kif18A is a motile microtubule depolymerase essential for chromosome congression. *Curr. Biol*. 17:488-498.

Mazumdar, M., S. Sundareshan, and T. Misteli. 2004. Human chromokinesin KIF4A functions in chromosome condensation and segregation. *J Cell Biol*. 166:613-620.

Mazzarello, P. 1999. A unifying concept: the history of cell theory. *Nat Cell Biol*. 1:E13-15.

McDonald, K.L., E.T. O'Toole, D.N. Mastronarde, and J.R. McIntosh. 1992. Kinetochore microtubules in PTK cells. *J Cell Biol*. 118:369-383.

McEwen, B.F., G.K. Chan, B. Zubrowski, M.S. Savoian, M.T. Sauer, and T.J. Yen. 2001. CENP-E is essential for reliable bioriented spindle attachment, but chromosome alignment can be achieved via redundant mechanisms in mammalian cells. *Mol Biol Cell*. 12:2776-2789.

McIntosh, J.R., E.L. Grishchuk, and R.R. West. 2002. Chromosome-microtubule interactions during mitosis. *Annu Rev Cell Dev Biol*. 18:193-219.

McIntosh, J.R., and S.C. Landis. 1971. The distribution of spindle microtubules during mitosis in cultured human cells. *J Cell Biol*. 49:468-497.

McKinley, K.L., and I.M. Cheeseman. 2017. Large-Scale Analysis of CRISPR/Cas9 Cell-Cycle Knockouts Reveals the Diversity of p53-Dependent Responses to Cell-Cycle Defects. *Dev Cell*. 40:405-420.e402.

McKinley, K.L., N. Sekulic, L.Y. Guo, T. Tsinman, B.E. Black, and I.M. Cheeseman. 2015. The CENP-L-N Complex Forms a Critical Node in an Integrated Meshwork of Interactions at the Centromere-Kinetochore Interface. *Molecular cell*. 60:886-898.

Meraldi, P., and E.A. Nigg. 2002. The centrosome cycle. *FEBS Lett*. 521:9-13.

Milas, A., M. Jagric, J. Martincic, and I.M. Tolic. 2018. Optogenetic reversible knocksideways, laser ablation, and photoactivation on the mitotic spindle in human cells. *Methods Cell Biol*. 145:191-215.

Milas, A., and I.M. Tolić. 2016. Relaxation of interkinetochore tension after severing of a k-fiber depends on the length of the k-fiber stub. *Matters (Zür)*.

Mimori-Kiyosue, Y., I. Grigoriev, H. Sasaki, C. Matsui, A. Akhmanova, S. Tsukita, and I. Vorobjev. 2006. Mammalian CLASPs are required for mitotic spindle organization and kinetochore alignment. *Genes to cells : devoted to molecular & cellular mechanisms*. 11:845-857.

Mitchison, T., and M. Kirschner. 1984. Dynamic instability of microtubule growth. *Nature*. 312:237-242.

Mitchison, T.J. 1989. Polewards microtubule flux in the mitotic spindle: evidence from photoactivation of fluorescence. *J Cell Biol*. 109:637-652.

Mitchison, T.J., and M.W. Kirschner. 1985. Properties of the kinetochore in vitro. II. Microtubule capture and ATP-dependent translocation. *J Cell Biol*. 101:766-777.

Miyamoto, D.T., Z.E. Perlman, K.S. Burbank, A.C. Groen, and T.J. Mitchison. 2004. The kinesin Eg5 drives poleward microtubule flux in Xenopus laevis egg extract spindles. *J Cell Biol*. 167:813-818.

Mollinari, C., J.P. Kleman, W. Jiang, G. Schoehn, T. Hunter, and R.L. Margolis. 2002. PRC1 is a microtubule binding and bundling protein essential to maintain the mitotic spindle midzone. *J. Cell Biol*. 157:1175-1186.

Mollinari, C., J.P. Kleman, Y. Saoudi, S.A. Jablonski, J. Perard, T.J. Yen, and R.L. Margolis. 2005. Ablation of PRC1 by small interfering RNA demonstrates that cytokinetic abscission requires a central spindle bundle in mammalian cells, whereas completion of furrowing does not. *Mol. Biol. Cell*. 16:1043-1055.

Musacchio, A., and A. Desai. 2017. A Molecular View of Kinetochore Assembly and Function. *Biology (Basel)*. 6.

Musacchio, A., and E.D. Salmon. 2007. The spindle-assembly checkpoint in space and time. *Nat Rev Mol Cell Biol*. 8:379-393.

Nabeshima, K., T. Nakagawa, A.F. Straight, A. Murray, Y. Chikashige, Y.M. Yamashita, Y. Hiraoka, and M. Yanagida. 1998. Dynamics of centromeres during metaphase-anaphase transition in fission yeast: Dis1 is implicated in force balance in metaphase bipolar spindle. *Mol Biol Cell*. 9:3211-3225.

Nagel, G., T. Szellas, W. Huhn, S. Kateriya, N. Adeishvili, P. Berthold, D. Ollig, P. Hegemann, and E. Bamberg. 2003. Channelrhodopsin-2, a directly light-gated cation-selective membrane channel. *Proc Natl Acad Sci U S A*. 100:13940-13945.

Napoli, C., C. Lemieux, and R. Jorgensen. 1990. Introduction of a Chimeric Chalcone Synthase Gene into Petunia Results in Reversible Co-Suppression of Homologous Genes in trans. *The Plant cell*. 2:279-289.

Neef, R., U. Gruneberg, R. Kopajtich, X. Li, E.A. Nigg, H. Sillje, and F.A. Barr. 2007. Choice of Plk1 docking partners during mitosis and cytokinesis is controlled by the activation state of Cdk1. *Nat Cell Biol*. 9:436-444.

Nicklas, R.B., and D.F. Kubai. 1985. Microtubules, chromosome movement, and reorientation after chromosomes are detached from the spindle by micromanipulation. *Chromosoma*. 92:313-324.

Nishimura, K., T. Fukagawa, H. Takisawa, T. Kakimoto, and M. Kanemaki. 2009. An auxin-based degron system for the rapid depletion of proteins in nonplant cells. *Nature methods*. 6:917-922.

Nixon, F.M., C. Gutierrez-Caballero, F.E. Hood, D.G. Booth, I.A. Prior, and S.J. Royle. 2015. The mesh is a network of microtubule connectors that stabilizes individual kinetochore fibers of the mitotic spindle. *Elife*. 4:e07635.

Nixon, F.M., T.R. Honnor, N.I. Clarke, G.P. Starling, A.J. Beckett, A.M. Johansen, J.A. Brettschneider, I.A. Prior, and S.J. Royle. 2017. Microtubule organization within mitotic spindles revealed by serial block face scanning electron microscopy and image analysis. *J Cell Sci*. 130:1845-1855.

Nogales, E., M. Whittaker, R.A. Milligan, and K.H. Downing. 1999. High-resolution model of the microtubule. *Cell*. 96:79-88.

O'Connell, C.B., and A.L. Khodjakov. 2007. Cooperative mechanisms of mitotic spindle formation. *J Cell Sci*. 120:1717-1722.

O'Neill, P.R., V. Kalyanaraman, and N. Gautam. 2016. Subcellular optogenetic activation of Cdc42 controls local and distal signaling to drive immune cell migration. *Mol. Biol. Cell*. 27:1442-1450.

O'Toole, E., M. Morphew, and J.R. McIntosh. 2020. Electron tomography reveals aspects of spindle structure important for mechanical stability at metaphase. *Mol Biol Cell*. 31:184-195.

Ohi, R., M.L. Coughlin, W.S. Lane, and T.J. Mitchison. 2003. An inner centromere protein that stimulates the microtubule depolymerizing activity of a KinI kinesin. *Dev Cell*. 5:309-321.

Okumura, M., T. Natsume, M.T. Kanemaki, and T. Kiyomitsu. 2018. Dynein-Dynactin-NuMA clusters generate cortical spindle-pulling forces as a multi-arm ensemble. *Elife*. 7:e36559.

Pavin, N., and I.M. Tolic. 2016. Self-Organization and Forces in the Mitotic Spindle. *Annu Rev Biophys*. 45:279-298.

Paweletz, N. 2001. Walther Flemming: pioneer of mitosis research. *Nat Rev Mol Cell Biol*. 2:72-75.

Pecot, M.Y., and V. Malhotra. 2004. Golgi membranes remain segregated from the endoplasmic reticulum during mitosis in mammalian cells. *Cell*. 116:99-107.

Pereira, A.L., A.J. Pereira, A.R. Maia, K. Drabek, C.L. Sayas, P.J. Hergert, M. Lince-Faria, I. Matos, C. Duque, T. Stepanova, C.L. Rieder, W.C. Earnshaw, N. Galjart, and H. Maiato. 2006. Mammalian CLASP1 and CLASP2 cooperate to ensure mitotic fidelity by regulating spindle and kinetochore function. *Mol Biol Cell*. 17:4526-4542.

Polak, B., P. Risteski, S. Lesjak, and I.M. Tolic. 2017. PRC1-labeled microtubule bundles and kinetochore pairs show one-to-one association in metaphase. *EMBO Rep*. 18:217-230.

Prosser, S.L., and L. Pelletier. 2017. Mitotic spindle assembly in animal cells: a fine balancing act. *Nat Rev Mol Cell Biol*. 18:187-201.

Renicke, C., D. Schuster, S. Usherenko, L.O. Essen, and C. Taxis. 2013. A LOV2 domain-based optogenetic tool to control protein degradation and cellular function. *Chemistry & biology*. 20:619-626.

Rieder, C.L. 1981. The structure of the cold-stable kinetochore fiber in metaphase PtK1 cells. *Chromosoma*. 84:145-158.

Rieder, C.L., E.A. Davison, L.C. Jensen, L. Cassimeris, and E.D. Salmon. 1986. Oscillatory movements of monooriented chromosomes and their position relative to the spindle pole result from the ejection properties of the aster and half-spindle. *J Cell Biol*. 103:581-591.

Rieder, C.L., and E.D. Salmon. 1994. Motile kinetochores and polar ejection forces dictate chromosome position on the vertebrate mitotic spindle. *J Cell Biol*. 124:223-233.

Rieder, C.L., and E.D. Salmon. 1998. The vertebrate cell kinetochore and its roles during mitosis. *Trends Cell Biol*. 8:310-318.

Robinson, M.S., and J. Hirst. 2013. Rapid inactivation of proteins by knocksideways. *Current protocols in cell biology*. 61:15.20.11-17.

Robinson, M.S., D.A. Sahlender, and S.D. Foster. 2010. Rapid inactivation of proteins by rapamycin-induced rerouting to mitochondria. *Dev. Cell*. 18:324-331.

Rogers, G.C., S.L. Rogers, T.A. Schwimmer, S.C. Ems-McClung, C.E. Walczak, R.D. Vale, J.M. Scholey, and D.J. Sharp. 2004. Two mitotic kinesins cooperate to drive sister chromatid separation during anaphase. *Nature*. 427:364-370.

Romano, N., and G. Macino. 1992. Quelling: transient inactivation of gene expression in Neurospora crassa by transformation with homologous sequences. *Molecular microbiology*. 6:3343-3353.

Roostalu, J., E. Schiebel, and A. Khmelinskii. 2010. Cell cycle control of spindle elongation. *Cell Cycle*. 9:1084-1090.

Ruiz, M.T., O. Voinnet, and D.C. Baulcombe. 1998. Initiation and maintenance of virus-induced gene silencing. *The Plant cell*. 10:937-946.

Saxton, W.M., D.L. Stemple, R.J. Leslie, E.D. Salmon, M. Zavortink, and J.R. McIntosh. 1984. Tubulin dynamics in cultured mammalian cells. *J Cell Biol*. 99:2175-2186.

Schuyler, S.C., J.Y. Liu, and D. Pellman. 2003. The molecular function of Ase1p: evidence for a MAP-dependent midzone- specific spindle matrix. Microtubule-associated proteins. *J Cell Biol*. 160:517-528.

Schuyler, S.C., and D. Pellman. 2001. Microtubule "plus-end-tracking proteins": The end is just the beginning. *Cell*. 105:421-424.

Shalem, O., N.E. Sanjana, E. Hartenian, X. Shi, D.A. Scott, T. Mikkelson, D. Heckl, B.L. Ebert, D.E. Root, J.G. Doench, and F. Zhang. 2014. Genome-scale CRISPR-Cas9 knockout screening in human cells. *Science*. 343:84-87.

Silkworth, W.T., and D. Cimini. 2012. Transient defects of mitotic spindle geometry and chromosome segregation errors. *Cell division*. 7:19.

Skibbens, R.V., V.P. Skeen, and E.D. Salmon. 1993. Directional instability of kinetochore motility during chromosome congression and segregation in mitotic newt lung cells: a push-pull mechanism. *J Cell Biol*. 122:859-875.

Smertenko, A.P., D. Kaloriti, H.Y. Chang, J. Fiserova, Z. Opatrny, and P.J. Hussey. 2008. The C-terminal variable region specifies the dynamic properties of Arabidopsis microtubule-associated protein MAP65 isotypes. *The Plant cell*. 20:3346-3358.

Snyder, J.A., L. Armstrong, O.G. Stonington, T.P. Spurck, and J.D. Pickett-Heaps. 1991. UV-microbeam irradiations of the mitotic spindle: spindle forces and structural analysis of lesions. *European journal of cell biology*. 55:122-132.

Sprague, B.L., C.G. Pearson, P.S. Maddox, K.S. Bloom, E.D. Salmon, and D.J. Odde. 2003. Mechanisms of microtubule-based kinetochore positioning in the yeast metaphase spindle. *Biophysical journal*. 84:3529-3546.

Steblyanko, Y., G. Rajendraprasad, M. Osswald, S. Eibes, A. Jacome, S. Geley, A.J. Pereira, H. Maiato, and M. Barisic. 2020. Microtubule poleward flux in human cells is driven by the coordinated action of four kinesins. *Embo j*:e105432.

Stepanova, T., J. Slemmer, C.C. Hoogenraad, G. Lansbergen, B. Dortland, C.I. De Zeeuw, F. Grosveld, G. van Cappellen, A. Akhmanova, and N. Galjart. 2003. Visualization of microtubule growth in cultured neurons via the use of EB3-GFP (end-binding protein 3-green fluorescent protein). *J Neurosci*. 23:2655-2664.

Strickland, D., Y. Lin, E. Wagner, C.M. Hope, J. Zayner, C. Antoniou, T.R. Sosnick, E.L. Weiss, and M. Glotzer. 2012. TULIPs: tunable, light-controlled interacting protein tags for cell biology. *Nature methods*. 9:379-384.

Strickland, D., K. Moffat, and T.R. Sosnick. 2008. Light-activated DNA binding in a designed allosteric protein. *Proc Natl Acad Sci U S A*. 105:10709-10714.

Strunov, A., L.V. Boldyreva, E.N. Andreyeva, G.A. Pavlova, J.V. Popova, A.V. Razuvaeva, A.F. Anders, F. Renda, A.V. Pindyurin, M. Gatti, and E. Kiseleva. 2018. Ultrastructural analysis of mitotic Drosophila S2 cells identifies distinctive microtubule and intracellular membrane behaviors. *BMC Biol*. 16:68.

Stumpff, J., G. von Dassow, M. Wagenbach, C. Asbury, and L. Wordeman. 2008. The kinesin-8 motor Kif18A suppresses kinetochore movements to control mitotic chromosome alignment. *Dev. Cell*. 14:252-262.

Stumpff, J., M. Wagenbach, A. Franck, C.L. Asbury, and L. Wordeman. 2012. Kif18A and chromokinesins confine centromere movements via microtubule growth suppression and spatial control of kinetochore tension. *Dev. Cell*. 22:1017-1029.

Su, X., H. Arellano-Santoyo, D. Portran, J. Gaillard, M. Vantard, M. Thery, and D. Pellman. 2013. Microtubule-sliding activity of a kinesin-8 promotes spindle assembly and spindle-length control. *Nat Cell Biol*. 15:948-957.

Subramanian, R., S.C. Ti, L. Tan, S.A. Darst, and T.M. Kapoor. 2013. Marking and measuring single microtubules by PRC1 and kinesin-4. *Cell*. 154:377-390.

Subramanian, R., E.M. Wilson-Kubalek, C.P. Arthur, M.J. Bick, E.A. Campbell, S.A. Darst, R.A. Milligan, and T.M. Kapoor. 2010. Insights into antiparallel microtubule crosslinking by PRC1, a conserved nonmotor microtubule binding protein. *Cell*. 142:433-443.

Sudakin, V., G.K. Chan, and T.J. Yen. 2001. Checkpoint inhibition of the APC/C in HeLa cells is mediated by a complex of BUBR1, BUB3, CDC20, and MAD2. *J Cell Biol*. 154:925-936.

Suresh, P., A.F. Long, and S. Dumont. 2020. Microneedle manipulation of the mammalian spindle reveals specialized, short-lived reinforcement near chromosomes. *Elife*. 9.

Tanenbaum, M.E., and R.H. Medema. 2010. Mechanisms of centrosome separation and bipolar spindle assembly. *Dev Cell*. 19:797-806.

Tischer, C., D. Brunner, and M. Dogterom. 2009. Force- and kinesin-8-dependent effects in the spatial regulation of fission yeast microtubule dynamics. *Mol Syst Biol*. 5:250.

Tolic, I.M. 2018. Mitotic spindle: kinetochore fibers hold on tight to interpolar bundles. *Eur Biophys J*. 47:191-203.

Tucker, C.L., J.D. Vrana, and M.J. Kennedy. 2014. Tools for controlling protein interactions using light. *Current protocols in cell biology*. 64:17.16.11-20.

van der Krol, A.R., L.A. Mur, M. Beld, J.N. Mol, and A.R. Stuitje. 1990. Flavonoid genes in petunia: addition of a limited number of gene copies may lead to a suppression of gene expression. *The Plant cell*. 2:291-299.

van Haren, J., R.A. Charafeddine, A. Ettinger, H. Wang, K.M. Hahn, and T. Wittmann. 2018. Local control of intracellular microtubule dynamics by EB1 photodissociation. *Nat. Cell Biol.* 20:252-261.

Varga, V., J. Helenius, K. Tanaka, A.A. Hyman, T.U. Tanaka, and J. Howard. 2006. Yeast kinesin-8 depolymerizes microtubules in a length-dependent manner. *Nat Cell Biol*. 8:957-962.

Varga, V., C. Leduc, V. Bormuth, S. Diez, and J. Howard. 2009. Kinesin-8 motors act cooperatively to mediate length-dependent microtubule depolymerization. *Cell*. 138:1174-1183.

Vladimirou, E., N. McHedlishvili, I. Gasic, J.W. Armond, C.P. Samora, P. Meraldi, and A.D. McAinsh. 2013. Nonautonomous movement of chromosomes in mitosis. *Dev Cell*. 27:60-71.

Voets, E., J. Marsman, J. Demmers, R. Beijersbergen, and R. Wolthuis. 2015. The lethal response to Cdk1 inhibition depends on sister chromatid alignment errors generated by KIF4 and isoform 1 of PRC1. *Scientific reports*. 5:14798.

Vukusic, K., R. Buda, A. Bosilj, A. Milas, N. Pavin, and I.M. Tolic. 2017. Microtubule Sliding within the Bridging Fiber Pushes Kinetochore Fibers Apart to Segregate Chromosomes. *Dev Cell*. 43:11-23 e16.

Vukusic, K., R. Buda, I. Ponjavic, P. Risteski, and I.M. Tolic. 2019a. Chromosome segregation is driven by joint microtubule sliding action of kinesins KIF4A and EG5. *bioRxiv*.

Vukusic, K., R. Buda, and I.M. Tolic. 2019b. Force-generating mechanisms of anaphase in human cells. *J Cell Sci*. 132.

Walczak, C.E., S. Cai, and A. Khodjakov. 2010. Mechanisms of chromosome behaviour during mitosis. *Nat Rev Mol Cell Biol*. 11:91-102.

Wandke, C., M. Barisic, R. Sigl, V. Rauch, F. Wolf, A.C. Amaro, C.H. Tan, A.J. Pereira, U. Kutay, H. Maiato, P. Meraldi, and S. Geley. 2012. Human chromokinesins promote chromosome congression and spindle microtubule dynamics during mitosis. *J. Cell Biol.* 198:847-863.

Wang, H., and K.M. Hahn. 2016. LOVTRAP: A Versatile Method to Control Protein Function with Light. *Curr. Protoc. Cell Biol.* 73:21 10 21-21 10 14.

Wang, T., J.J. Wei, D.M. Sabatini, and E.S. Lander. 2014. Genetic screens in human cells using the CRISPR-Cas9 system. *Science*. 343:80-84.

Wargacki, M.M., J.C. Tay, E.G. Muller, C.L. Asbury, and T.N. Davis. 2010. Kip3, the yeast kinesin-8, is required for clustering of kinetochores at metaphase. *Cell Cycle*. 9:2581-2588.

Wendell, K.L., L. Wilson, and M.A. Jordan. 1993. Mitotic block in HeLa cells by vinblastine: ultrastructural changes in kinetochore-microtubule attachment and in centrosomes. *J Cell Sci*. 104 (Pt 2):261-274.

West, R.R., T. Malmstrom, and J.R. McIntosh. 2002. Kinesins klp5(+) and klp6(+) are required for normal chromosome movement in mitosis. *J Cell Sci*. 115:931-940.

Wijeratne, S., and R. Subramanian. 2018. Geometry of antiparallel microtubule bundles regulates relative sliding and stalling by PRC1 and Kif4A. *Elife*. 7.

Winey, M., C.L. Mamay, E.T. O'Toole, D.N. Mastronarde, T.H. Giddings, Jr., K.L. McDonald, and J.R. McIntosh. 1995. Three-dimensional ultrastructural analysis of the Saccharomyces cerevisiae mitotic spindle. *J Cell Biol.* 129:1601-1615.

Winters, L., I. Ban, M. Prelogovic, I. Kalinina, N. Pavin, and I.M. Tolic. 2019. Pivoting of microtubules driven by minus-end-directed motors leads to spindle assembly. *BMC Biol*. 17:42.

Wise, D., L. Cassimeris, C.L. Rieder, P. Wadsworth, and E.D. Salmon. 1991. Chromosome fiber dynamics and congression oscillations in metaphase PtK2 cells at 23 degrees C. *Cell Motil Cytoskeleton*. 18:131-142.

Wollman, R., E.N. Cytrynbaum, J.T. Jones, T. Meyer, J.M. Scholey, and A. Mogilner. 2005. Efficient chromosome capture requires a bias in the 'search-and-capture' process during mitotic-spindle assembly. *Curr Biol*. 15:828-832.

Wordeman, L., J. Decarreau, J.J. Vicente, and M. Wagenbach. 2016. Divergent microtubule assembly rates after short- versus long-term loss of end-modulating kinesins. *Mol. Biol. Cell*. 27:1300-1309.

Wordeman, L., and T.J. Mitchison. 1995. Identification and partial characterization of mitotic centromere- associated kinesin, a kinesin-related protein that associates with centromeres during mitosis. *J Cell Biol*. 128:95-104.

Wordeman, L., M. Wagenbach, and G. von Dassow. 2007. MCAK facilitates chromosome movement by promoting kinetochore microtubule turnover. *J Cell Biol*. 179:869-879.

Yang, X., A.P. Jost, O.D. Weiner, and C. Tang. 2013. A light-inducible organelle-targeting system for dynamically activating and inactivating signaling in budding yeast. *Mol. Biol. Cell*. 24:2419-2430.

Yu, C.H., S. Redemann, H.Y. Wu, R. Kiewisz, T.Y. Yoo, W. Conway, R. Farhadifar, T. Muller-Reichert, and D. Needleman. 2019. Central-spindle microtubules are strongly coupled to chromosomes during both anaphase A and anaphase B. *Mol Biol Cell*. 30:2503-2514.

Yu, N., L. Signorile, S. Basu, S. Ottema, J.H.G. Lebbink, K. Leslie, I. Smal, D. Dekkers, J. Demmers, and N. Galjart. 2016. Isolation of Functional Tubulin Dimers and of Tubulin-Associated Proteins from Mammalian Cells. *Curr. Biol*. 26:1728-1736.

Zhang, H., C. Aonbangkhen, E.V. Tarasovetc, E.R. Ballister, D.M. Chenoweth, and M.A. Lampson. 2017. Optogenetic control of kinetochore function. *Nat. Chem. Biol*. 13:1096-1101.

Zhang, L., J.D. Ward, Z. Cheng, and A.F. Dernburg. 2015. The auxin-inducible degradation (AID) system enables versatile conditional protein depletion in C. elegans. *Development (Cambridge, England)*. 142:4374-4384.

Zhou, X.X., H.K. Chung, A.J. Lam, and M.Z. Lin. 2012. Optical control of protein activity by fluorescent protein domains. *Science*. 338:810-814.

Zhu, C., and W. Jiang. 2005. Cell cycle-dependent translocation of PRC1 on the spindle by Kif4 is essential for midzone formation and cytokinesis. *Proc. Natl. Acad. Sci. USA*. 102:343-348.

Zhu, C., E. Lau, R. Schwarzenbacher, E. Bossy-Wetzel, and W. Jiang. 2006. Spatiotemporal control of spindle midzone formation by PRC1 in human cells. *Proc. Natl. Acad. Sci. USA*. 103:6196-6201.

Zoncu, R., R.M. Perera, D.M. Balkin, M. Pirruccello, D. Toomre, and P. De Camilli. 2009. A phosphoinositide switch controls the maturation and signaling properties of APPL endosomes. *Cell*. 136:1110-1121.

Zoncu, R., R.M. Perera, R. Sebastian, F. Nakatsu, H. Chen, T. Balla, G. Ayala, D. Toomre, and P.V. De Camilli. 2007. Loss of endocytic clathrin-coated pits upon acute depletion of phosphatidylinositol 4,5-bisphosphate. *Proc Natl Acad Sci U S A*. 104:3793-3798.

8. BIOGRAPHY

Mihaela Jagrić was born on August 10, 1991 in Brčko, Bosnia and Herzegovina. She graduated Molecular Biology in 2016 from the Faculty of Science, University of Zagreb. During that time she participated in the manifestation "Noć Biologije" for which she was awarded with the Special Rector's Award in 2013. During her Master studies she was among top 10% best students and was awarded with the stipend for excellence by University of Zagreb. Since 2016 she has been working as a PhD student in the Laboratory for Cell Biophysics at the Ruđer Bošković Institute, Zagreb under the mentorship of prof. Iva Tolić on the project funded by Croatian Science Foundation (HRZZ) – Oscillatory Dynamics of Cytoskeleton (IP-2014-09-4753). At the same time she has enrolled in the postgraduate study of Biology at Faculty of Science, University of Zagreb. She participated in 3 international conferences where she gave an oral presentation of the scientific results in two of them (*Mitotic spindle: from living and synthetic systems to theory*, Split, 2019 and *EMBL Symposium: Microtubules: From Atoms to Complex Systems*, Heidelberg, 2020) and poster presentation in one (*EMBL Symposium: Microtubules: From Atoms to Complex Systems*, Heidelberg, 2018). She also attended the workshop European Science Camp at Instituto Gulbenkian de Ciência, during the period 24th of June to 5th of July 2019.

Publications:

Milas, Ana*; **Jagrić, Mihaela***; Martinčić, Jelena*; Tolić, Iva M. (2018) Optogenetic reversible knocksideways, laser ablation, and photoactivation on the mitotic spindle in human cells. *Methods in Cell Biology*

Jagrić, Mihaela*; Risteski, Patrik*; Martinčić, Jelena*; Milas, Ana; Tolić, Iva M. (2021) Optogenetic control of PRC1 reveals its role in chromosome alignment on the spindle by overlap length-dependent forces. *eLife.* 10: e61170

Risteski, Patrik*; **Jagrić Mihaela***; Tolić Iva M. (2021) Sliding of kinetochore fibers along bridging fibers helps center the chromosomes on the spindle. *bioRxiv.* https://doi.org/10.1101/2020.12.30.424837 (preprint)

* These authors contributed equally.

"All we have to decide is what to do with the time that is given us" – Gandalf,

J.R.R Tolkien, *Lord of the Rings: Fellowship of the Ring*